POLITECNICO DI MILANO

Faculty of Engineering

Department of Chemistry, Materials

and Chemical Engineering “Giulio Natta"

Master of Materials Engineering Thesis

Electrochemical Deposition of Composite NiCo Alloys

Supervisor

Dr. Luca Magagnin

by

Sougata Pahari

737143

Master of Materials Engineering

2011/2012

Contents

Glossary of Terms

1. **Anode**: An anode is an electrode through which electric current flows into a polarized electrical device. The direction of electric current is, by convention, opposite to the direction of electron flow.

2. **Austenitic Steel:** Austenitic steels have austenite as their primary phase (face centered cubic crystal). These are alloys containing chromium and nickel (sometimes manganese and nitrogen). Austenitic steels are not hardenable by heat treatment.

3. **Band Gap:** It is an energy range in a solid where no electron states can exist. It is called an energy gap or band gap.

4. **Cathode:** A cathode is an electrode through which electric current flows out of a polarized electrical device.

5. **Coefficient of Thermal Expansion:** Thermal expansion is the tendency of matter to change in volume in response to a change in temperature. The degree of expansion divided by the change in temperature is called the material's coefficient of thermal expansion and generally varies with temperature.

6. **Electrolyte:** An electrolyte is any substance containing free ions that make the substance electrically conductive. The most typical electrolyte is an ionic solution, but molten electrolytes and solid electrolytes are also possible.

7. **Etching:** Etching is the process of using strong chemicals to cut into the unprotected parts of a material’s surface.

8. **Hydrogen Bubbling:** In the electrodeposition of metals, a widely used industrial technique, bubbles of gas generated near the cathode can adversely affect the quality of the metal coating.

9. **INOX Steel:** Stainless steel is also known as inox steel or inox from French word "inoxydable", is defined as a steel alloy with a minimum of 10.5% to 11% chromium content by mass.

10. **Internal Stress:** Internal stress is a measure of the internal forces acting within a deformable body. Quantitatively, it is a measure of the average force per unit area of a surface within the body on which internal forces act.

11. **Lattice Distortion:** Structural disorder resulting from misalignment of the unit cells within the crystals.

12. **MEMS:** A Microelectromechanical system is the technology of very small devices; it merges at the nano-scale into nanoelectromechanical systems (NEMS) and nanotechnology. MEMS are made up of components between 1 to 100 micrometres in size (i.e. 0.001 to 0.1 mm), and MEMS devices generally range in size from 20 micrometres (20 millionths of a metre) to a millimetre (i.e. 0.02 to 1.0 mm).

13. **Molecular Beam Epitaxy:** It is one of several methods of depositing single crystals. Molecular beam epitaxy takes place in high vacuum or ultra-high vacuum (10−8 Pa). The most important aspect of MBE is the slow deposition rate (typically less than 1000 nm per hour), which allows the films to grow epitaxially. The slow deposition rates require proportionally better vacuum to achieve the same impurity levels as other deposition techniques.

14. **Photolithography:** It is a process used in microfabrication to selectively remove parts of a thin film or the bulk of a substrate. It uses light to transfer a geometric pattern from a photomask to a light-sensitive chemical "photoresist", or simply "resist," on the substrate. A series of chemical treatments then either engraves the exposure pattern into, or enables deposition of a new material in the desired pattern upon, the material underneath the photo resist.

15. **PVD:** Physical vapor deposition is a variety of vacuum deposition and is a general term used to describe any of a variety of methods to deposit thin films by the condensation of a vaporized form of the desired film material onto various workpiece surfaces . The coating method involves purely physical processes such as high temperature vacuum evaporation with subsequent condensation, or plasma sputter bombardment rather than involving a chemical reaction at the surface to be coated as in chemical vapor deposition.

16. **Sputtering:** Sputtering is a process whereby atoms are ejected from a solid target material due to bombardment of the target by energetic particles. It is commonly used for thin-film deposition, etching and analytical techniques.

17. **Stacking Faults:** A defect in a face-centered cubic or hexagonal close-packed crystal in which there is a change from the regular sequence of positions of atomic planes.

18. **Sulfur Embrittlement:** Also known as Red-short or hot-short is the quality possessed by carbon steel that suffers from having too much sulfur as an impurity.

List of Figures

Figure 20: Typical cyclic voltammogram where i_{pc} and i_{pa} show the peak cathodic and anodic current respectively for a reversible reaction.

Figure 21: Schematic Diagram of SEM.

Figure 22: Vickers Pyramid Indenter.

Figure 23: Indentation Impression after Vickers Hardness Test.

Figure 24: Vickers Microidentation Instrument.

Figure 25: E–t transients of NiCo electrodeposition at different current densities: (a) j = −10 mA cm^{-2}, T = 50° C, (b) j = −30 mA cm^{-2}, T = 50° C, (c) j = −50 mA cm^{-2}, T = 50° C, (d) j = -10 mA cm^{-2}, T = 40° C, (e) j = −10 mA cm^{-2}, T = 30° C.

Figure 26: SEM picture of a NiCo deposit obtained at j = −10 mA cm^{-2} , T = 50 ° C.

Figure 27: Two details of the X-ray diffractograms of NiCo deposits obtained at 50 ° C and: curve (a) j = −10 mA cm^{-2}; curve (b) j = −50 mA cm^{-2} .

Figure 28: Dependence of the microhardness (A) and Young's modulus (B) with the temperature for NiCo deposits obtained at j = −10 mA cm^{-2}.

Figure 29: Magnetisation vs magnetic field applied for NiCo samples prepared at: (A) j = −10 mA cm−2 , T = 50 ° C, (B) j = −50 mA cm−2 , T = 50 ° C, (C) j = −10 mA cm−2 , T = 40 ° C.

Figure 30: Chemical composition of the composites by EDS.

Figure 31: Typical composite in SEM imaging: (A) microstructure (5 g/l $BaFe_{12}O_{19}$), (B) surface topology (20 g/l $BaFe_{12}O_{19}$).

Figure 32: AFM surface morphology of composites: (A) 0 g/l – Ra = 3.9 nm, (B) 5 g/l – Ra = 23 nm, (C) 15 g/l – Ra = 30 nm.

Figure 33: FCC structure of the NiCo, all solid solutions by XRD: pure matrix (lower curve) and all composites (upper curves up to 20 g/l).

Figure 34: Nano-grained NiCo matrix by LVSTEM.

Figure 35: Particle distribution in the NiCo matrix by LVSTEM.

Figure 36: Particle agglomeration by TEM.

Figure 37: Columnar crystal growth at the surface of a NiCo composite: (A) SEM image, (B) EBSD results (quality map, orientation map, grain size distribution, (111) fibre texture // layer normal).

Figure 38: Magnetization vs field curves at room temperature for NiCo and the composite: (A) out-of plane measurement – matrix property, (B) in-plane measurement – influence of the particles.

Figure 39: SEM images of coatings with particle's load of 0 and 5 g L^{-1}: (A) NiCo alloy, (B) NiCo/5 g L^{-1} Ba–Sr ferrite, (C) NiCo/5 g L^{-1} Ba–Sr ferrite (zoom), (D) NiCo/5 g L^{-1} Ba–Sr ferrite (EDS spectrum of zoom area), (E) NiCo/5 g L^{-1} Ba–Sr ferrite (mapping of iron presence in the surface).

Figure 40: Detail of the cross-section of : (A) NiCo /5 g L^{-1} Ba–Sr ferrite and (B) NiCo/10 g L^{-1} Ba–Sr ferrite.

Figure 41: Diffraction peaks of (A) NiCo, (B) NiCo/5 g L^{-1} particles, (C) NiCo/5 g L^{-1} particles – zoom area.

Figure 42: HV vs load of particles (A) and Young modulus vs load of particles (B).

Figure 43: M–H curves Ba–Sr ferrites, (A) before, and (B) after immersing them in the electrolyte solution.

Figure 44: M–H curves for (A) NiCo and (B) NiCo/15 g/L Ba–Sr ferrite.

Figure 45: A) E–t transients of the galvanostatic deposition of (a) NiCo nanowires, (b) NiCo/ferrite nanowires and SEM images of the resulting nanowires (B) and nanowires composite (C) into the alumina membrane.

Figure 46: X-ray diffractograms of the nanowires and zoom details.

Figure 47: Magnetization–magnetic field applied with the membrane parallel (a) or perpendicular (b) to the magnetic field. A) NiCo nanowires, B) NiCo/ferrite composite nanowires.

Figure 48: TEM pictures of the resulting composite nanowires.

List of Tables

Abstract

The continuing trend towards further miniaturization as well as increased functionality of electronic microelectromechanical (MEMS) devices fuels the demand for advanced materials [1 - 4]. Magnetic materials have found a large number of applications in MEMS as actuators, mini-pumps and micro-motors due to their reversibility, high actuation speed and effectiveness over long-distances [5, 6]. Soft magnetic materials are more abundant in the market today [7-11], but permanent magnetic elements, requiring hard magnetic materials find increasingly attention [12, 13]. Of special interest in this context are composite materials consisting of a matrix with embedded nano-particles. This could open a route to obtain materials that combine hard magnetic properties with the high saturation magnetization achievable in soft magnets.

Several techniques for depositing hard-magnetic materials are under study worldwide. Screen printing, sputtering and electroplating are some examples of micro-machining techniques used today. Electrochemical deposition (ECD) has proved to be one of the most versatile and cost-effective techniques [14, 15] for MEMS applications. Ni-Co is one of the most commonly used matrixes to form magnetic materials. Compared to Ni and Co composite layers, there are few studies related to composites of alloys by ECD [16]. Barium-ferrite-nickel-cobalt composites have been prepared from an optimized bath solution [17 - 19]. Nevertheless, the incorporated particles had micron or larger size. Surfactants were used to prevent agglomeration of the suspended particles and provided 12 wt% barium ferrite incorporation; however surfactants are detrimental factors concerning matrix properties [17]. The cationic dodecyl trimethyl ammonium chloride (DTAC) [20, 21] and cationic azobenzene moiety (AZTMAI) [22, 23] were used to reduce surfactant incorporation. Pure NiCo deposits have been formed in an AZTMAI containing bath [24], although the structure of the deposits were modified [25].

In the present work the electro-codeposition of NiCo matrixes with incorporated barium strontium ferrite nanoparticles using a sulfamate bath is examined. For different deposition parameters composition, structure and mechanical properties were studied.

Chapter 1: STATE OF ART

1. State of Art

1.1 Electrodeposition and Electroforming

1.1.1 Electrodeposition

Metal electrodeposition is often referred to as electro-plating, and has long been important commercially. It is a highly versatile technique, being used for applications ranging from the deposition of coatings for corrosion protection to the fabrication of Permalloy thin film recording heads [26 - 30]. Even when film thickness must be controlled on the scale of a few angstroms, for some applications electrodeposition is a viable alternative to Molecular Beam Epitaxy or sputtering.

Deposition takes place in an electrochemical cell containing metal ions in solution. The ions receive electrons from one of the electrodes (the cathode) and are thereby reduced to the corresponding metal. A typical metal electrodeposition reaction is shown below:

$$Ni^{+2}_{(aq)} + 2e^{-} \rightarrow Ni_{(s)}$$

1.1.2 Electroforming

Electroforming is the fabrication of simple and complicated components by means of electroplating where the electrodeposited material is required to be separated from the electrode itself. The basic fabrication steps are as follows:

1. A suitable mandrel is fabricated and prepared for electroplating;
2. The mandrel is placed in the appropriate electroplating solution and metal is deposited upon the mandrel by electrolysis;
3. When the required thickness of metal has been plated, the metal-covered mandrel is removed from the solution;

4. The mandrel is separated from the electrodeposited material which may be a metal or an alloy or a composite.

The electroform is a separate, free-standing entity composed entirely of electrodeposited material. The standard definition adopted by ASTM Committee B8 is that "electroforming is the production or reproduction of articles by electrodeposition upon a mandrel or mold that is subsequently separated from the deposit".

1.1.2.1 Advantages and Limitations of Electroforming

The predominant advantage of electroforming is the accuracy achieved with it. The general tolerance is 0.005 mm [31 - 33]. Besides it can be used for the production of bores and grooves at a minimal measurement of 0.032 mm. As in etching, here also highly complex forms can be produced as long as it's possible to sketch. It is possible to obtain electroforms of complex shapes using expendable mandrels.

The primary limitation is the scalability of the process. It is also fairly difficult to ensure uniform composition regardless of shape [34 - 36].

1.2 Nickel Electroforming

The Nickel electroplating solutions commonly used for electroforming are the Watts, and conventional and concentrated Nickel sulfamate solutions with and without addition agents. Nickel fluoborate solutions are used, but their popularity appears to be declining. From a commercial perspective, the most important ones are those based on Nickel sulfamate. The advantages of Nickel electroforming from sulfamate solutions are the low internal stress of the deposits and the high rates of deposition that are possible, especially from the concentrated solution (Ni-Speed) [37 - 40].

1.2.1 Properties of Electroformed Nickel

The mechanical properties of electroformed Nickel are influenced by the operating variables - pH, temperature, and cathode current density. The constituents of the solution, if their concentrations are not kept within specified limits, and relatively small amounts of metallic impurities can, also, affect mechanical properties. The properties are interrelated and steps taken to increase the hardness of the deposit usually increase its strength and lower its ductility [41]. The refinement of crystal structure, for example by the use of organic addition agents, is accompanied by increased hardness and tensile strength, and reduced ductility. Typical properties of deposits from various additive-free baths are included in Table 1.

Electrolyte Composition (g/l)			
	Watts Nickel	Conventional Sulfamate	Concentrated Sulfamate
$NiSO_4.6H_2O$	225 to 300	-	-
$Ni(SO_3NH_2)2.4H_2O$	-	315 to 450	500 to 650
$NiCl_2.6H_2O$	37 to 53	0 to 22	5 to 15
H_3BO_3	30 to 45	30 to 45	30 to 45
Operating Conditions			
Temperature, °C	44 to 66	32 to 60	Normally 60 or 70
Agitation	Air or Mechanical	Air or Mechanical	Air or Mechanical
Cathode Current Density, A/dm^2	3 to 11	0.5 to 32	Up to 90
Anodes	Nickel	Nickel	Nickel
pH	3.0 to 4.2	3.5 to 45	3.5 to 4.5
Mechanical Properties			
Tensile Strength, MPa	345 to 485	415 to 620	400 to 600
Elongation, %	15 to 25	10 to 25	10 to 25
Vickers Hardness, 100 g load	130 to 200	170 to 230	150 to 250
Internal Stress, MPa	125 to 185 (tensile)	0 to 55 (tensile)	Zero stress can be obtained at various combinations of current density and temperature

Table 1: Typical Nickel Electroforming Solutions and General Properties of the respective Deposits.

Some of the properties of Nickel deposited from Watts and conventional Nickel sulfamate solutions are influenced by operating variables. Deposits from these types of Nickel baths are affected differently by the same variables. For example, in the Watts solution tensile strength is relatively independent of plating solution temperature, pH and cathode current density; it increases with increasing Nickel and chloride in solution. In the sulfamate solution, tensile strength decreases with increasing temperature to 50°C, increases with increasing pH, and decreases with increasing cathode current density; it decreases slightly

with increasing Nickel and chloride in solution. The operating variables, as well as the specific constituents, affect the properties of electroformed Nickel.

In addition, the mechanical properties, especially the percent elongation or ductility, are affected by the thickness of the electroformed Nickel used in determining the properties. The ductility increases with increasing Nickel thickness up to about 250 micrometers after which it becomes relatively constant [42 - 44]. This was shown in the classic work by Zentner, Brenner and Jennings in 1952 for deposits from Watts solutions and is also true for Nickel deposits from sulfamate solutions. Mechanical testing should be done at the thickness of interest even though it may be more convenient to test thick deposits.

The properties of Nickel electroformed from sulfamate solutions can be affected by uncontrolled anode behavior, which results in the oxidation of the sulfamate anion. The oxidation products can lower the internal stress and increase the sulfur content of the deposits. The extent to which these changes in internal stress and sulfur content affect the ultimate tensile strength and per cent elongation of sulfamate Nickel electrodeposits has been studied by Chart in 1977 [45]. In the study by Chart, Nickel sulfamate deposits with tensile internal stress were obtained from conventional solutions; the stress was stable at 50MPa. The solution contained 70 g/l of Nickel metal as the sulfamate, 0.1 g/l of chloride added as Nickel chloride hexahydrate, and 35 g/l boric acid. The pH was 4.0, temperature 60°C, and cathode current density 540 A/m_2; the bath was operated with air agitation. After the tensively stressed deposits were prepared over a range of thicknesses, similar compressively stressed deposits were prepared by including a platinum foil anode in the circuit and passing 1 to 2 per cent of the total current through the auxiliary anode, the current density on the auxiliary anode was 2.7 A/m^2. This procedure gave deposits with an internal stress that was 71 MPa in compression. The ultimate tensile strength varies with Nickel thickness but becomes stable above 250 micrometers. The strength of the compressively stressed deposits is greater than that of the tensively stressed deposits. Annealing at 371°C for 2 hours lowers the tensile strength of the compressively stressed and tensively stressed deposits to approximately equal values. Annealing at the higher

temperature lowers the tensile strength even further, but the decrease is significantly greater in the case of the compressively stressed deposits.

The ductility showed greater variation with thickness than does the ultimate tensile strength. The ductility was greater for the tensively stressed deposits than for the compressive ones in the as-plated condition. Annealing at 371°C increases the ductility of both types of deposits. Annealing at 760°C increases the ductility of the tensively stressed deposits, but lowers the ductility of the compressively stressed ones to values below the as-plated ones [45]. The measurements of ultimate tensile strength and per cent elongation (ductility) were made by standard uniaxial tension testing. The deposits were also analyzed chemically. The tensively stressed deposits contained less than 1 part per million sulfur, whereas the compressive deposits contained about 40 parts per million sulfur [46 - 48]. Metallographic and electron microprobe analyses conducted after annealing showed brittle failure in compressive deposits heated at 760°C, as well as high sulfur (380 to 500 ppm) contents in grain boundaries. The work established that the oxidation products formed at an insoluble platinum anode in sulfamate solutions lower internal stress and result in the codeposition of sulfur. The codeposition of small amounts of sulfur affects the mechanical properties of electroformed Nickel especially at high temperatures [49]. It is important to control the anode behavior to achieve consistent results in electroforming from sulfamate solutions.

1.2.2 Watts Solutions

The Watts bath contains Nickel sulfate, Nickel chloride and boric acid, and yields Nickel deposits that are matte in appearance and that are stressed in tension. The solution is relatively inexpensive and is successfully used for electroforming.

Nickel sulfate is the main source of Nickel ions in the Watts solution. Nickel chloride increases solution conductivity and has a beneficial effect on the uniformity of metal distribution at the cathode. Boric acid acts as a buffer to control pH at the cathode-solution

interface. Anti-pitting agents (wetting agents) are essential for avoiding pitting due to the clinging of air and hydrogen bubbles.

With considerable care, the internal stress of the electroformed Nickel can be controlled by means of organic addition agents. Typical stress reducers are saccharin, paratoluene sulfonamide, meta-benzene disulfonate, and 1-3-6 sodium naphthalene trisulfonate. All of these organic stress-reducing agents introduce sulfur into Nickel deposits and this limits the temperature at which the electroform can be used in service. Nickel electrodeposits with small amounts of sulfur become embrittled when exposed to temperatures above 200°C. The exact temperature of embrittlement depends on the sulfur content, the time at the elevated temperature and other factors. Control of internal stress by means of organic addition agents requires an optimum level of the additive, regular replenishment as it is consumed, and frequent (or continuous) carbon treatment to control the concentration of decomposition products which form as a result of reduction of the additive at the cathode.

1.2.3 Conventional Nickel Sulfamate Solutions

A formulation for conventional Nickel sulfamate solutions is included in Table 2. In essence, these are analogous to Watts solutions in which the Nickel sulfate is replaced with Nickel sulfamate. The internal stress is lower than in the Watts solution. The zero stress level may be obtained by maintaining the solution in a high state of purity and by eliminating the Nickel chloride. To assure efficient dissolution of Nickel anode materials in the absence of chlorides, it is essential to use sulfur-activated Nickel anode materials, such as S-Rounds electrolytic Nickel or S-Nickel pellets. Even with extreme care, a zero stress level may be difficult to maintain without using small amounts of the organic addition agents referred to above. The additives function in Nickel sulfamate, as well as in Watts, solutions.

A stable tensile stress can be maintained in conventional Nickel sulfamate solutions by including Nickel chloride in the formulation, by using an adequate anode area (1.5 to 2 times the area of the cathode), and by using a fully-active Nickel anode material to maintain the

potential on the anode basket as low as possible, thus avoiding oxidation of the sulfamate anion. Under these conditions, the stress level normally is between 35 and 55 MPa (5000 to 8000 psi) tensile for a well-worked solution.

1.2.4 Anodic Oxidation of Sulfamate Anions

A phenomenon, which apparently only occurs in sulfamate solutions, is anodic oxidation of the anion to form species, which diffuse to the cathode where they are reduced. In some cases, this results in incorporation of sulfur, which acts to lower internal stress and brighten the deposit. This occurs, for example, at insoluble primary or auxiliary anodes, or at Nickel anodes that are operating at high potentials.

At an insoluble platinum anode, a stress reducer forms which was identified as an azodisulfonate; it reacts at the cathode and introduces sulfur into the Nickel deposit. The use of a small auxiliary platinum anode along with primary anodes to control stress by passing one to two per cent of the total current through the platinum is feasible and has been evaluated on a laboratory scale; although stress was controlled at a low value (compressive), the work confirmed that sulfur co-deposits and affects the ductility and other mechanical properties of the Nickel, and its tendency to become embrittled when heated. The long-time effects of employing an insoluble auxiliary anode in this way have not been determined.

More than one sulfamate oxidation product may form. The one that forms depends on the anode potential. At an insoluble platinum anode, the electrode potential is high (1.2 volts vs. SCE), whereas in the concentrated solution (Ni-Speed) the electrode potential on the anode in the conditioning tank is controlled at a lower level, about 0.2 volts vs. SCE. The existence of several oxidation species in sulfamate solutions was confirmed by Chinese investigators in 1988.

1.2.5 Concentrated Nickel Sulfamate (Ni-Speed)

The concentrated Nickel sulfamate process, Ni-Speed, was developed by Inco Europe Limited. It permits the deposition of Nickel at high rates and at low stress levels in the deposit. It is particularly useful for electroforming where zero-stress conditions are required to produce perfectly flat electroforms and where thick deposits may be built up rapidly. Because low to zero-stress conditions can be achieved without organic addition agents, there is no incorporation of sulfur and the deposits do not become embrittled when heated above 200°C [48].

The composition of the solution is given in Table 1 which lists the acceptable operating limits.

1.2.6 Leveling Agents

The use of levelling agents, such as 2 butyne 1:4 diol, can improve metal distribution on the mandrel by suppressing the growth of nodules and by preventing the formation of a plane of weakness when electroforming into a corner. In general, levelling agents increase internal stress in the tensile direction. In the case of deposition of Nickel or Nickel-cobalt alloys from the concentrated solutions already discussed, it is possible to control the increase that results from the use of the levelling agent and achieve acceptable levels of internal stress. The initial concentration of butyne diol suggested for a concentrated solution with 1.25 g/L cobalt is about 20 mg/L with a replenishment rate of 0.5 mg/Ah at a current density of 3 A/dm$_2$. Although the breakdown products formed by organic addition agents generally increase internal stress, continuous filtration through carbon removes only the breakdown products in the case of butyne diol and the stress can be closely controlled with this additive.

1.2.7 Nickel Anode Materials of Unique Shapes

Some proprietary Nickel Anode materials include active Nickel anode materials with unique shapes, which are ideal for use in titanium anode baskets. The active ones are particularly useful for electroforming.

The active Nickel anode materials include S-Rounds electrolytic Nickel and S Nickel pellets. These products owe their activity to the small, controlled amount of sulfur incorporated during production. Activity refers to the anode potential, which these materials assume when they are dissolved anodically in various Nickel plating solutions. Sulfur-activated Nickel anode materials are very active. That is, they dissolve at the lowest electrode potentials for a specified current density.

The tendency for passivation associated with commercially pure Nickel is absent in the case of the sulfur-activated anodes. As a result, anodes like S-Rounds electronickel and S-Nickel pellets dissolve smoothly without the formation of metallic residues in all Nickel plating solutions irrespective of the chloride content. The low dissolution potentials save electrical power; the savings in power costs are significant. The uniformity of dissolution results in improved settling characteristics in the baskets. In addition to contributing to uniform current distribution, improved settling of the load in the basket protects the titanium from electrochemical attack. The nonmetallic residue that forms is insoluble Nickel sulfide, which displaces copper impurities from solution. Nickel plating solutions operated with S-Rounds or S-Nickel pellets always have unusually low copper present as an impurity for this reason.

The shapes of S-Rounds and of S-Nickel pellets button-shaped in the case of S-Rounds and spherical in the case of the pellets are also advantages. By eliminating sharp, pointed corners, settling of the load in the baskets is facilitated. The spherical shape has added advantages in that it facilitates the loading of odd-shaped baskets and baskets placed in other than the vertical position because the pellets tend to roll and flow. In fact, the flowability of pellets lends itself to the semi- or complete automation of the basketloading

operation. These anodes have relatively high packing densities, which minimize basket maintenance and contribute to power savings. An added benefit is that they can be handled safely.

Figure 1: S-Nickel Pallets.

Figure 2: Nickel S-Rounds.

As mentioned, sulfur-activated Nickel anode materials are preferred for electroforming from Nickel sulfamate solutions because they prevent the uncontrolled formation of sulfamate oxidation products, which affect internal stress, appearance, mechanical properties and composition of the deposits. In addition, active Nickel anode materials make it possible to operate Nickel electroplating processes with little or no chloride ions in solution. This is an alternate means of reducing internal stress during electroforming since chloride ions are known to increase stress.

Sulfur-free, non-activated electrodes are also used in electroforming and plating when chloride ions are present in solution. The unique shapes of R-Rounds, Nickel Pellets, and Nickel Flats make these electrodes ideal for filling titanium anode baskets safely. The absence of sharp corners contributes to uniform settling of the load in baskets, which leads to the same advantages already described. All these anodes form small amounts of metallic residues, which are easily retained in anode bags. Being sulfur-free, these anodes dissolve

non-uniformly and at higher anode potentials than do the sulfur-activated anodes. The sulfur-free, non-activated forms of Nickel are popular for electroplating in general, but there is a decided preference for S-Rounds electrolytic Nickel and S Nickel pellets for electroforming.

1.2.8 Control Of Electroforming Processes

Successful electroforming requires careful control of the purity of the electrolyte and of the operating variables, such as pH, current density, temperature and agitation. In this respect, control is similar to that of decorative Nickel electroplating. Control is more difficult and perhaps, more critical in the case of electroforming because processing may take hours or days to complete. The common problems encountered in electroforming include controlling metal distribution, internal stress, roughness and nodular formation. Addition agents may help overcome some of these problems, but their concentrations must be closely controlled.

1.2.8.1 Metal Distribution

The variation of the thickness of the metal deposited at various points on the surface of a mandrel is related to current distribution. Recessed areas will receive less current; areas that project from the surface will receive higher current. The current density and the rate of metal deposition will be lower in recessed areas than at areas, which project from the surface. The result is that metal distribution will be non-uniform in many cases. The deposit will be relatively thin in recessed areas and relatively thick on projections.

Some electroplating solutions are less sensitive then others to variations in current density. The capability of a plating solution to deposit uniformly thick deposits despite variations in current density on the surface of an electroform is measured by its throwing power. Throwing power is the relationship between metal distribution and the variables-conductivity, polarization, current efficiency, and geometry. Studies of the throwing power of Nickel plating solutions suggest that throwing power can be improved by reducing current density, by increasing the distance between anode and cathode, and by increasing

the pH, temperature, and metal content of the bath. All-chloride Nickel plating solutions (which are not used for electroforming because of the high internal stress of the deposits) have better throwing power than Watts solutions. Sulfamate solutions are better than Watts solutions but not as good as the all-chloride solutions.

The Nickel process selection should be based on the mechanical and physical properties specified, rather than throwing power. Metal distribution is then improved by proper racking, and by the use of thieves, shields, and/or conforming or auxiliary anodes. The use of these processing aids makes it possible to control metal distribution and obtain relatively uniform deposits. Although these techniques are optimized by trial and error, simulation of the electroforming operation combined with the determination of cathode potential profiles can facilitate the design and placement of shields and auxiliary anodes. Computer software is available to help improve metal distribution at the cathode.

1.2.8.2 Internal Stress

The control of internal stress is extremely important in electroforming. Internal stress refers to forces created within an electrodeposit as a result of the electrocrystallization process and/or the codeposition of impurities such as hydrogen, sulfur and other elements. The forces are either tensile (contractile) or compressive (expansive) in nature; rarely are electrodeposits free of some degree of internal stress. Excessive tensile or compressive stress can cause the following problems [46]:

1. distortion of the electroform when it is separated from the mandrel
2. difficulty of separating the electroform from the mandrel
3. curling, peeling or separation of the electroform prematurely from the mandrel
4. buckling and blistering of the deposit which is usually indicative of high compressive stress.

Internal stress is influenced by the nature and composition of the Nickel plating solution as shown in Table 2.

Electroforming Solution	Internal Stress, MPa
Watts	110 to 210
Watts with Hydrogen Peroxide	275 or higher
All-Chloride	205 to 310
Fluoborate	100 to 175
Fluoborate with hydrogen peroxide	100 to175
Sulfamate, no Chloride	0 to 55
Sulfamate, with Chloride	55 to 85
All-Sulfate	110 to 140

Table 2: Typical Values of Internal Stress for Nickel Electroforming Solutions [48].

The all-chloride solution produces deposits with the highest internal stresses. Nickel sulfamate solutions without chlorides produce deposits with the lowest internal stresses. Organic additives can be used to control internal stress of electrodeposited Nickel, but since these additives invariably introduce sulfur they must be used with caution and due consideration. Sulfur codeposited with Nickel increases its hardness and strength, and reduces ductility. Sulfur affects the high temperature properties adversely, and Nickel deposits with sulfur cannot be heated above 200°C without becoming embrittled. The codeposition of small amounts of manganese has been shown to prevent embrittlement of sulfur-containing Nickel electrodeposits and allows heating above that temperature. The concentrated Nickel sulfamate process discussed above can be operated at high current densities to yield deposits with very low or zero internal stresses, the techniques being shown to be effective with Nickel as well as Nickel-cobalt alloy electroforming.

Internal stress is controlled by specifying the electrolyte and maintaining its purity, and by using organic addition agents. Control of current density and the other operating variables is also important.

1.2.8.3 Roughness

Any condition, which would tend to cause roughness in decorative plating will have a much more serious effect on electroforming operations. Nodules, nuggets and trees will form. These become high current density areas, and the larger they get, the faster they grow and the more they rob surrounding areas of deposit [47]. As a consequence, the filtration rates used in electroforming are very high in an effort to prevent roughness; the rates may amount to passing the entire solution through a filter one or more times an hour.

The sources of roughness include airborne dirt. It is good electroforming practice to keep the plating area clean by vacuum cleaning and to supply the plating room with filtered air keeping the room under an inch or so of pressure. These precautions are especially necessary when the plating tank has an exhaust system, which draws air across the bath [46].

Electroformed stampers for making compact discs are made in clean rooms under exacting conditions of cleanliness. Anode particles may also cause roughness and are controlled by means of anode bags and diaphragms; higher filtration rates and cathode agitation may be beneficial. The crystallization of bath chemicals on anode bags, tank walls and super-structures which may form at low temperatures or because of inadequate solution agitation may cause roughness problems when these particles fall or are brushed into the solution. The crystallized salts tend to dissolve slowly and may become attached to the cathode. Accumulated salts should be removed carefully or washed away when the bath is not in use. Deionized water should be used to make up the plating and rinsing solutions to avoid the formation of particles from precipitation of hard water constituents.

1.2.8.4 Treeing

Treeing at edges and corners may be troublesome and is minimized by the use of shields or by the choice of electrolyte; for example, high-chloride solutions are better than Watts baths in this respect. Certain addition agents, such as the levelling agents discussed above, suppress the treeing tendency. Another approach applicable in many cases is to extend the mandrel beyond the dimensions actually desired, so that the treeing occurs on a part of the electroform that can be machined away. If Nickel electroforming is interrupted to remove trees and nodules by machining, the machined Nickel surface must be activated to insure good Nickel-to-Nickel adhesion. Methods of preparing Nickel surfaces for deposition with Nickel have been standardized (ASTM Standard B 343).

1.2.8.5 Other Control Techniques

Agitation of every kind, singly or in combination should be employed whenever possible to control burning and pitting at high current density sites. Solution agitation, either air or mechanical, may induce roughness, however, unless the solution is kept clean by using a high filtration rate. Cathode rotation, when applicable, is an effective means of solution agitation. In addition, cathode rotation can ensure uniformity of deposit thickness from point to point around the circumference. (Inequalities along the axis of rotation have to be overcome by other means). When rotation is used, brushes or other commutating devices must be provided to conduct current to the cathode. Care must be taken that these devices are designed so that no lubricating grease or metal particles resulting from the wear of bearing surfaces fall into the plating solution.

1.2.9 Post-Electroforming Operations

The operations that are performed after electroforming is completed are machining and final finishing of the electroform; parting or separation of the electroform from the mandrel, and backing the electroform.

1.2.9.1 Machining and Finishing

Necessary machining or other mechanical finishing operations are usually performed before the electroform is separated from the mandrel to avoid deformation. The machining and grinding of electrodeposited Nickel may be difficult. Directions for machining and grinding of Nickel and other electrodeposits have been published [41].

1.2.9.2 Parting

Electroforms are removed from permanent mandrels mechanically by the use of one or a combination of several of the following techniques:

1. Impact, by a sudden pull or hammer blow.
2. Gradual force, applied by a hydraulic ram to push, or a jack-screw or wheel-puller to pull the pieces apart.
3. Cooling, for example with a mixture of dry ice and acetone. This works best if the mandrel has a lower coefficient of expansion than the Nickel. On withdrawal from the cold bath, the electroform will expand faster than the mandrel permitting separation.
4. Heating, with a torch or hot water or oil bath, either to melt or soften a parting compound or to take advantage of a difference in coefficients of expansion between mandrel and electroform.
5. Prying, with a sharp tool may be used with care to separate relatively flat pieces, such as phonograph record stampers or engraving plates.

Expendable mandrels are melted or dissolved out as follows:

1. Zinc alloys are dissolved with hydrochloric acid.
2. Aluminum alloys are dissolved in strong, hot sodium hydroxide solutions.
3. Low-melting alloys are melted and shaken out. The alloy may be collected and used over. If tinning occurs, a Nickel electroform may be cleaned with strong nitric acid.
4. Plastics of the thermoplastic kind may be softened by heat so that the bulk of the mandrel may be withdrawn, after which the electroform is cleaned with a suitable solvent. An alternative is to dissolve the entire mandrel with a solvent.

The separation of mandrel and electroform should be considered at an early stage since the separation can be simplified by certain design changes. A fine surface finish facilitates parting. Gripping devices may be incorporated on the mandrel and a knock-off block may be provided so force can be applied for separating the mandrel and the electroform. A taper can be specified when feasible.

1.2.9.3 Backing the Electroform

It is often necessary to back the electroform with some other material which is then finished to specified dimensions to fit into a bolster or onto a printing press. This is true, for example, in the case of molds, dies, printing plates and tools in general.

The most important backing methods include the following [50]:

1. casting with low-melting temperature alloys
2. spraying with various materials
3. electroplating with other metals
4. use of thermosetting resins
5. spark-eroded steel back-ups and electrochemical machining techniques that sink conforming cavities in the back-up material.

1.3 Electrochemical Deposition of Ni-Alloys

1.3.1 Nickel-Cobalt Alloy Plating

The physical facilities for electroforming Nickel-Cobalt alloys do not differ appreciably from those for Nickel.

Nickel-cobalt alloys can be deposited from concentrated Nickel sulfamate solutions with controlled internal stresses. The cobalt in solution can be maintained by the addition of cobalt sulfamate or by using electrolytic cobalt anodes connected to a separate power

supply alongside the Nickel anodes. The codeposition of cobalt increases the hardness and strength, and enhances the high temperature properties of the deposits [51, 52]. The cobalt content of the deposit rises with increasing amounts of cobalt in solution and declines as the current density increases. As the cobalt content of the solution is increased, the hardness of the deposit increases to a maximum value. The peak occurs at 35 per cent cobalt in the deposit which corresponds to about 6 g/l cobalt in solution [53, 54]. The internal stress of the deposit increases with current density and also with cobalt content of the solution.

It can be seen that there are a number of conditions under which Nickel- cobalt can be deposited with zero stress and these are listed in Table 3:

Cobalt Concentration in Solution, g/l	**Current Density, A/dm^2**
0.75	10
1.0	7.5
1.25	5.1
1.5	3.0

Table 3: Plating Conditions at 60°C for Zero Stress Deposits in Cobalt-Containing Concentrated Nickel Sulfamate Solutions [55].

Nickel-cobalt alloys can be deposited from conventional Nickel sulfamate solutions and from Nickel sulfate-based solutions, but the deposition of the alloys from the concentrated solution provides a means to control the internal stress without the use of organic addition agents.

1.3.2 Metallurgical Considerations of NiCo Alloys

Nickel Cobalt electrodeposited alloys have very good room temperature properties, although ductility is usually poor and inversely proportional to the ultimate strength when the material has not been heat-treated. Heat-treatment temperatures normally do not exceed 400°C to obtain the best room-temperature properties. Nickel-Cobalt alloys afford some of the best electrodeposited materials for retention of strength after exposure to elevated temperatures for short times. However, mechanical properties at elevated temperatures degrade rapidly becoming no better than conventional electrodeposited Nickel at temperatures approaching 375°C as shown in Figure 3. This is a result of unit cell changes that take place in the crystallographic lattice structure at this temperature.

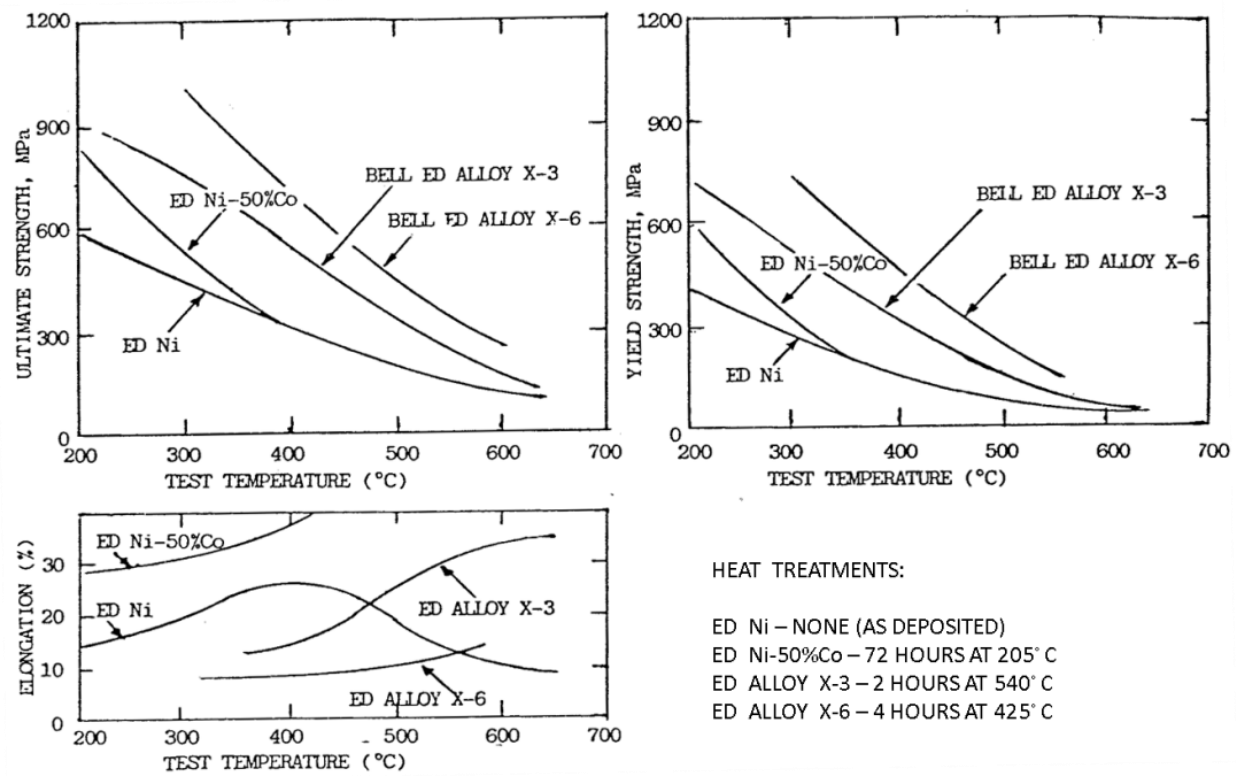

Figure 3: A comparison of Mechanical Properties of electroformed Nickel and Alloys over an elevated test Temperature range [45].

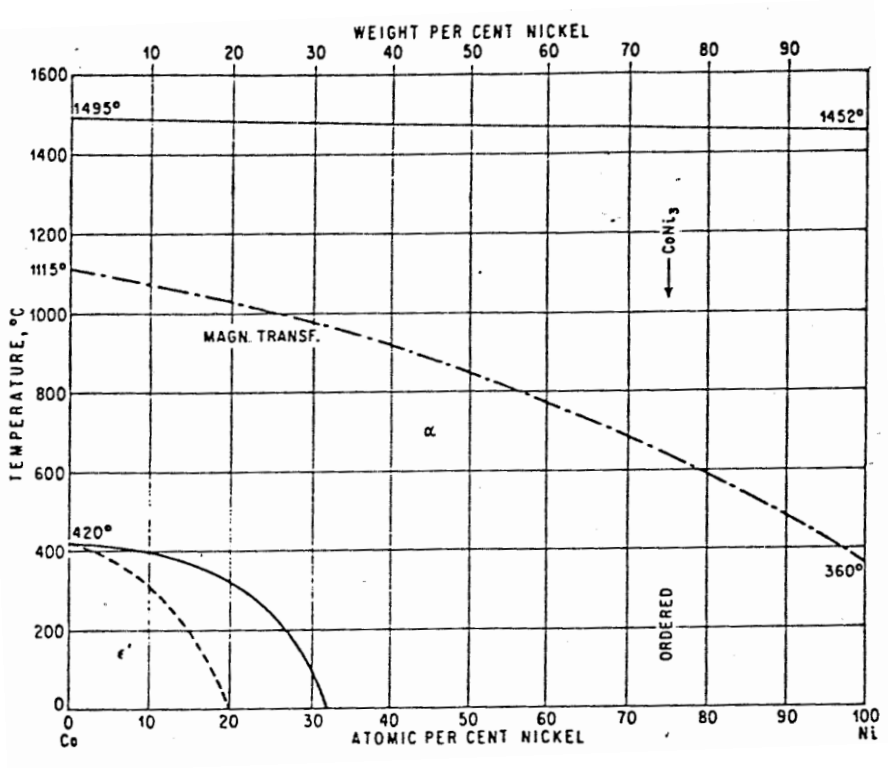

Figure 4: Cobalt Nickel Binary Phase Diagram [45].

This area has been of great interest because all of the mechanical behavior changes in electroformed Nickel-Cobalt result from thermal excursions through this zone. These effects may be brought about by fabrication operations such as welding or brazing, as well as service applications where elevated temperatures may be involved. In general, as the temperature is increased, the mixed cell structure in the peritectic zone becomes increasingly FCC until the α region is reached where it becomes all FCC. Upon cooling, a transformation again occurs to the mixed structure. However, not all of the original HCP structure is regained.

The unusual mechanical strength of Nickel-Cobalt electrodeposits can only be attributed to the presence of Cobalt and Cobalt-Nickel cells of the HCP type. Microstructures of metals and alloys with mixed HCP and FCC cells are usually characterized by a type of lattice distortion and disordering known as “stacking faults”. This is likely to be what influence the band gap [46]. The amount of banding may be an indication of how much HCP structure is

present. These bands diminish with heat-treatment – disappearing when the treatment temperature is high. When the bands disappear, the strength retention is not appreciably greater than that of electrodeposited Nickel.

1.3.3 Metal Matrix Composites and Other Innovations

Electroplating processes that result in the incorporation of particles uniformly dispersed throughout an electrodeposited metal matrix have been investigated in connection with electroforming. By careful selection of the particle to be occluded, it is possible to obtain Nickel electroforms with unique mechanical and physical properties. Oxides, nitrides, carbides and borides have been incorporated in Nickel and Nickel alloy deposits to produce high-temperature, oxidation-resistant materials. The codeposition of mica with Nickel results in a deposit with a low coefficient of friction. The incorporation of fibers in metal matrices by means of electrodeposition is also possible and is receiving renewed attention at this time [56 - 58].

Electroless Nickel processes have, until recently, been considered unsuitable for forming applications because of the lack of ductility of the deposits. Bellows have, however, reportedly been successfully formed electrolessly [59].

The possibility of creating articles with unusual properties through the incorporation of metallic and non-metallic particles and fibers, either electrolytically or electrolessly, exists and may extend the utility of electroforming even further.

Several studies have been carried out to study electroformed composites with dispersed particles [55, 56, 60 - 64]. Studies have also been carried out on electrochemical deposition of minute devices such as MEMS [65 - 68] and Nanowires [69].

1.4 Applications of Magnetic Composites

Magnetic materials have received much attention in recent years because their extensive technological applications in micro- electronics industry. A particular research study was focused on ferromagnetic materials [70–73]. Ferrite materials are used is a variety of components. Advanced magnetic composites such as the ones being studied here will enable further miniaturization and use of new design concepts. Several devices use electrochemically deposited coatings with novel magnetic properties [74 - 76], some of which are composites which combine hard magnetic properties with high saturation magnetization achievable in soft magnetic materials [77]. In particular, the use of cobalt–nickel system has been extended to some magnetic applications, especially in microsystems technology for manufacture of sensors, actuators or inductors [78–80], and their use has been tested as magneto-optic memory material as very desirable data storage material [81,82].

Following are some examples of devices which could benefit from development of new magnetic composites:

1. TV scanning yoke
2. UR core and TV line output transformer
3. E-core for switched mode power supply
4. Wide band transformer core
5. Core giving good magnetic shielding
6. High Q filter core
7. Precision ferrite antenna for transponder
8. Multilayer EMI suppressors
9. Toroids for laser and radar pulse applications
10. Typical EMI shields for cables
11. Loudspeaker and field magnets
12. Hard ferrite–polymer composite.

Chapter 2: EXPERIMENTATION

2. Experimentation

2.1 Formulation of Electrolyte

Three batches of NiCo elecroforming solution was made of 2000ml each.

Following was the composition of the various constituents:

S. No.	Name	Physical State	Concentration in Original Solution	Concentration in Electrolyte
1	Nickel Sulfamate Solution	Liquid Solution	180 g/l	55 g/l
2	Cobalt Sulfamate Solution	Liquid Solution	17.63 g/l	10 g/l
3	Saccharine	Solid – Powder	-	1.5 g/l
4	Boric Acid	Solid – Powder	-	36 g/l
5	Sodium Lauryl Sulfate (SLS)	Solid – Powder	-	0.15 g/l

Table 4: Composition of the bath.

For each batch of 2000ml of NiCo Electrolyte the following procedure was followed:

1. A 3000ml conical flask was taken, cleaned with distilled water, wiped dry and placed on an electric heater with built-in magnetic stirrer.
2. 610ml of the Nickel Sulfamate solution was introduced into the flask.
3. 1135ml of Cobalt Sulfamate solution was added to the flask.
4. A Magnetic Rod was slipped into the flask.

Figure 5: Magnetic Rod for Magnetic Stirring.

5. A feedback-thermometer was placed and fastened in place using a stand and clamp. The thermometer wire connector was connected to the electric heater-stirrer.
6. The electric heater was started and adjusted to 70°C. The magnetic stirrer was adjusted to about 1000 RPM.
7. 72 g of Boric Acid powder was added to the solution.
8. After about 5 minutes, 3g of Sacchaarine was added.
9. After another 5 minutes, 0.3g of SLS was added to the solution.
10. 225ml of deionized water was added to the solution.
11. The solution was stirred until all the added solids were dissolved.
12. The pH was adjusted to 4. To increase the pH Sodium Hydroxide solution was added to the solution, while Sulfamic acid solution (H_3NSO_3) was added to reduce the pH. It was noted that the pH varied with temperature and had to be duly adjusted.
13. The evaporated water from solution increased the concentration of the constituents. Ionized water was added to adjust the volume to 2000ml.
14. The concentration of Nickel and Cobalt in the solution was tested periodically using an X-Ray Fluoresence Spectrometer.

Figure 6: The Velp Heater-cum-Magnetic Stirrer used for the Experiments.

2.1.1 Addition of $Fe_{12}O_{19}Ba_{0.2}Sr_{0.8}$

$Fe_{12}O_{19}Ba_{0.2}Sr_{0.8}$ nanopowder by Sigma-Aldrich of 99.5% purity of nominal diameter 5nm was used in various concentrations to study their incorporation into the NiCo matrix.

Following were the concentrations used in the various experiments:

1. For Electroforming of Films on INOX Steel: 0g/l, 1g/l, 5g/l, 10g/l, 15g/l and 20g/l
2. For Electrodeposition of Nanowires: 0g/l and 1g/l

0g/l concentration indicates that a pure NiCo sample was obtained to act as the control sample in each type of cell.

In each of the remaining cases, specific concentrations of $Fe_{12}O_{19}Ba_{0.2}Sr_{0.8}$ nanopowder was added to the solution, stirred mechanically and ultrasonically treated for 15 minutes for better particle dispersion.

2.2 Preparation of Cathodes

2.2.1 Electrode for NiCo Films

The Electrodeposited NiCo films were required to be easily "peeled off" for easy analysis. As a result INOX Steel was selected as the cathode. The lower surface energy in INOX Steel ensures that the deposited film (of a substantial thickness) will peel off at the end of the deposition process.

The following steps were taken to prepare the Cathode:

1. A 30mm x 250mm piece of INOX Steel of thickness 0.6mm was taken.
2. It was cleaned using deionized water and dried using compressed air.
3. A Kapton tape was used to insulate all the surfaces barring a rectangular region of 25mmx 30mm and 20mm on all sides from the top portion of the strip to allow connection. This left an exposed rectangular area of 7.5 cm^2 on which deposition could take place.
4. It was ensured that the layers of the Kapton tape were appropriately stuck in order to avoid air-bubbles and leakages which could inadvertently increase the surface area to be deposited on.

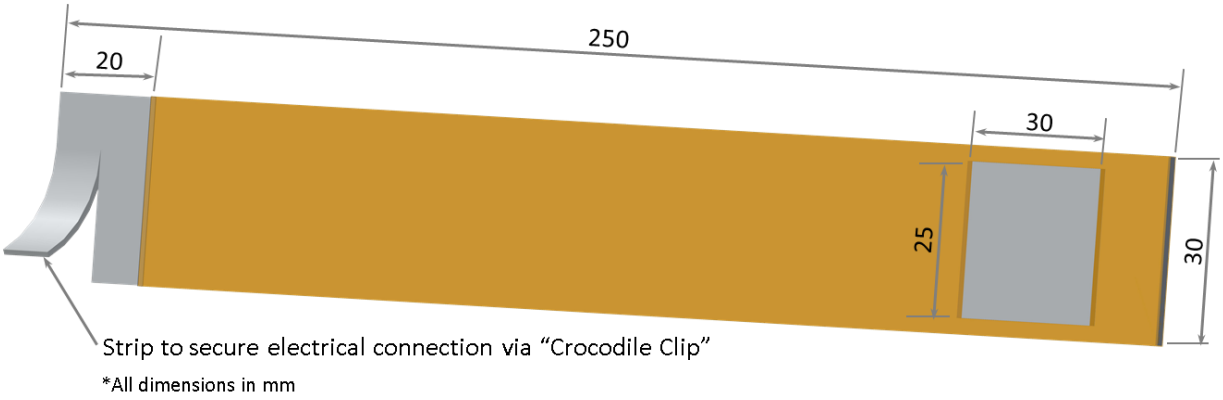

Figure 7: Dimensions of the Cathode.

In each case, the Anode was a strip of soluble Nickel activated using Sulfamic acid (H_3NSO_3) prior to each session of plating.

2.2.2 Nanoporous Alumina Templates for Nano-Wires

Nanoporous alumina membranes with hexagonal ordering and controlled geometrical characteristics were prepared by anodic oxidation in a dual step process [83] from aluminum sheet of high purity (99.99%).

1. Oxidation was carried out in 0.3 M oxalic solution, using a cell maintained at 20°C by a HAAKE K10 cryostat, with vigorous stirring and Ti as cathode.
2. Aluminum oxidation was performed under a constant voltage of 40 V for 120 min both for first and second step.
3. Between the two, oxide dissolution was performed in a 0.2M CrO_3 + 0.4M H_3PO_4 solution at 60 °C for 30 min.
4. Templates with 50 nm pore diameter were obtained.
5. For the subsequent electrodeposition, a thin (30 nm) Au PVD coating on the bottom membrane side was used to guarantee electrical contact.

2.3 Preparation of Samples

2.3.1 Types of Cells Used

2.3.1.1 Vertical Electrode Configuration with Mechanical Stirrer

This is the most basic configuration of an electrochemical cell. The exposed rectangular area of the INOX Cathode is placed parallel and facing the soluble-Nickel Anode. The mechanical Stirrer ensures that nanopowder remains dispersed in the electrolyte through the process of electroforming. This cell was used to carry out the first stage of study using NiCo electrolyte without any suspended particles. The mechanical stirrer was used to circulate the electrolyte effectively around the electrodes and distribute the heat to the entire volume of the electrolyte.

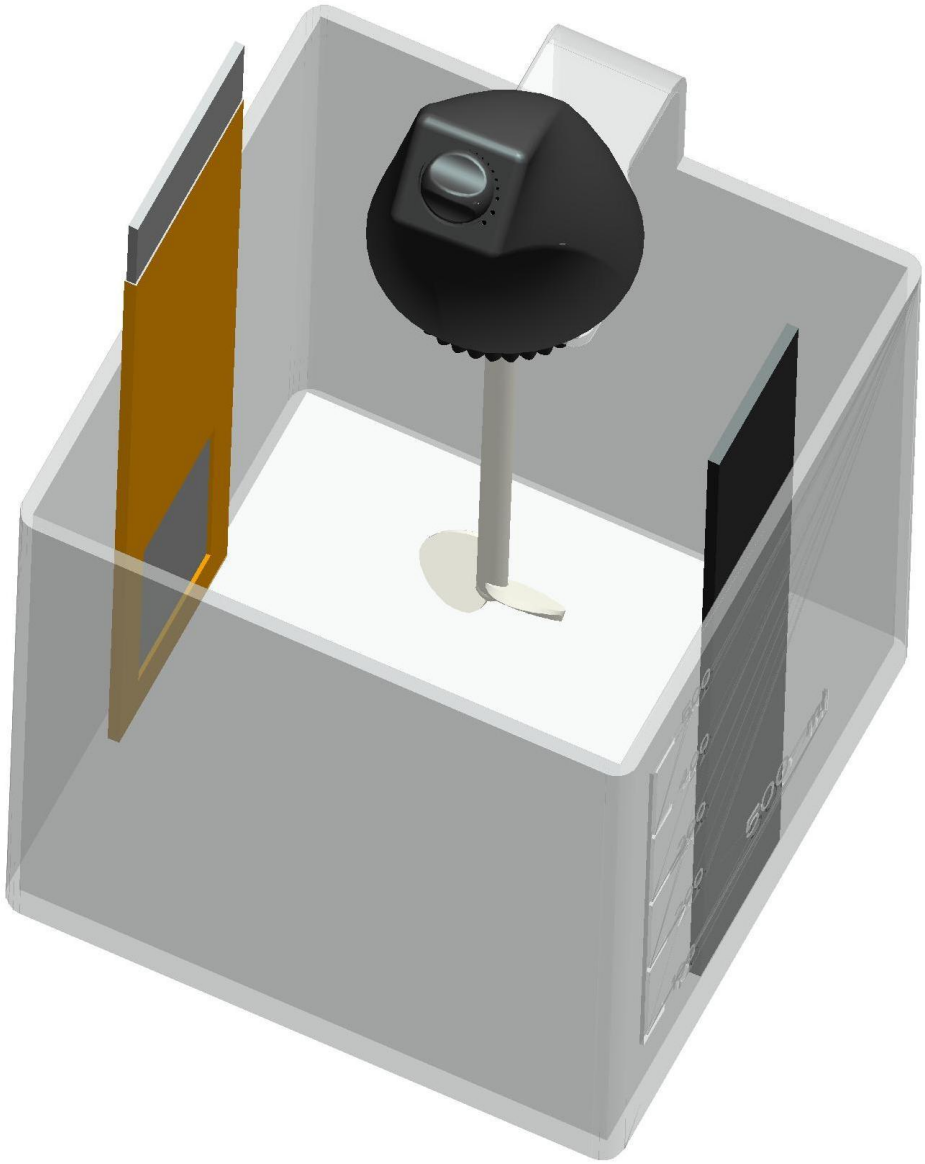

Figure 8: Illustration of the simple cell with vertically-parallel electrodes.

2.3.1.2 Horizontal Electrode Configuration with Mechanical Stirrer

This configuration of the cell is intended to favour the incorporation of the Ferrite particles into the NiCo Matrix. Here, as illustrated in the figures below, the electrodes are parallel and still face each other but the area to be deposited and a part of the Anode are twisted by 90° to allow ferrite particles more time to be incorporated in the NiCo matrix.

The two electrodes were not placed directly over each other and at an angle so as to allow Hydrogen bubbles to escape without impacting the surface area of either electrodes.

This setup may also be said to be “Gravity-Assisted”. The mechanical stirrer was used to circulate the electrolyte effectively around the electrodes, distribute the heat to the entire volume of the electrolyte and to keep the Nanoparticles suspended in the solution.

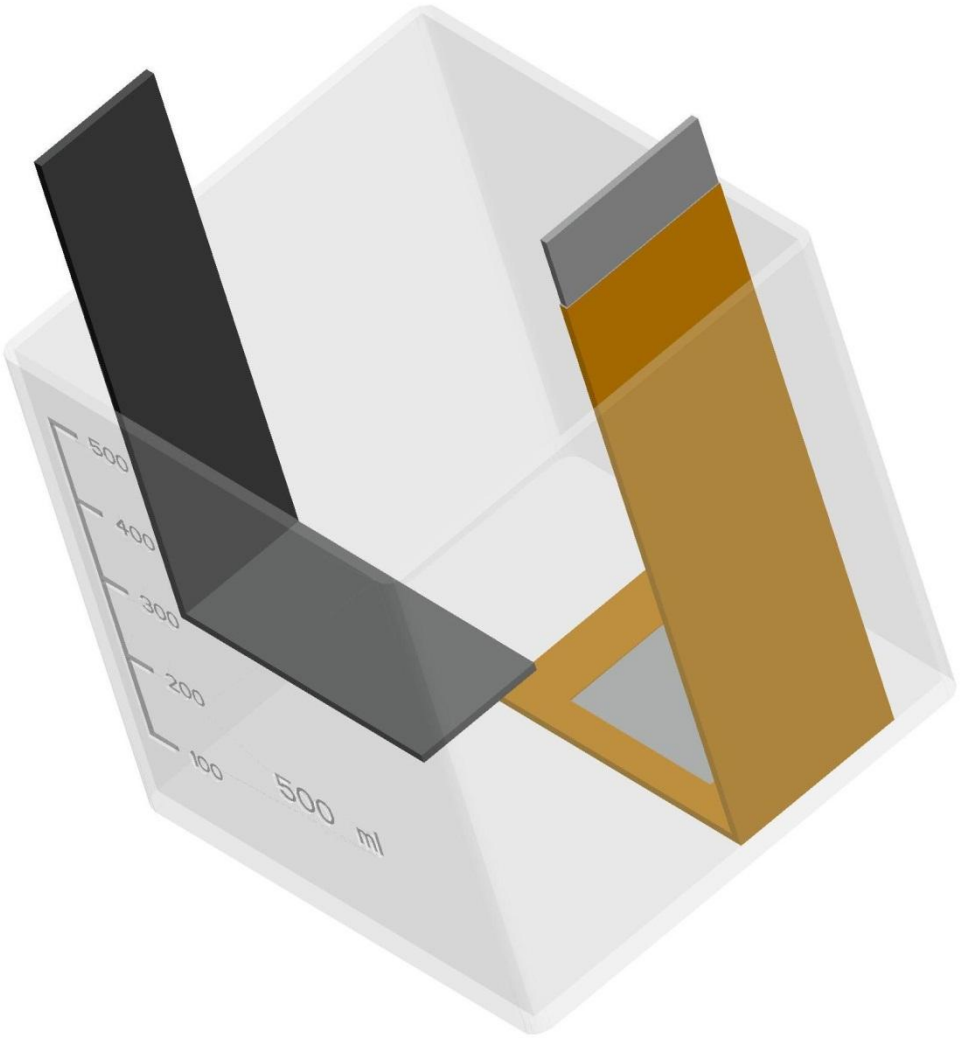

Figure 9: Illustration of the simple cell with horizontal-parallel electrodes.

2.3.1.3 Forced-Flow onto Horizontal Electrode

This type of Electrochemical cell was designed with the intension of studying the incorporation of kinetically-energized ferrite particles in NiCo matrix.

Here, a miniature pump is used to force the electrolyte along with the dispersed Ferrite particles through multiple nozzles onto the Cathode which is kept in a vertical arrangement.

The soluble-Nickel Anode is placed parallel to it. The mechanical stirrer was used to circulate the electrolyte effectively around the electrodes, distribute the heat to the entire volume of the electrolyte and to keep the Nanoparticles suspended in the solution..

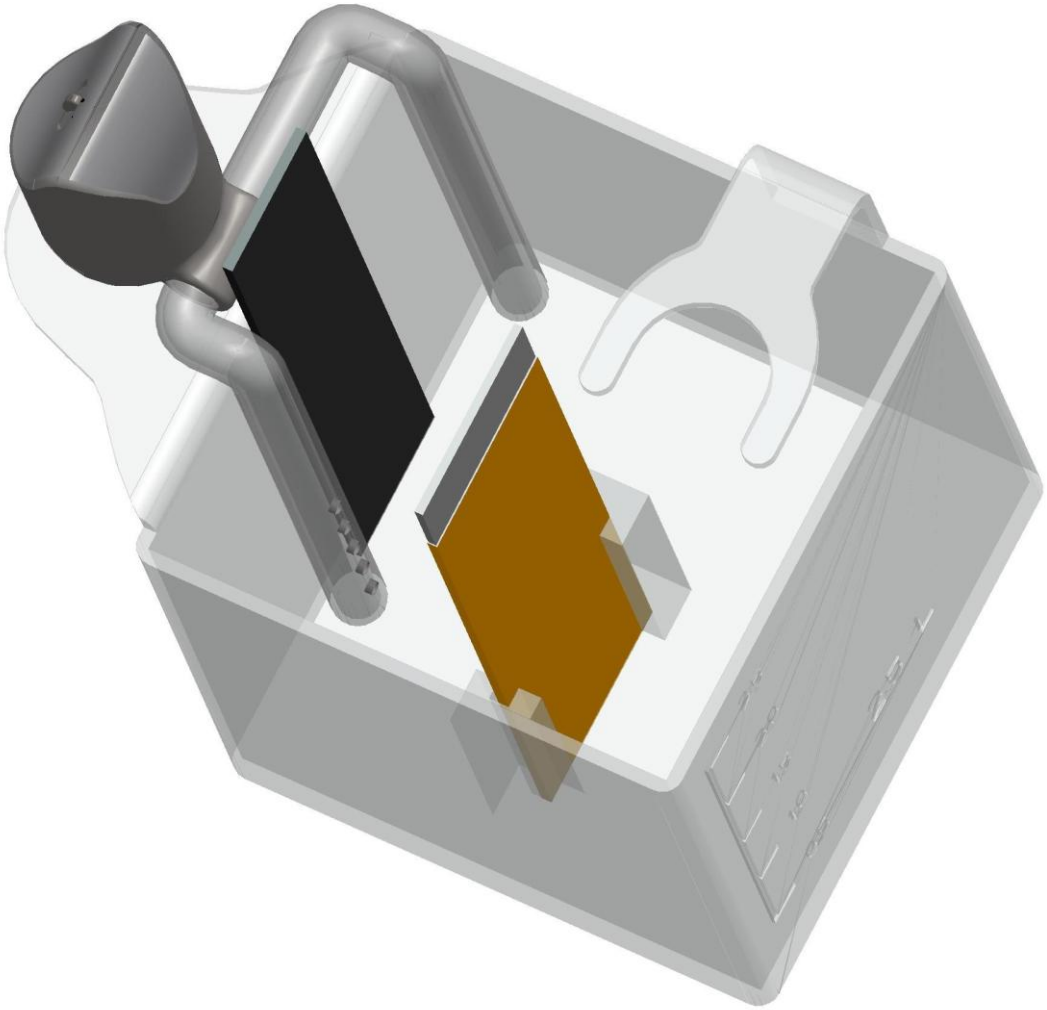

Figure 10: Cell with forced flow configuration.

2.3.1.4 Centrifugal Electrochemical Cell

This was a prototype cell conceived, designed, fabricated and tested at the SuperLab at Politecnico di Milano. This cell was designed with the intention of optimizing the deposition process in a manner so as to reduce the quantity of the substantially expensive $Fe_{12}O_{19}Ba_{0.2}Sr_{0.8}$ nanopowder by Sigma-Aldrich.

The initial design of this cell was that of a simple cylinder:

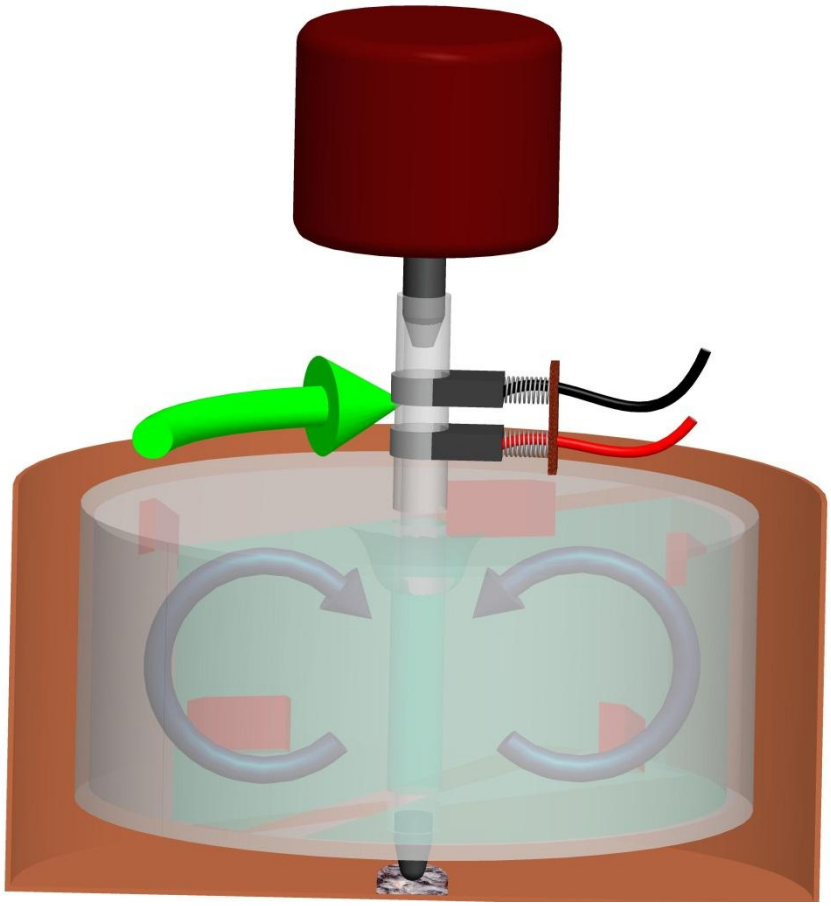

Figure 11: Intended flow of electrolyte within the centrifugal cell.

This design was modified to allow the dispersed particles to aggregate in the region of the electrodes, particularly the Cathode.

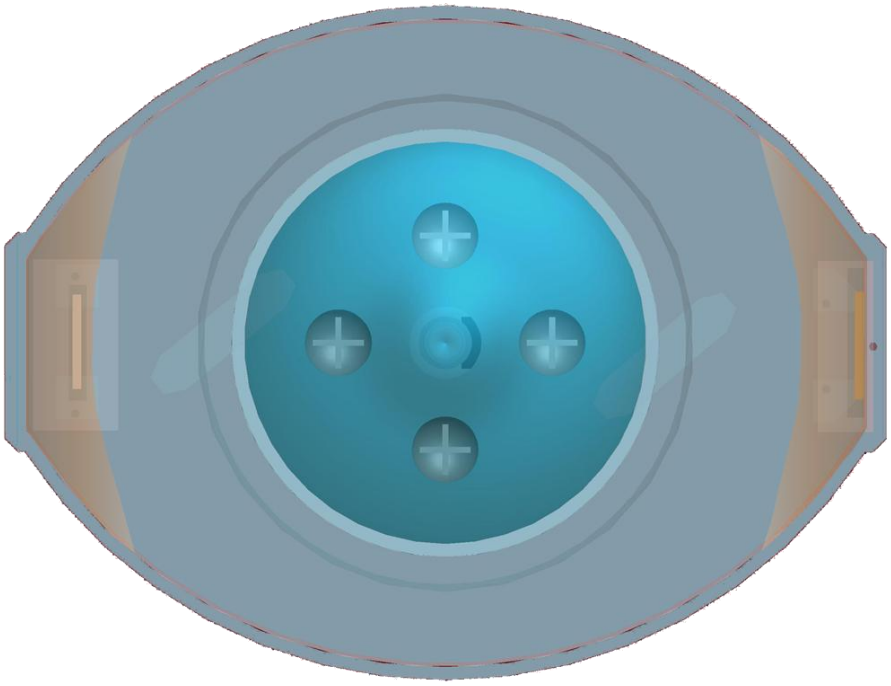

Figure 12: Region of the cell where a higher Nanoparticle concentration desired than the rest of the centrifugal cell.

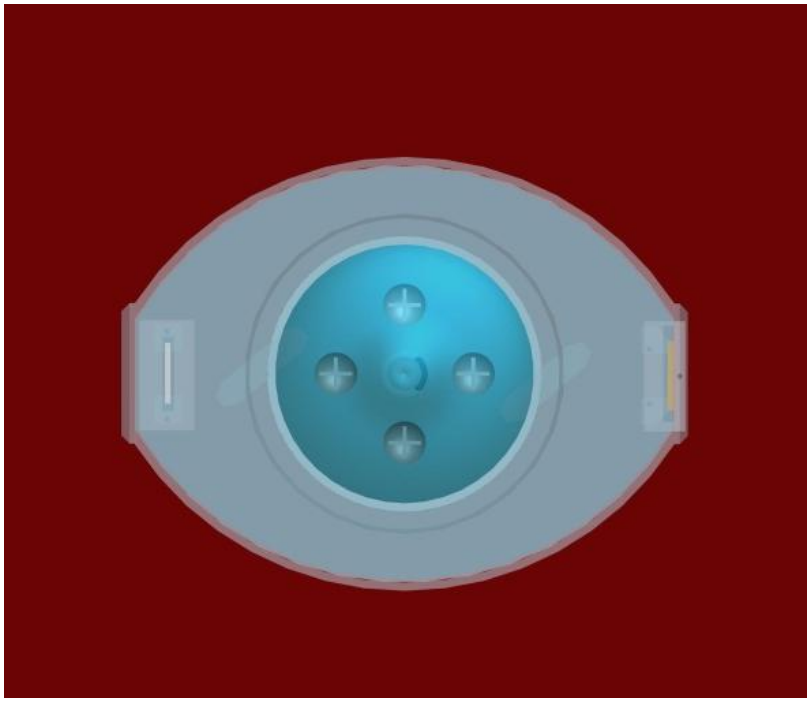

Figure 13: Top view of the Centrifugal Cell.

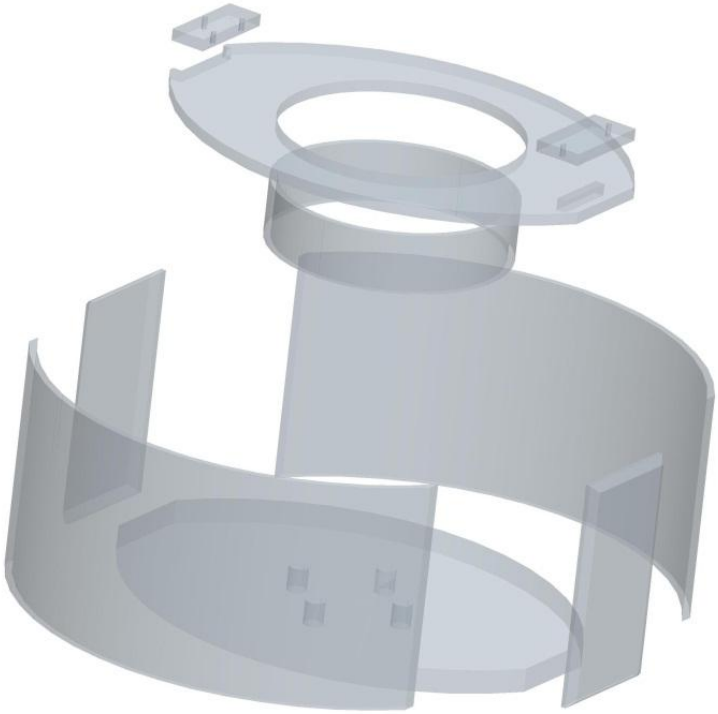

Figure 14: Exploded view of the Centrifugal Cell.

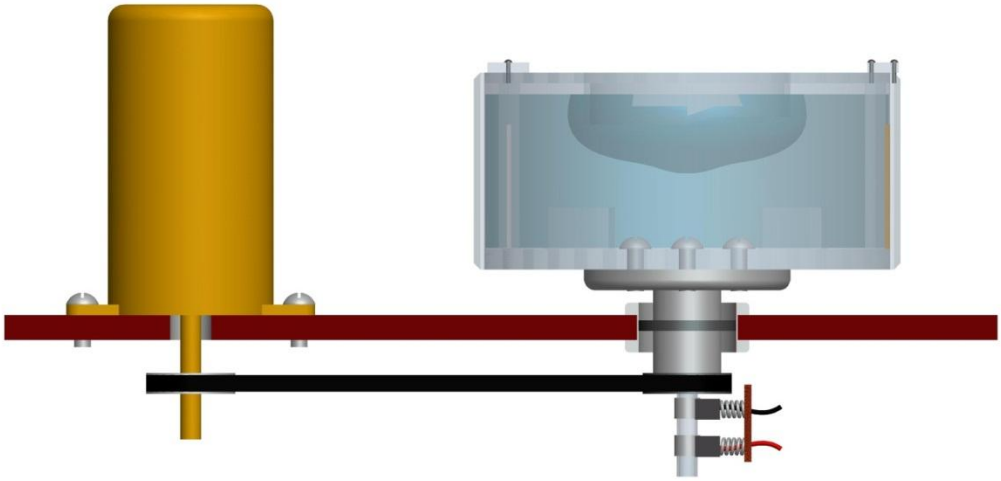

Figure 15: Side Sectioned view of the Centrifugal cell with motor assembly.

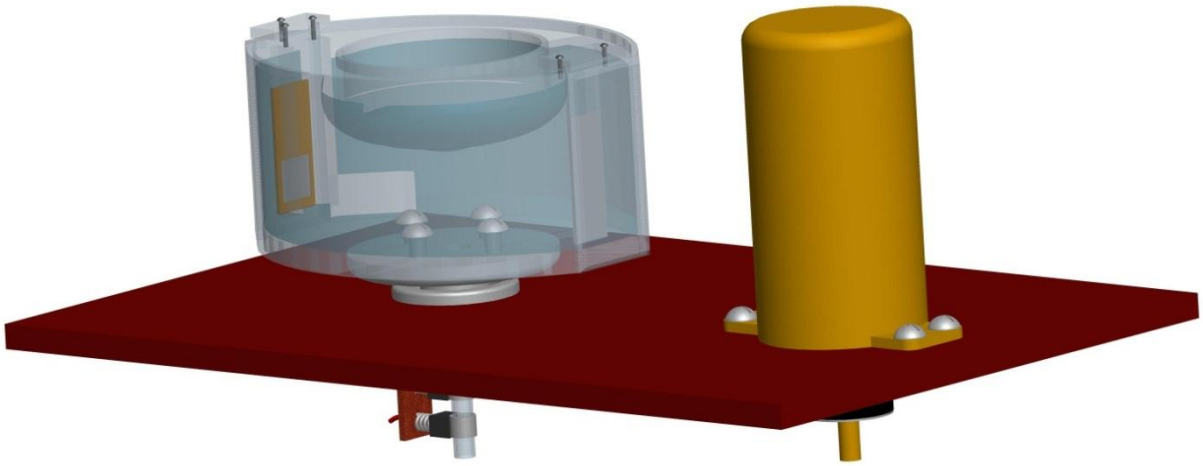

Figure 16: Isometric view of the complete Centrifugal Cell assembly.

The system uses a portable Candle heater which can be inserted into the liquid through the opening on top. The Anode and the Cathode may be placed through the slots on the upper lid. Sufficient opening was ensured for the feedback thermometer and a mechanical stirrer.

The final design was slightly altered during fabrication so as to allow use of the available resources and optimize time:

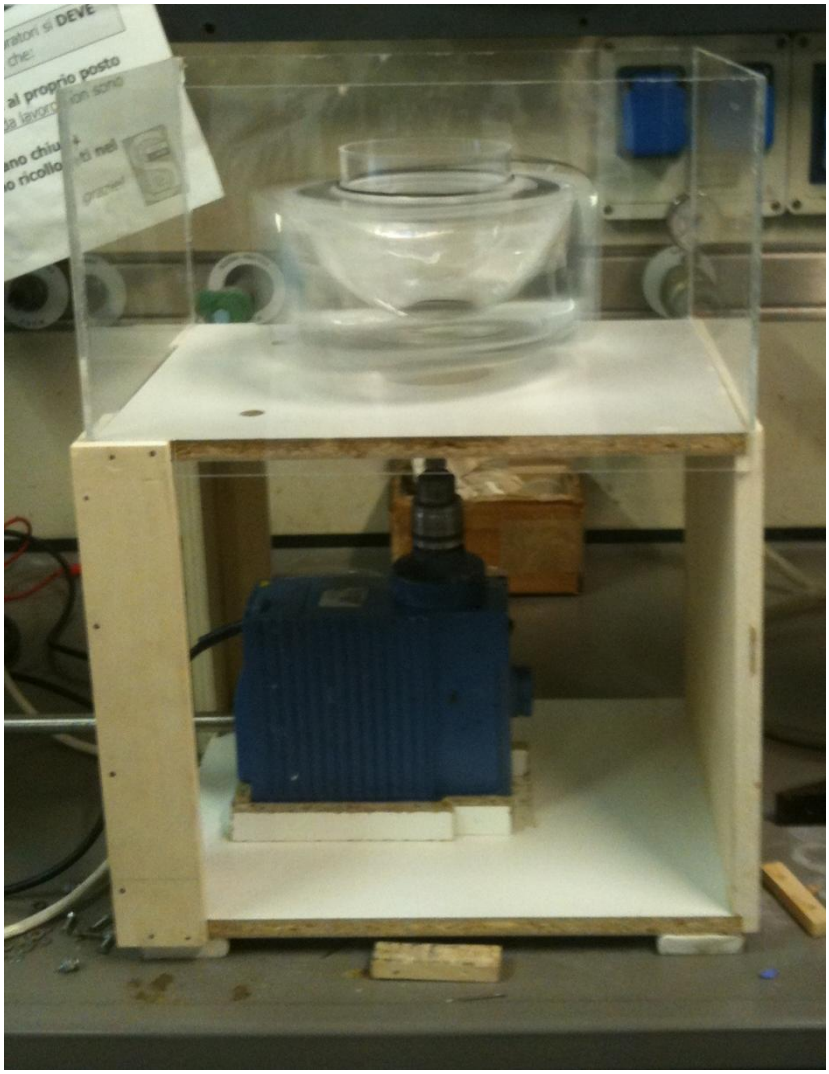

Figure 17: Final design of the constructed Centrifugal cell.

2.3.2 AAO Template Holder

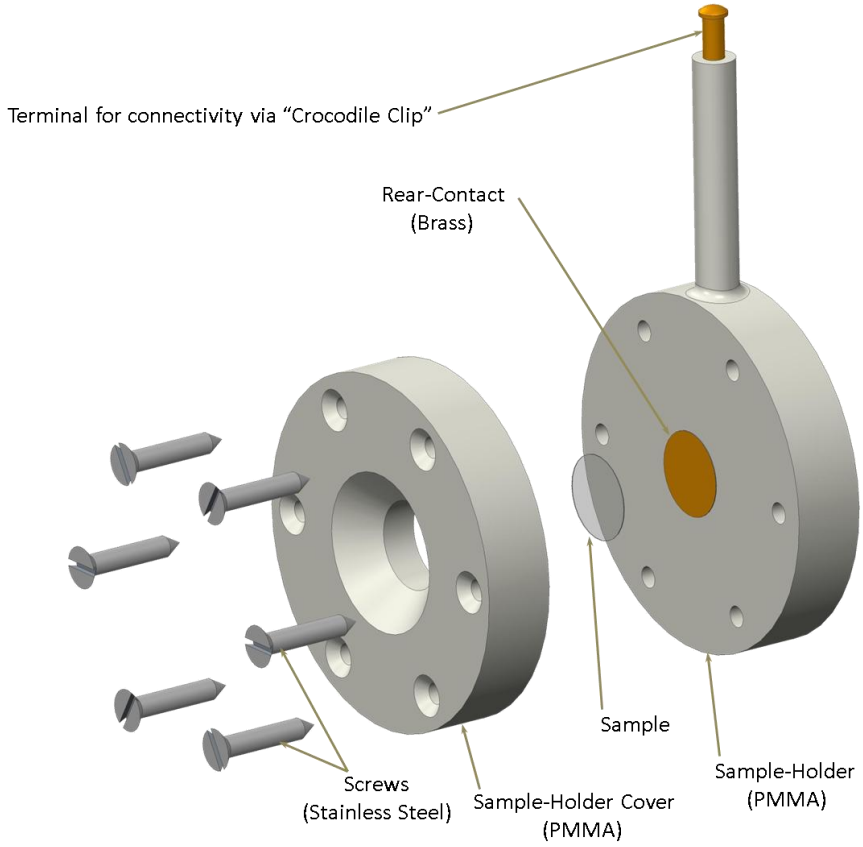

Figure 18: AAO Template holder design.

As depicted in the illustration above, the sample was place with great care between the two halves of the Sample-holder. Additionally, a polymer gasket was used to prevent electrolyte from seeping in from unintended directions. The electrochemical deposition initiates from the rear brass contact. Additionally, Kapton was used to seal the screws and the polymer gasket to avoid any leakage of current.

2.3.3 Electroforming of Composite NiCo Films

The depositions were carried out in the various cells using the previously prepared electrolyte.

A current density of 10 mA/cm^2 (75 mA in total) was applied for in various concentrations of Ferrite particles by using an EG&G Princeton Applied Research, Model 273A, equipment. The reference electrode chosen was Calomel Electrode.

The Kapton tape was changed between each deposition after the Cathode was cleaned using deionized water.

In each case, between any two electrodepositions, the electrolyte was analyzed and concentrations of Ni and Co were adjusted using their respective sulfamates using the formula:

$$C_1V_1 = C_2V_2$$

Where,

C_1 = Concentration of Original Solution

C_2 = Concentration required in Final Electrolyte

V_1 = Volume of Original Solution required

V_2 = Volume of Final Electrolyte

The pH of the bath was readjusted to 4 before each deposition.

2.3.4 Electrochemical Deposition of Composite NiCo Nanowires

The moderate particle concentration of 1g/l was chosen to avoid obstruction of pores.

The cell was a beaker filled with 200 ml of the plating bath, mechanically stirred at 200 rpm. The reference electrode was Ag/AgCl and the anode was soluble nickel activated with H3NSO3. A current density of 10 mA/cm^2 was applied for 1 h to electrodeposit the nanowires by using an EG&G Princeton Applied Research, Model 273A, equipment. The stability of the nanoparticles in the bath was thus proved: identical magnetic response and XRD profile of the barium ferrite nanoparticles were obtained before and after immersion of the particles in the electrolytic bath during several days.

2.4 Characterization Techniques Used

2.4.1 XRD:

X-rays are electromagnetic radiation with typical photon energies in the range of 100 eV - 100 keV. For diffraction applications, only short wavelength x-rays (hard x-rays) in the range of a few angstroms to 0.1 angstrom (1 keV - 120 keV) are used. Because the wavelength of x-rays is comparable to the size of atoms, they are ideally suited for probing the structural arrangement of atoms and molecules in a wide range of materials. The energetic x-rays can penetrate deep into the materials and provide information about the bulk structure.

X-rays are produced generally by either x-ray tubes or synchrotron radiation. In a x-ray tube, which is the primary x-ray source used in laboratory x-ray instruments, x-rays are generated when a focused electron beam accelerated across a high voltage field bombards a stationary or rotating solid target.

X-rays primarily interact with electrons in atoms. When x-ray photons collide with electrons, some photons from the incident beam will be deflected away from the direction where they originally travel, much like billiard balls bouncing off one another. If the wavelength of these scattered x-rays did not change (meaning that x-ray photons did not lose any energy), the process is called elastic scattering (Thompson Scattering) in that only momentum has been transferred in the scattering process. These are the x-rays that we measure in diffraction experiments, as the scattered x-rays carry information about the electron distribution in materials. On the other hand, in the inelastic scattering process (Compton Scattering), x-rays transfer some of their energy to the electrons and the scattered x-rays will have different wavelength than the incident x-rays.

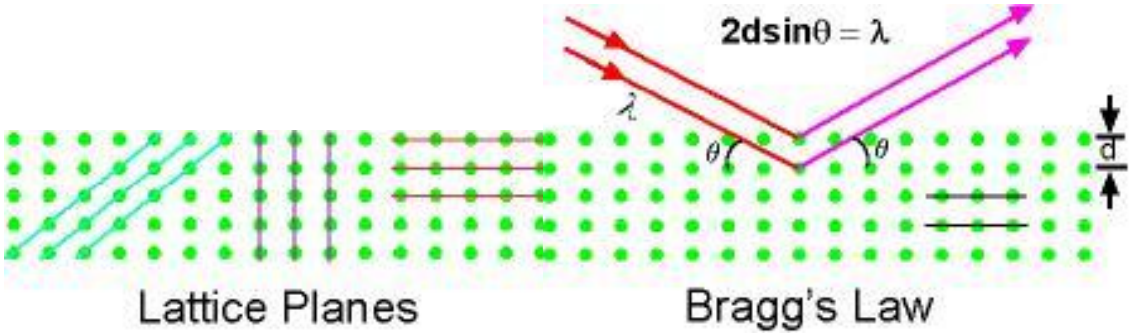

Figure 19: Illustration of XRD principle.

$$2d.Sin\Theta = \lambda \quad (\text{Bragg's law})$$

This is known as the Bragg's law, after W.L. Bragg, who first proposed it. In the equation λ is the wavelength of the x-ray, q the scattering angle, and n is an integer representing the order of the diffraction peak. The Bragg's Law is one of most important laws used for interpreting x-ray diffraction data.

It is important to point out that although we have used atoms as scattering points in this example, Bragg's Law applies to scattering centres consisting of any periodic distribution of electron density. In other words, the law holds true if the atoms are replaced by molecules or collections of molecules, such as colloids, polymers, proteins and virus particles.

2.4.2 Cyclic voltammetry analysis:

Potentiodynamic electrochemical measurement in a cyclic voltammetry experiment the working electrode potential is ramped linearly versus time like linear sweep voltammetry. Cyclic voltammetry takes the experiment a step further than linear sweep voltammetry which ends when it reaches a set potential. When cyclic voltammetry reaches a set potential, the working electrode's potential ramp is inverted. This inversion can happen multiple times during a single experiment. The current at the working electrode is plotted

versus the applied voltage to give the cyclic voltammogram trace. Cyclic voltammetry is generally used to study the electrochemical properties of an analyte in solution.

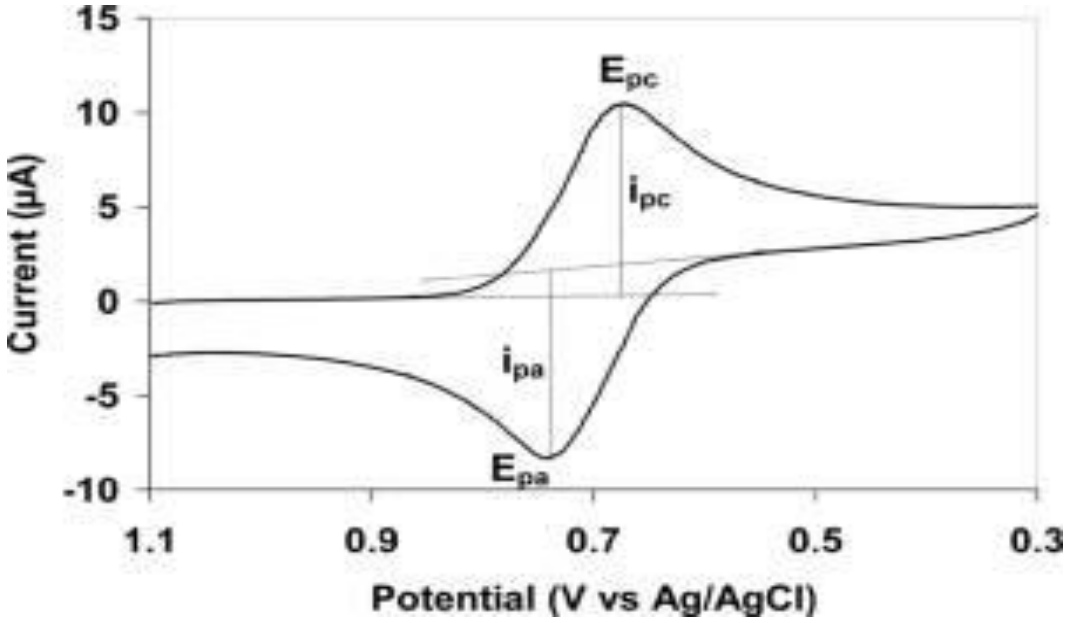

Figure 20: Typical cyclic voltammogram where i_{pc} and i_{pa} show the peak cathodic and anodic current respectively for a reversible reaction.

All the samples we prepared have been evaluated in KOH solution of 6M we prepared before. We covered all the samples with Kapton except for the area to be reacted with the solution W=2cm, and L=2cm. we used the potentiometer of the type potentistat/ galvanostat Model 273 A, EG& G, Princeton Applied research, the counter electrode was a pure platinum mesh , an Ag/AgCl reference electrode and the working electrode was the Nickel samples : the pure Nickel , the oxidized sample by the furnace + air with 200°C treatment, the Nickel electro oxidized from the $Na_2B_4O_7$ 0.100* 10^$^{-2}$ M solution, the Nickel electro oxidized from 0.5M $NiCl_2$ (97%) + 0.1 M KCl+ EDTA (99%) solution, and the membrane deposited with Nickel the thinner side of our deposition which has been electro oxidized through $Na_2B_4O_7$ 0.100 x 10^{-2} M solution. We used the magnetic stirrer of 250 rpm velocity for homogenization conditions, and we kept parallel electrodes for equal current density distribution. For setting up the system we fixed our parameters of (-0.4) - (-0.9) voltage as the initial and final potentials conditions, and we used for the step rate three

different speeds as: 30, 20, and 10 mV/s. All the experiments have been done in the room temperature conditions of 25°C.

2.4.3 SEM (Scanning Electronic Microscope):

The scanning electronic microscope is a type of electron microscope that images the sample surface by scanning it with a high-energy beam of electrons in a raster scan pattern. The electrons interact with the atoms that make up the sample producing signals that contain information about the sample's surface topography, composition and other properties such as electrical conductivity.

The types of signals produced by an SEM include secondary electrons, back-scattered electrons (BSE), characteristic X-rays, light (cathodoluminescence), specimen current and transmitted electrons. Secondary electron detectors are common in all SEMs, but it is rare that a single machine would have detectors for all possible signals. The signals result from interactions of the electron beam with atoms at or near the surface of the sample. In the most common or standard detection mode, secondary electron imaging or SEI, the SEM can produce very high-resolution images of a sample surface, revealing details about less than 1 to 5 nm in size. Due to the very narrow electron beam, SEM micrographs have a large depth of field yielding a characteristic three-dimensional appearance useful for understanding the surface structure of a sample.

The SEM instrument we used was of the type EVO 50 of ZEISS.

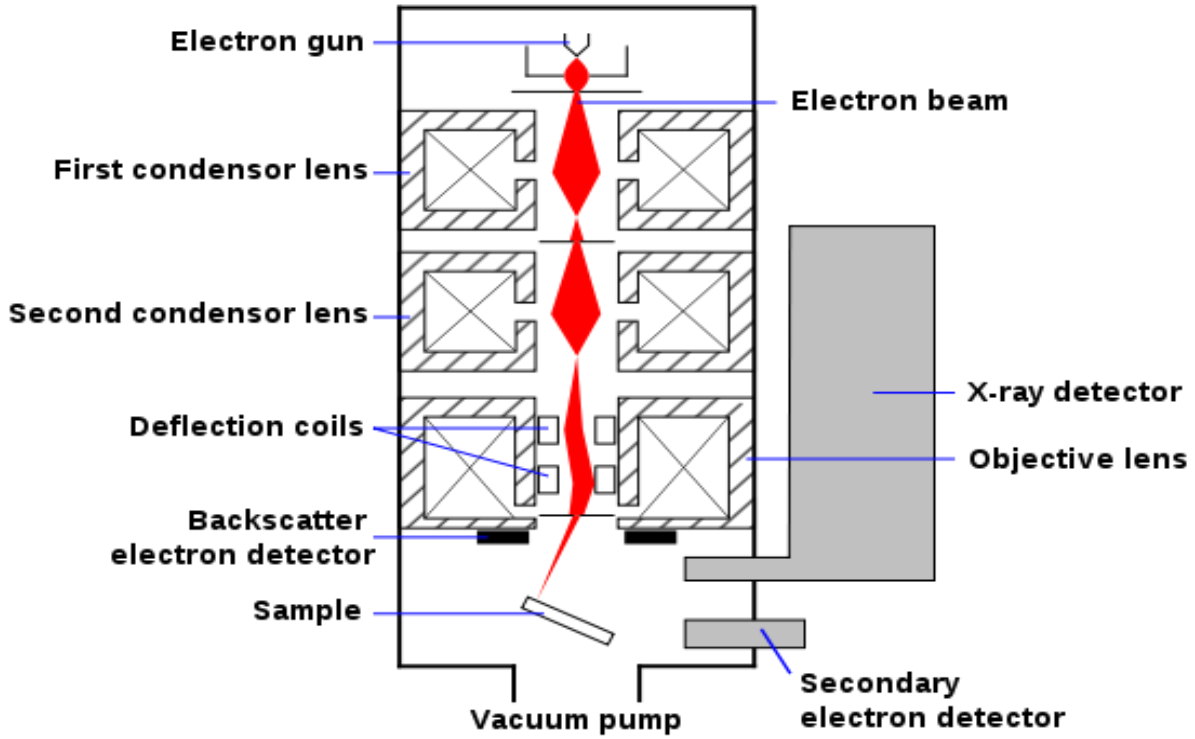

Figure 21: Schematic Diagram of SEM.

2.4.4 Microidentation test:

The hardness of a material is normally defined as the resistance which it opposes penetration by another body, assuming that the latter does not undergo deformation during penetration.

For thin layers the method is usually used Vickers, in which the indenter is a diamond pyramid with a square base with a top angle of 136°.

An alternative method, used mainly in the USA, the Koop test, in which the tip is always a diamond, but diamond shaped, with a ratio between the diagonal 1/7, it is particularly suitable for testing adhesion on carry-examined section.

To obtain valid results, we must pay attention to certain parameters that must always be respected; first and foremost, the relative depth of penetration depending on the thickness of the film to be analyzed, that depth should not exceed a value of 1/8 thickness. Penetration top has a significant influence of the substrate, producing a hardness measurement error. It should also be considered that low values of applied load values behave as low penetration, where it becomes necessary to consider the deformation of the indenter. If this contribution is not properly estimated, the hardness may not accurately measure, is considered acceptable average values of Vickers hardness in a series of measures on a sample showing a percentage change not more than 10%, with standard deviations given.

The instrument used is a micro indenter Fischer scope ® H100. The analysis of load-penetration curve tool is able to provide information on the Vickers hardness, the modulus $E/(1-\nu^2)$, the maximum penetration of the tip in the sample. The micro hardness is calculated as the ratio between the maximum load and the area of contact, estimated by the penetration and the shape of the indenter.

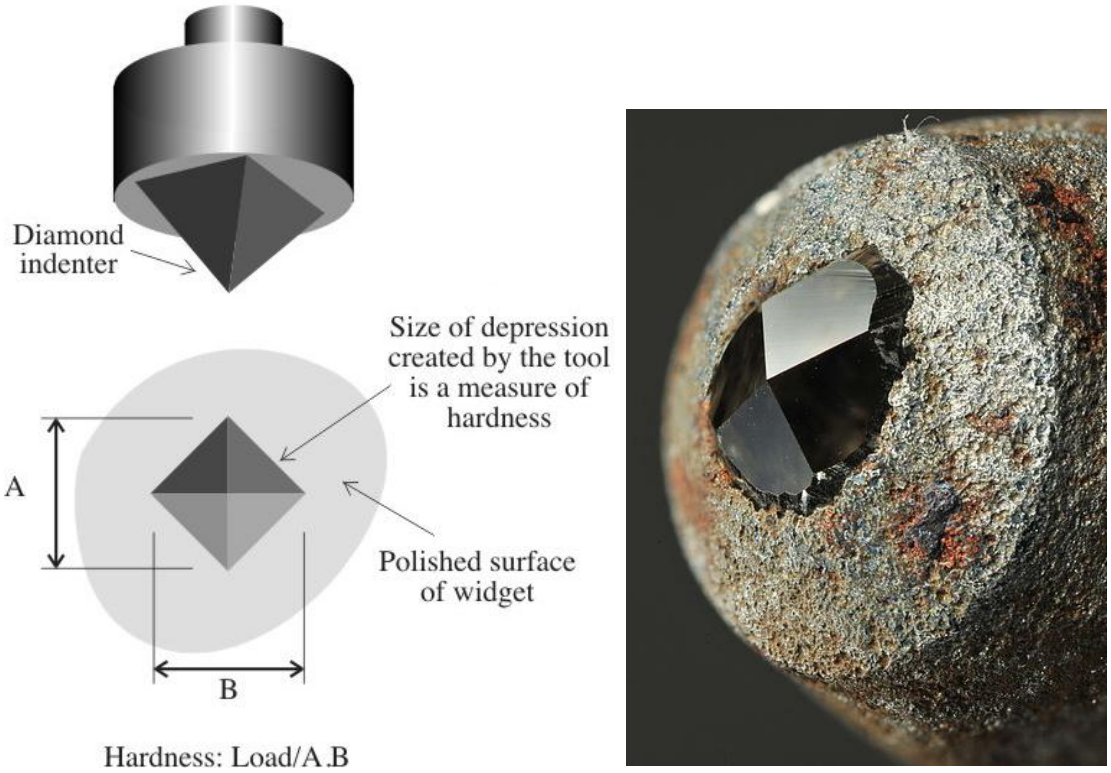

Figure 22: Vickers Pyramid Indenter.

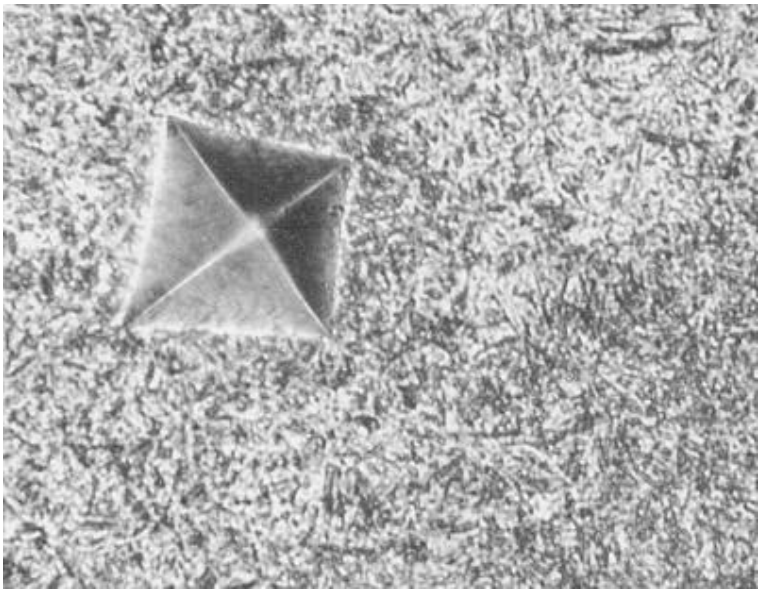

Figure 23: Indentation Impression after Vickers Hardness Test

Figure 24: Vickers Microidentation Instrument.

2.4.5 SQUID (Superconducting Quantum Interference Device)

Scanning SQUID microscopy is a technique where a superconducting quantum interference device (SQUID) is used to image surface magnetic field strength with micrometre scale resolution. A tiny SQUID is mounted onto a tip which is then rastered near the surface of the sample to be measured. As the SQUID is the most sensitive detector of magnetic fields available and can be constructed at submicrometre widths via lithography, the scanning SQUID microscope allows magnetic fields to be measured with unparalleled resolution and sensitivity.

2.4.6 VSM (Vibrating Sample Magnetometer)

A sample is placed inside a uniform magnetic field to magnetize the sample. The sample is then physically vibrated sinusoidally, typically through the use of a piezoelectric material. Commercial systems use linear actuators of some form and historically the development of these systems was done using modified audio speakers, though this approached was dropped due to the interference through the in-phase magnetic noise produced, as the magnetic flux through a nearby pickup coil varies sinusoidally. The induced voltage in the pickup coil is proportional to the sample's magnetic moment, but does not depend on the strength of the applied magnetic field. In a typical setup, the induced voltage is measured through the use of a lock-in amplifier using the piezoelectric signal as its reference signal. By measuring in the field of an external electromagnet, it is possible to obtain the hysteresis curve of a material.

Chapter 3: RESULTS AND DISCUSSION

3. Results and Discussion

3.1 Study of Plain NiCo films formed by Electrochemical Deposition

Films of NiCo were prepared from NiCo solution at different temperatures and current densities. Galvanostatic curves reveal the logical dependences of the stabilisation potential as a function of both current density and temperature (Figure 25). Stabilisation potentials were more negative by applying more negative current densities. At fixed current density (−10 mA cm−2) an increase in the temperature advanced the deposition potential.

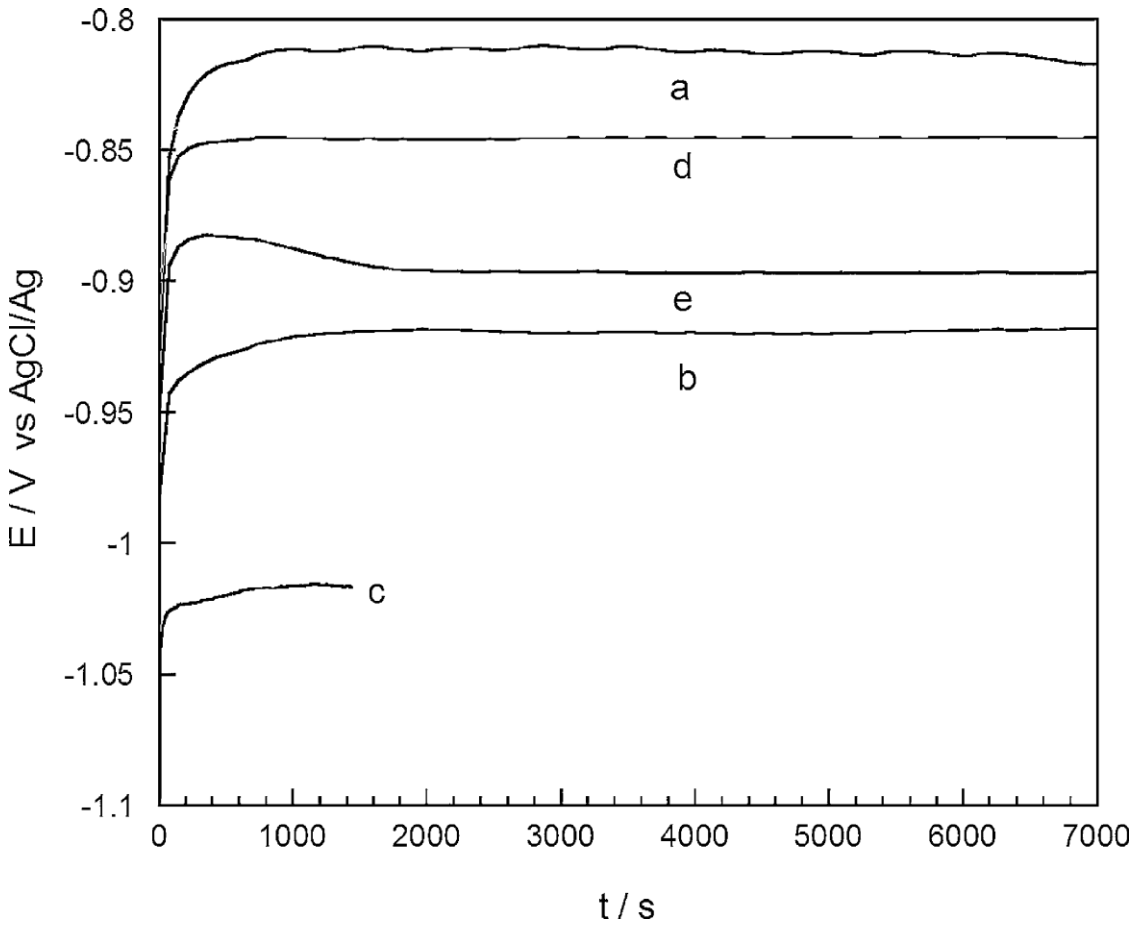

Figure 25: E–t transients of NiCo electrodeposition at different current densities: (a) j = −10 mA cm^{-2}, T = 50° C, (b) j = −30 mA cm^{-2}, T = 50° C, (c) j = −50 mA cm^{-2}, T = 50° C, (d) j = −10 mA cm^{-2}, T = 40° C, (e) j = −10 mA cm^{-2}, T = 30° C.

Anomalous NiCo deposition was observed for all conditions tested (Table 5) as is usual in the NiCo system from different electrolytic baths used [84, 85]. At fixed current density a low decrease of the cobalt percentage was observed when temperature was increased. On the other hand, an increase of the current density favoured the decrease of the cobalt percentage. This behaviour corresponds to a nickel deposition process controlled by activation whereas cobalt deposition process can be controlled by mass transfer as in other media [86].

Current Density [mA cm^{-2}]	Temperature [C]	at.% Ni	at.% Co
−10	50	47.0	53.0
−30	50	54.2	45.8
−50	50	55.3	44.7
−10	40	44.2	55.8
−10	30	40.2	59.8

Table 5: Composition of NiCo electrodeposits as a function of the bath temperature and current density applied.

Few variations in the morphological, structural and mechanical properties of the NiCo deposits were observed for the different deposition conditions tested. Compact, no fragile and very fine- grained NiCo deposits were always obtained, which morphology was hardly detected from SEM observation (Figure 24).

XRD results agree with those obtained from SEM micrographs, wide peaks were detected being the calculated grain sizes using Debye–Scherrer equation around 13 nm. All NiCo deposits prepared showed diffraction peaks corresponding to an FCC structure (Figure 25). No differences were observed in the range of current densities and temperatures used. The position of the peaks of the FCC phase was shifted to lower e values than those

corresponding to pure nickel as a consequence of the incorporation of cobalt in the FCC crystalline lattice. The intermediate position of the peaks between those of cobalt FCC and nickel FCC reveal the formation of solid solution of both metals.

Determination of both HV hardness and Young's modulus was made acquiring measurements on the surface and on the cross section of the films detached. The results show that no significant variation was observed for the alloy deposits as a function of the applied current density. The obtained microhardness values ranged between 533–547 HV with standard deviation SD ≈ 20. In order to compare the mechanical properties of alloy and pure metals, the electrodeposition of both nickel and cobalt was performed from the sulphamate bath containing the corresponding metal in the same operating parameters. Microhardness of obtained NiCo alloy improved: microhardness values were higher than those corresponding to electrodeposited nickel (337 HV with SD ≈ 24) and electrodeposited cobalt (450 HV with SD ≈ 15).

When mechanical properties of the coatings prepared at different temperatures were analyzed, a gradual variation of the values was observed as a function of the deposition temperature. Figure 26 shows that when the deposition temperature decreases, both the micro hardness and Young's modulus decrease.

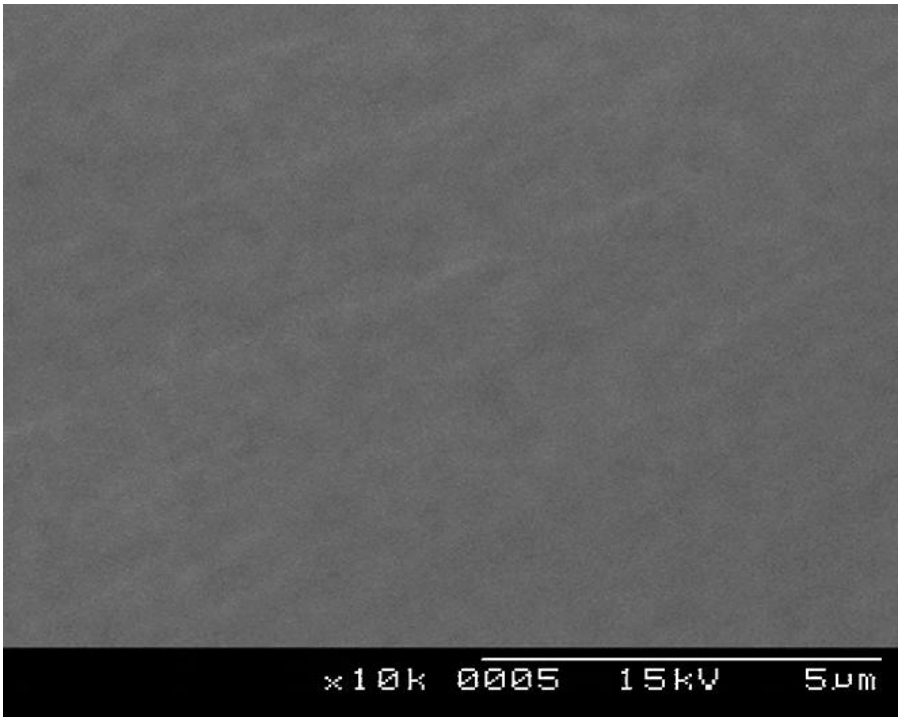

Figure 26: SEM picture of a NiCo deposit obtained at j = −10 mA cm^{-2} , T = 50 ° C.

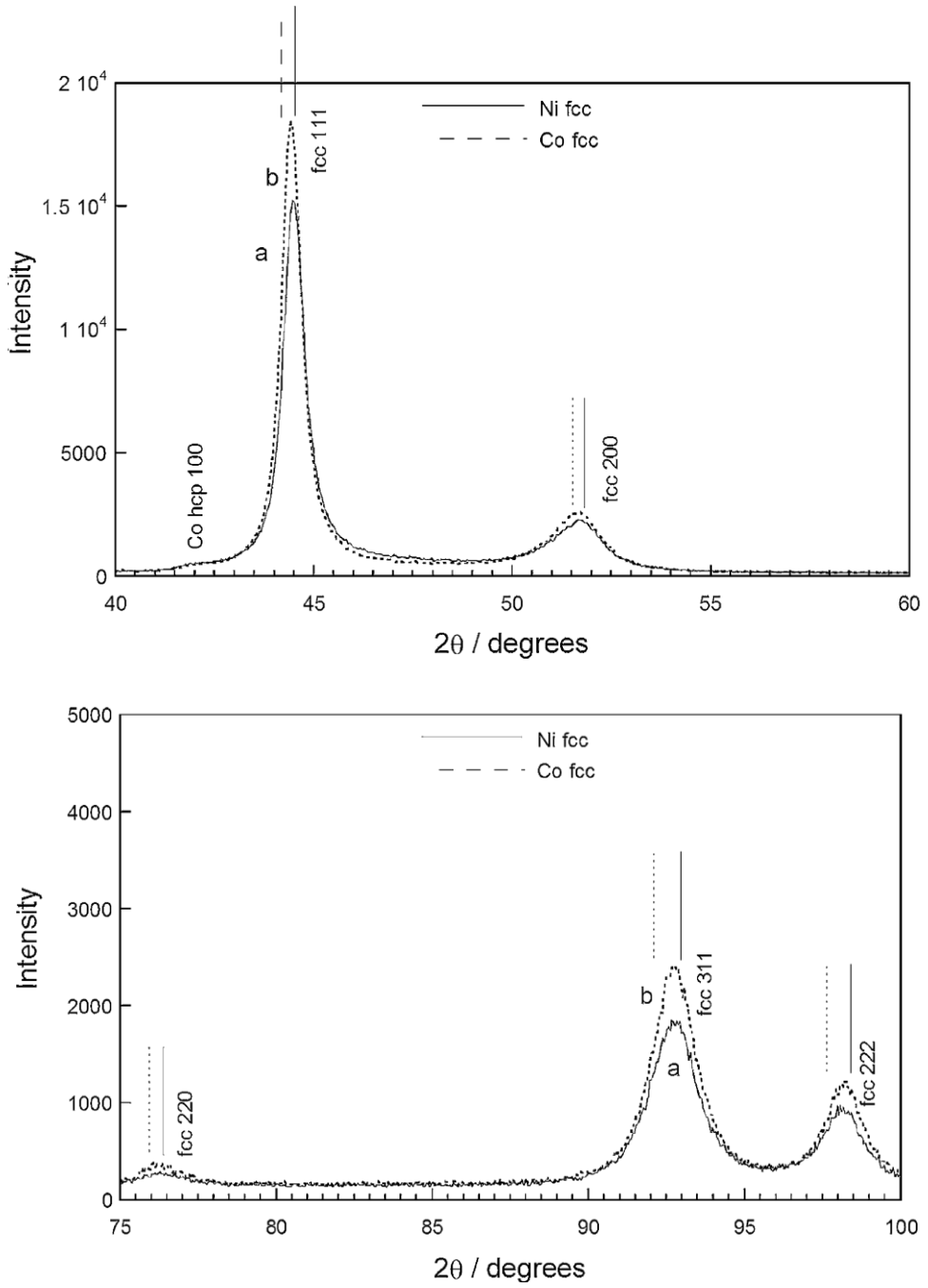

Figure 27: Two details of the X-ray diffractograms of NiCo deposits obtained at 50 ° C and: curve (a) j = −10 mA cm^{-2} ; curve (b) j = −50 mA cm^{-2} .

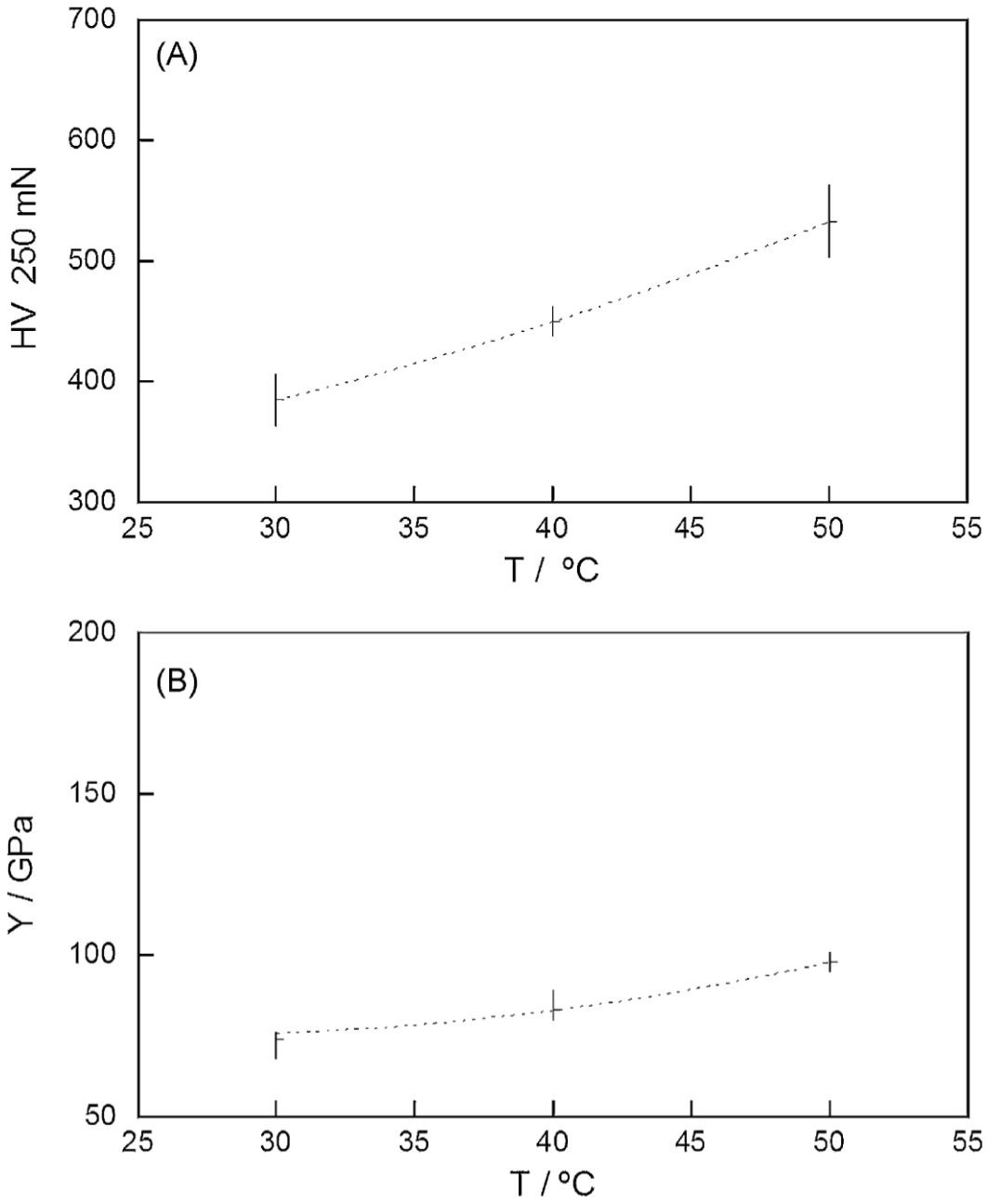

Figure 28: Dependence of the microhardness (A) and Young's modulus (B) with the temperature for NiCo deposits obtained at j = −10 mA cm^{-2}.

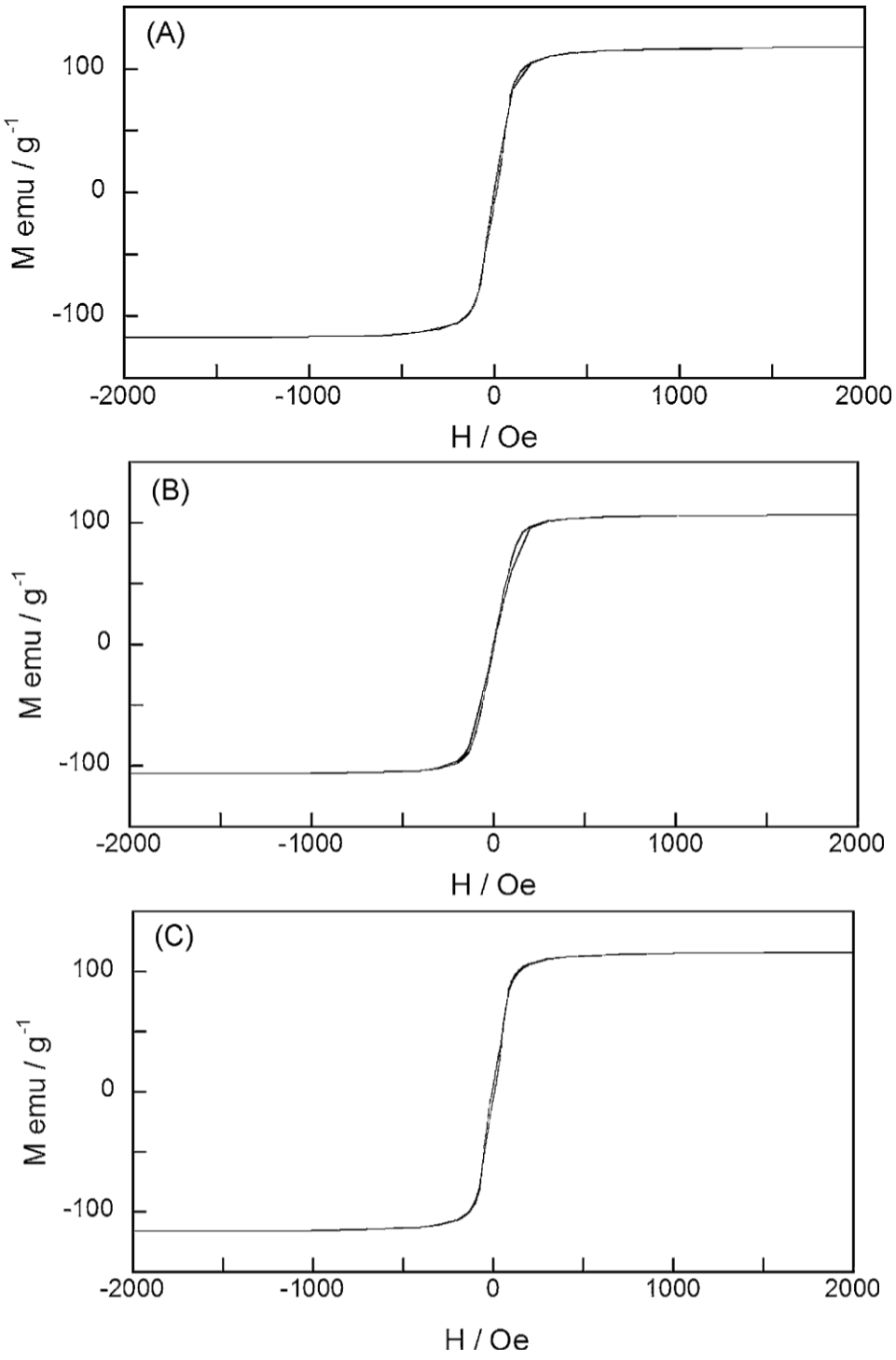

Figure 29: Magnetisation vs magnetic field applied for NiCo samples prepared at: (A) j = −10 mA cm−2 , T = 50 ° C, (B) j = −50 mA cm−2 , T = 50 ° C, (C) j = −10 mA cm−2 , T = 40 ° C.

The maximum hardness (up to 533 HV) and minimum elasticity (98 GPa) was observed for NiCo prepared at the higher temperature used.

In order to study the magnetic properties of alloy prepared, the magnetisation vs applied magnetic field curves were recorded. For all current densities and temperatures used, soft-magnetic properties of the films were detected (Figure 29). All deposits showed very low coercivity values lower than 10 Oe. The magnetisation of saturation value decreased (from 117 emu g^{-1} for deposits of 55 at.% Co to 107 emu g^{-1} for deposits with 45 at.% Co) as the cobalt content decreased due to the lower saturation magnetisation of pure electrodeposited nickel (52 emu g^{-1}) with respect to pure electrodeposited cobalt (150 emu g^{-1}).

3.2 Incorporation of Ferrite Nanoparticles into NiCo matrix using a Basic Electrochemical Cell

Electrochemical characteristics of the plating bath were obtained using data from the galvanostatic deposition experiment. The potential against the reference electrode (SCE) decreased linearly from − 0.8 V for the pure matrix deposition to − 0.95 V for 15 g/l $BaFe_{12}O_{19}$ particle bath loading as well as the current efficiency of the deposition, calculated by weight, from 90 to 65%. At still higher bath loadings the efficiency progressively decreased. This suggests an increase in the cathode polarization due to mass transfer limitations of the metallic ions at the electrode, with, as a consequence, a decrease of the cathodic efficiency.

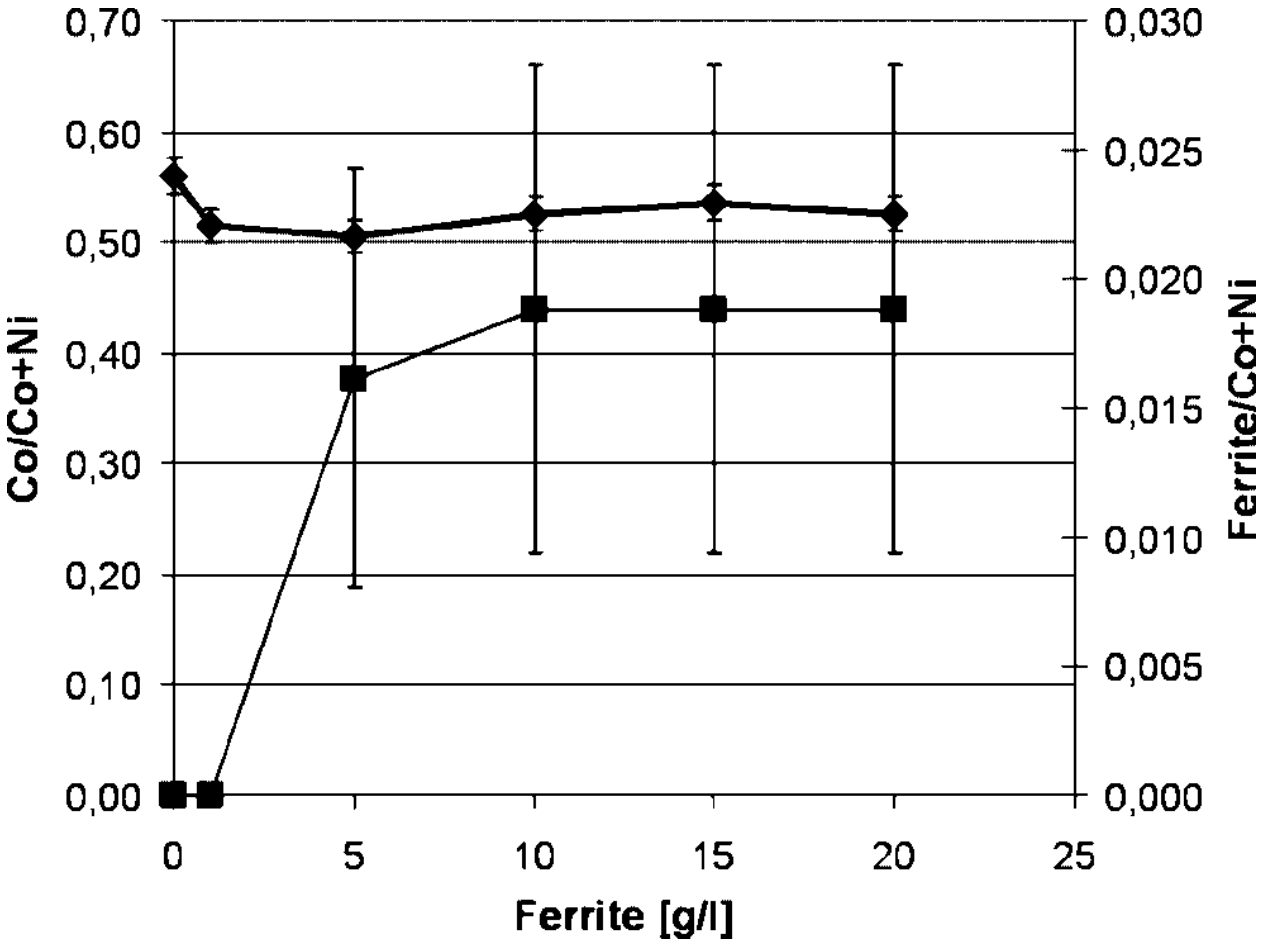

Figure 30: Chemical composition of the composites by EDS.

The composition of the samples was taken from EDS measurements on the cross-sections and is shown in Figure 30. The metallic matrix without particle incorporation has a composition of 56 at. % cobalt and 44 at. % nickel which is changed by co-deposition to an average composition of 51 at. % cobalt and 47 at. % nickel with the $BaFe_{12}O_{19}$ particle content as the difference of the sum 100 at. %. The $BaFe_{12}O_{19}$ particle incorporation has been estimated by measuring Fe concentration and by calculating the whole ratio of the particles in the composite assuming stoichiometric particle composition.

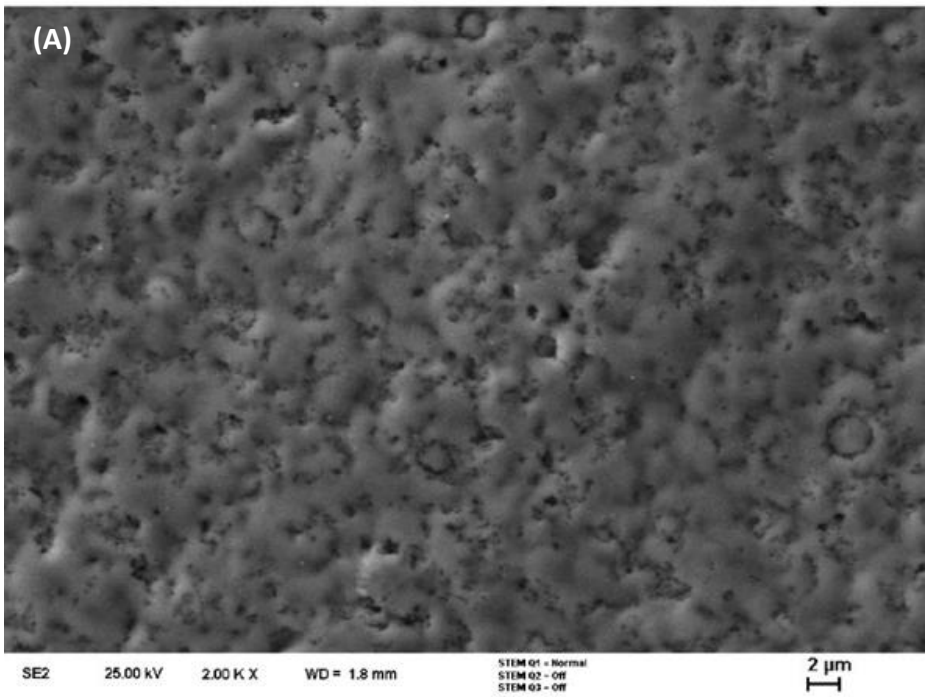

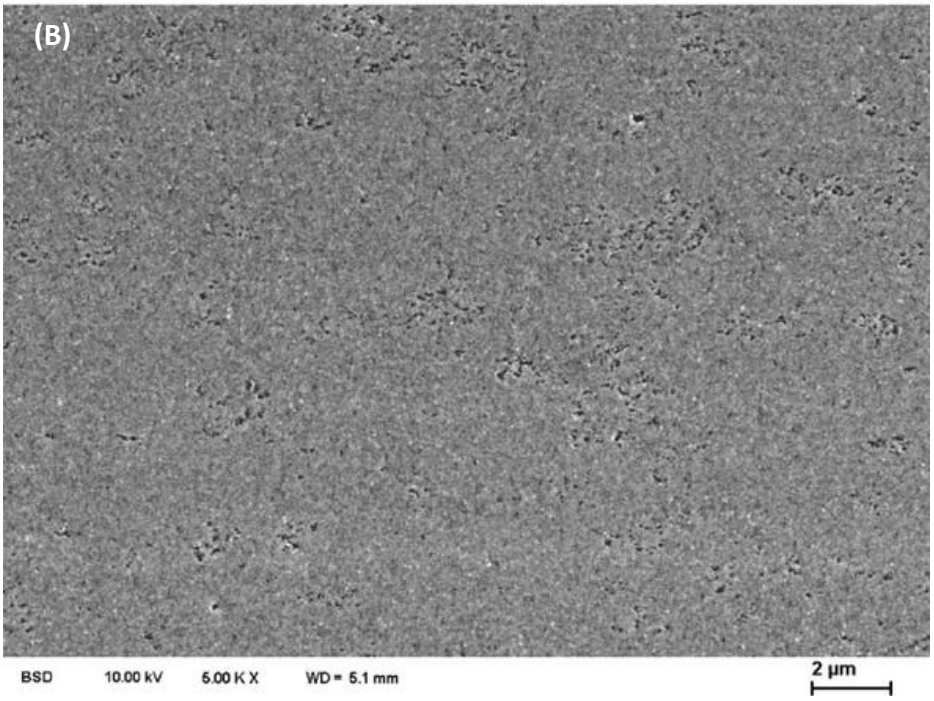

Figure 31: Typical composite in SEM imaging: (A) microstructure (5 g/l $BaFe_{12}O_{19}$), (B) surface topology (20 g/l $BaFe_{12}O_{19}$).

This has been done due to the barium concentration which is too small to be detected and due to the uncertainty of quantifying light elements by EDS. Nevertheless the uncertainty of the results is as high as shown in Figure 30 and for ferrite concentrations below 5 g/l in the electrolyte no particles could be detected.

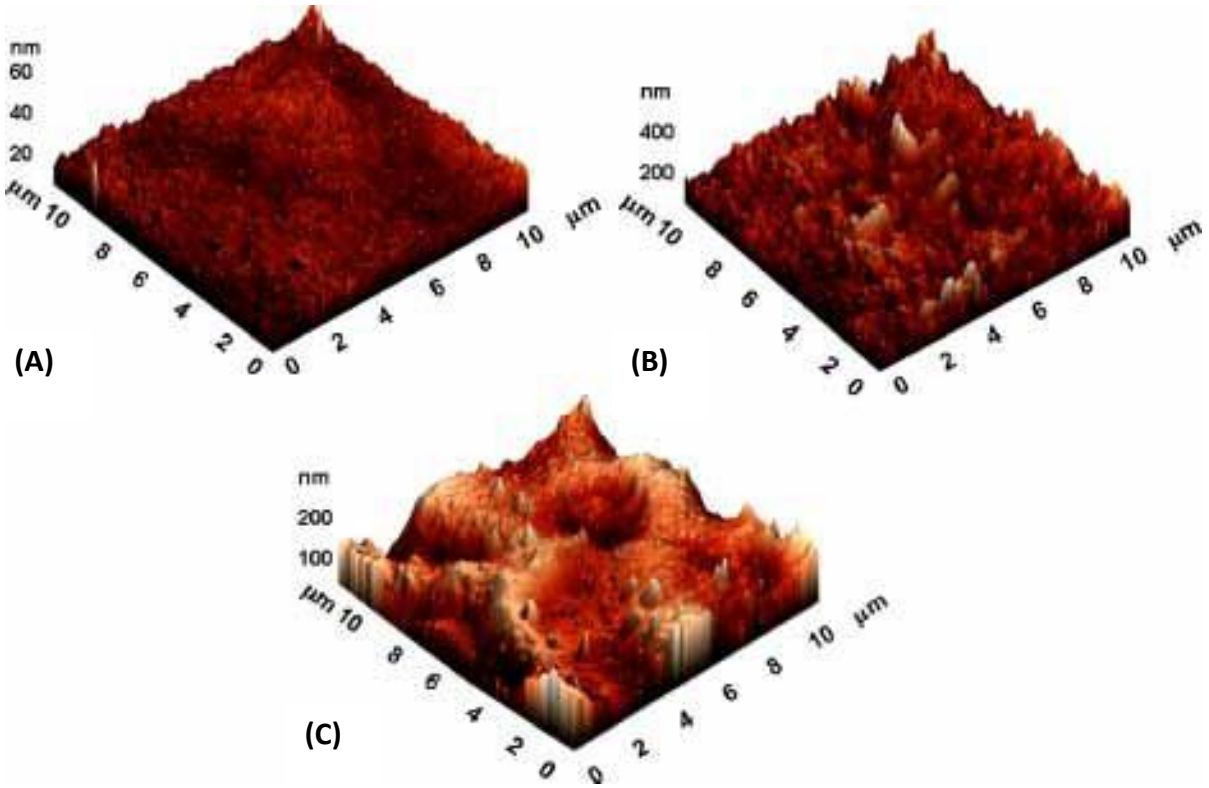

Figure 32: AFM surface morphology of composites: (A) 0 g/l – Ra = 3.9 nm, (B) 5 g/l – Ra = 23 nm, (C) 15 g/l – Ra = 30 nm.

For higher particle concentrations in the electrolyte, about 0.2 wt. % ferrite in the composite layer can be stated which seems not to differ up to 20 g/l bath loading. The equal particle concentration between 5 and 20 g/l bath load is confirmed by the appearance of cross-sections of the samples imaged by back-scattered electrons. Figure 31A shows the particle distribution in the composite with 5 g/l bath load which is typical for the higher bath loads as well. The metallic matrix appears fine-grained and the particles appear agglomerated. Additionally, the composite with 20 g/l particle bath load shows a striking columnar crystal growth at the surface of the metallic matrix which will be demonstrated and discussed later. A typical surface morphology of the composites is shown in Figure 31B. By AFM imaging of the surface roughness has been examined. A

steady rise of roughness estimated as the arithmetic average of the absolute values from 3.9 nm for the metallic matrix without particle incorporation up to 30 nm for the composite with 15 g/l bath loading has been measured (Figure 32 A-C). At 20 g/l bath loading the roughness increased arbitrary due to the surface crystal growth which has already been mentioned and will be discussed later on.

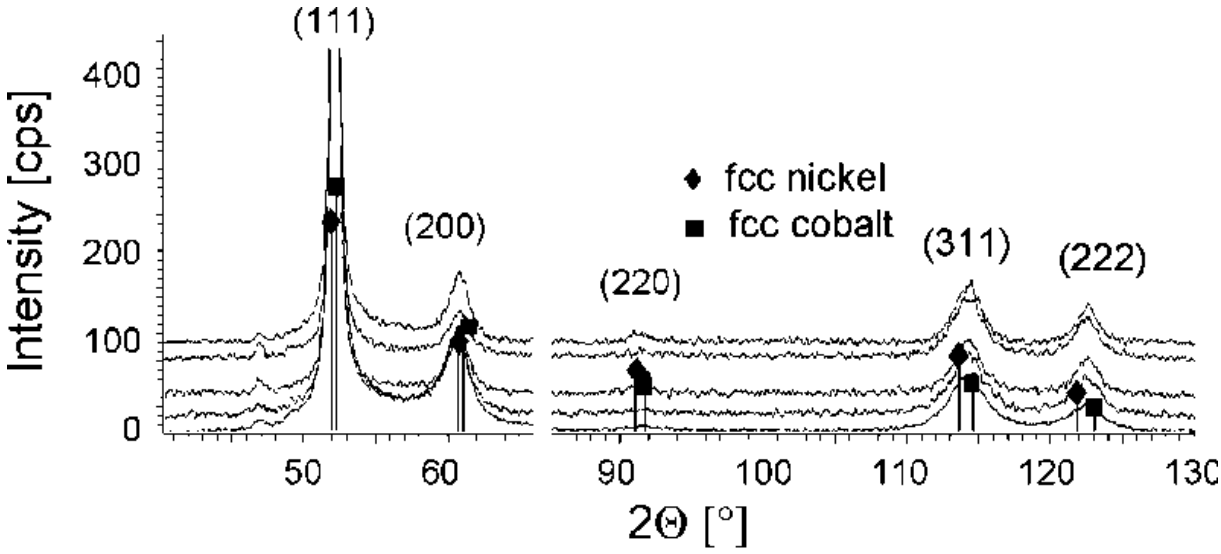

Figure 33: FCC structure of the NiCo, all solid solutions by XRD: pure matrix (lower curve) and all composites (upper curves up to 20 g/l).

Figure 33 summarizes the XRD diagrams of the NiCo sample without particles (bot- tom) and of the NiCo composites with rising particle concentration in the bath (from bottom to top) showing the (111), (002), (311) and (222) peaks. The XRD analysis reveals the face centered cubic (FCC) phase with a mean lattice parameter of 0.353 nm, thus indicating a NiCo solid solution. The lattice parameter is between the values of Ni (0.35280 nm, JCPDS No. 00-004-0850) and Co (0.354470 nm, JCPDS No. 00-015-0806), even though the value is less than

calculated after Vegard's rule due to the observed micro strains in the lattice. Despite the high cobalt concentration a hexagonal close packed (HCP) phase was not detected. The concentration of the ferrite particles is too low for XRD detection. The remarkably high (111) peak gives evidence for a (111) fibre texture of the electrodeposited NiCo matrix, although no further texture analysis was done. The position of the (002) peak is slightly shifted to lower values suggesting stacking faults and twins which were observed by LV-STEM and TEM, too. Due to the (002) peak shift the coherence lengths have been derived by analysing the single peaks by means of the TOPAS software. The coherence length of the (111) crystal plane in the direction of the layer growth is 14 nm for the matrix without particles and between 25 and 27 nm for the composites with detectable and constant particle incorporation. The coherence lengths of the other planes are around 10 nm; these planes show in addition a noticeable strain. The difference in the coherence length suggests that crystals with the orientation of the fibre texture grew larger than the others. In summary, the expected nano-grained metal matrix has been confirmed by XRD. Moreover, crystal sizes around 10 or 20 nm are revealed by LVSTEM imaging. Figure 34 shows the matrix without particle incorporation. The crystals can be distinguished by orientation contrast in the bright field image and show a broad distribution of the crystal size around 20 nm. It should be noted that the observation direction is the deposition direction respectively the direction of the (111) fibre which is consistent with the large amount of crystallites with a size below 10 nm. Figure 35 is typical for all composites with 0.2 wt. % particle incorporation. The metallic matrix shows again a large number of "10 nm"-crystals in observation direction. The incorporated ferrite particles are hardly to be distinguished due to very small mean atomic mass difference of the barium ferrite particles and the nickel cobalt solid solution, and as a consequence the low contrast difference. The particles have been localized by comparing backscattered electron images and thus could be marked in the LVSTEM image by circles. The particle size, around 40 nm, is remarkably larger as specified by the producer which seems evidence of particle agglomeration. Unfortunately, it was not possible to answer this question by TEM at 200 kV. Some of the

particles can be distinguished a little bit clearer (marked by arrows in Figure 36), but the Moiré Fringe patterns of the matrix crystals lying on each other impede a clearer picture.

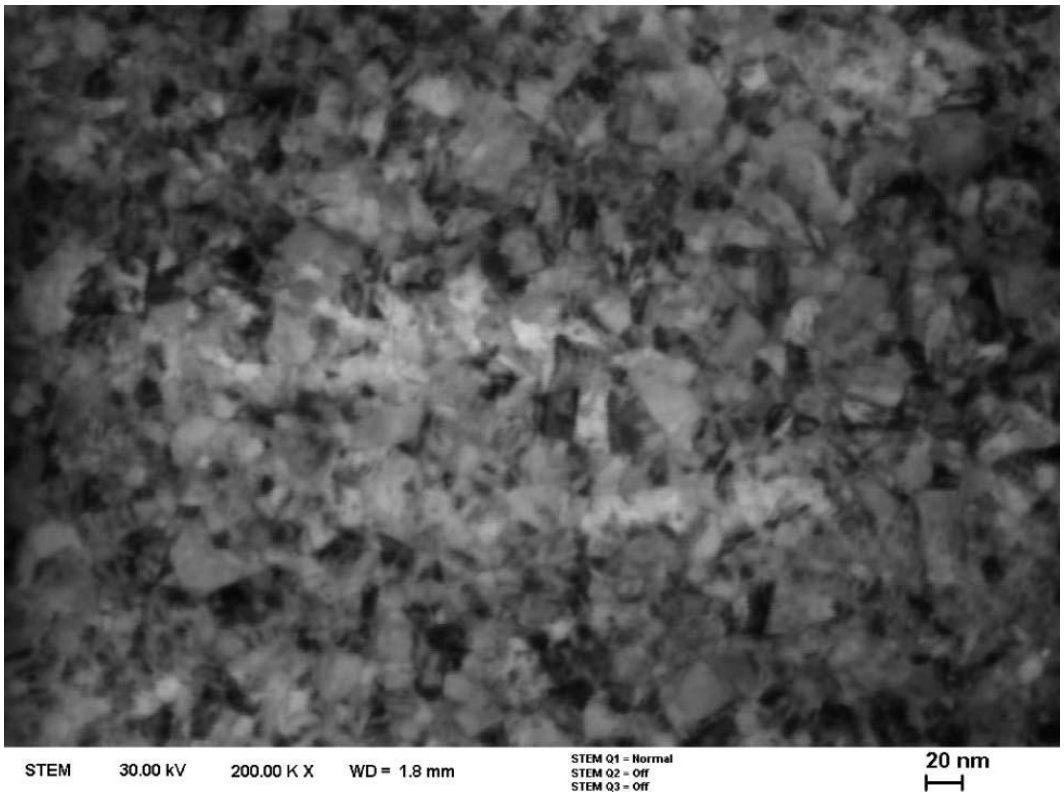

Figure 34: Nano-grained NiCo matrix by LVSTEM.

The cross-section of the composite with 20 g/l particle bath load shows a columnar crystal growth in the surface region at the layer–bath interface which was not observed in composite layers with lower bath load. This columnar crystal growth has been observed on the surface as well as in the cross-section by SEM (Figure 37A). We used EBSD-based orientation mapping for some more knowledge of the microstructure of the larger grains near the surface (Figure 37B). A few microns of the top of the 20 g/l- composite layer contain columnar crystals in the sub-micrometer range. Similar to the composites with lower bath loading the greater volume fraction is truly nano-

crystalline with equiaxed FCC grains which are in contrast to results in [87]. Due to the limited EBSD resolution (step size 50 nm) the measured grain size distribution ends at 70 nm and cannot reflect the complete grain size distribution as established by XRD at the lower end.

The pole figure confirms a (111) fibre texture in the layer normal which confirms the texture suggested by the raised (111) peak of the XRD diagrams. The composition regarding the matrix and the particle content is unchanged compared to the nano-grained part of this composite.

Summarizing, we deposited two types of layers distinguishable by their microstructure. One type is a pure NiCo nano-grained matrix without particle incorporation, the other is a composite of a nano-grained NiCo matrix and a barium ferrite particle content of 0.2 wt. %. For these two types, the magnetic properties were derived from SQUID magnetometry at room temperature. The results are consistent with the structural characterisation.

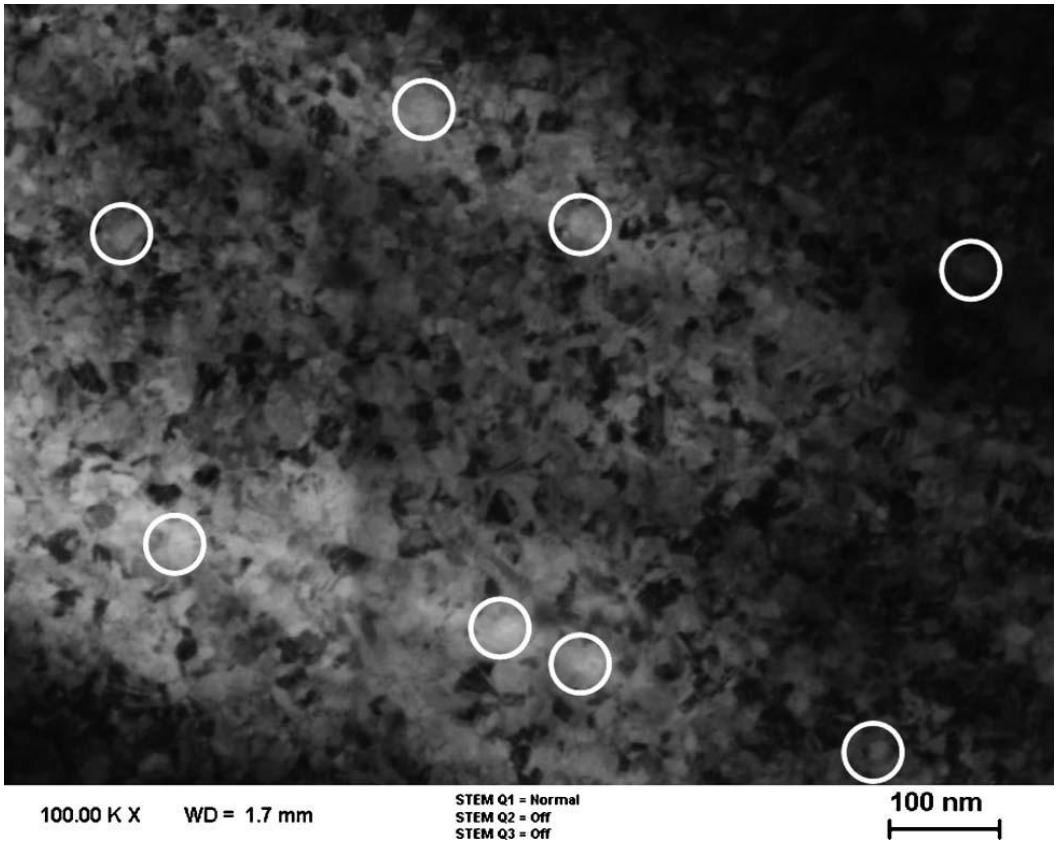

Figure 35: Particle distribution in the NiCo matrix by LVSTEM.

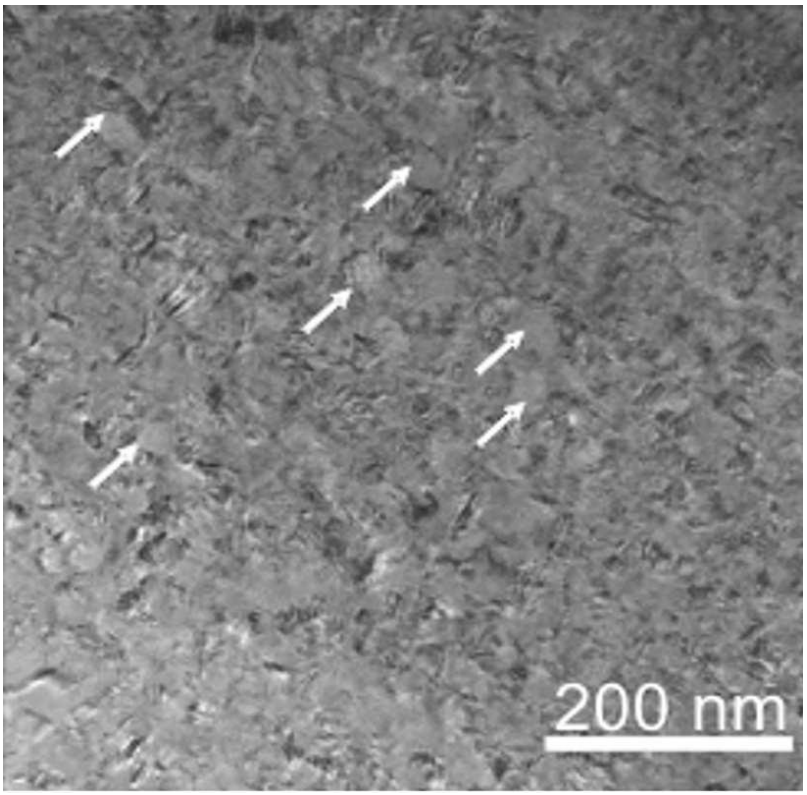

Figure 36: Particle agglomeration by TEM.

The soft magnet matrix dominates the global behaviour. Minimization of the stray field energy (shape anisotropy) forces the magnetization into the film plane, resulting in the typical hard-axis behaviour of the magnetization perpendicular to the film plane with a saturation field of ≈ 1.15 T (Figure 38A). The in plane magnetization (Figure 38B), follows roughly the curve expected for an easy axis magnetization. The saturation fields are in the range that can be expected for NiCo alloys. The small coercivity and the peculiar rounding of the magnetization curve as they approach saturation could indicate superparamagnetism. This, anyway improbable due to the strong coupling of the particles to the matrix, was excluded by temperature dependent measurements.

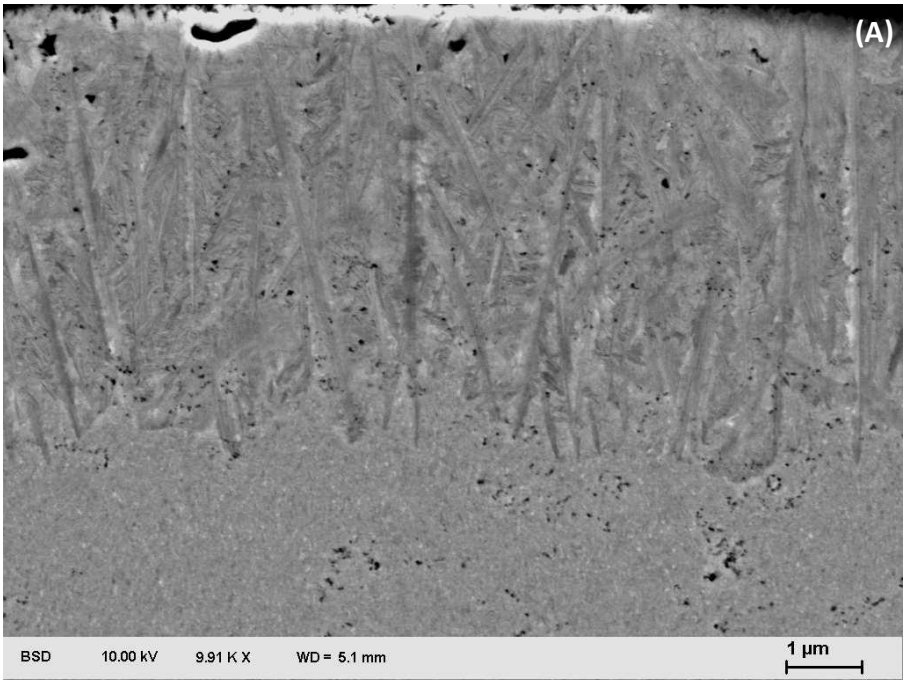

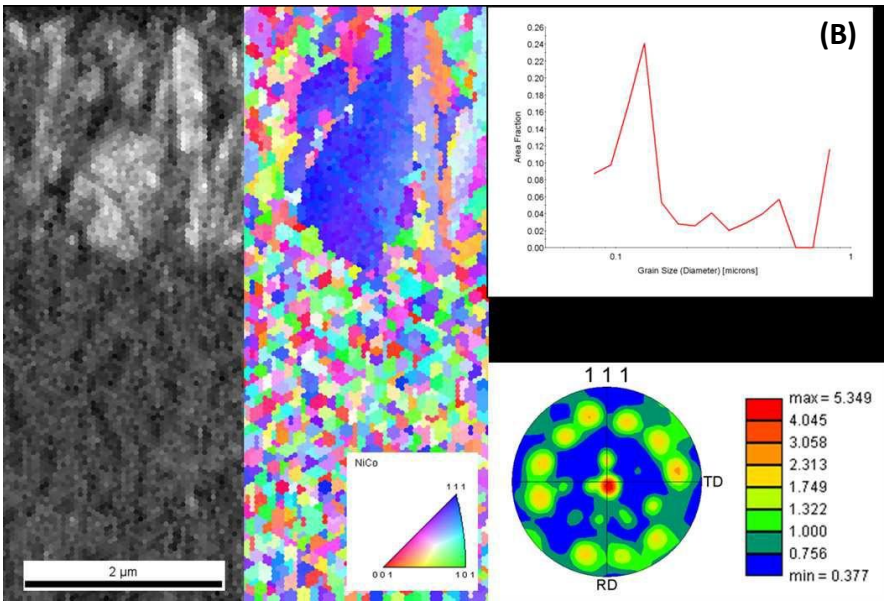

Figure 37: Columnar crystal growth at the surface of a NiCo composite: (A) SEM image, (B) EBSD results (quality map, orientation map, grain size distribution, (111) fibre texture // layer normal).

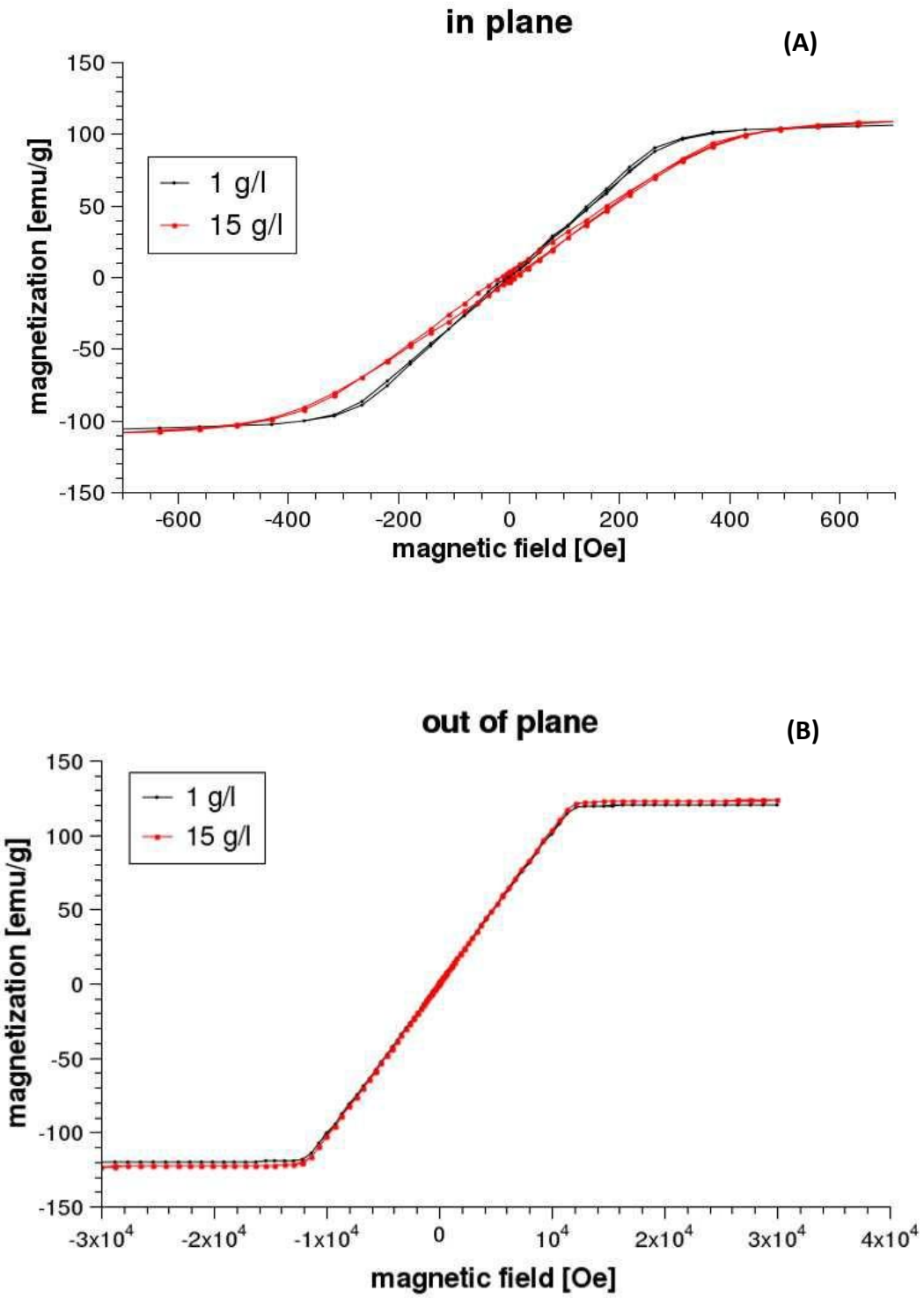

Figure 38: Magnetization vs field curves at room temperature for NiCo and the composite: (A) out-of plane measurement – matrix property, (B) in-plane measurement – influence of the particles.

The magnetization at a low field of 1590 A/m marginally depends on the temperature, decreasing by 2% during cooling to 10 K. Assuming the barium ferrite particles to be randomly oriented, the rounding of the magnetization curves, the higher saturation field for the composite sample and the slight decrease of the magnetization with temperature are interpreted as follows: the randomized anisotropies of the ferrite particles impress their magnetization direction into the surrounding matrix, resulting in a certain amount of non-collinearity of the magnetic moment. This non-collinearity would be more pronounced at higher particle concentrations, resulting in the higher saturation field. The saturation magnetization, however, is for both the solid solution and the composite nearly identical, showing conclusively that the moment is dominated by the matrix and not by the particles, and thereby, that the non-collinearity extends into the matrix. Higher anisotropies at lower temperatures lead also to an increase in the non-collinear moment, thereby explaining the slight decrease of the low-field magnetization at lower temperatures.

Summing up, despite the low barium ferrite particle incorporation rate, the relatively high anisotropy of the composite with very low coercivity, and very low remnant magnetization at room temperature would be a very useful property for MEMS. For such applications enhanced incorporation of nano-sized ferrite particles is highly desirable. However, this will not be reached by enhancing particle content in the plating bath. Further studies regarding the electrochemical process have to be done.

3.3 Incorporation of Ferrite Nanoparticles into NiCo matrix using Forced Flow Mechanism

In the codeposition mechanism, the aim is the incorporation of barium–strontium ferrite particles into the NiCo electrodeposited matrix forming a composite coating. In order to

enhance this process, studies on plating bath composition were done in order to find the optimal load of dispersed phase in the electrolyte and afterwards a series of microstructure, morphological, magnetic and mechanical characterizations were performed on the layers obtained.

In all conditions, the composition of the galvanostatically prepared deposits was determined by XRF method.

Table 6 shows a significant incorporation of particles in the metal matrix and that this clearly increases upon increasing the bath ferrite concentration. Nickel percent- age remained practically constant but cobalt percentage did decrease gradually as particles percentage increased. Anomalous codeposition was limited, then, in the tested bath by ferrite incorporation.

Electrolyte	Wt. % Ni	Wt. % Co	Wt.% $Fe_{12}O_{19}Ba_{0.2}Sr_{0.8}$
NiCo without barium ferrite	52.94	47.06	–
NiCo + 1 g L^{-1} barium ferrite	53.94	45.46	0.6
NiCo + 5 g L^{-1} barium ferrite	53.83	37.11	9.06
NiCo +10 g L^{-1} barium ferrite	53.74	28.86	17.4
NiCo + 15 g L^{-1} barium ferrite	55.36	24.61	20.03

Table 6: Composition in weight percent of NiCo and NiCo / $Fe_{12}O_{19}Ba_{0.2}Sr_{0.8}$ deposits.

Using the flow cell, barium ferrite particle incorporation becomes uniform. Figure 39 A, B and C shows an overview of the layers obtained with particles' load respectively of 0 and 5 g L^{-1}. Clear changes in morphology were obtained for deposits prepared in absence or presence of particles. Figure 39D shows the composition by EDS spectrum. A mapping study of the surface makes in evidence the good distribution of the particles (Figure 39E).

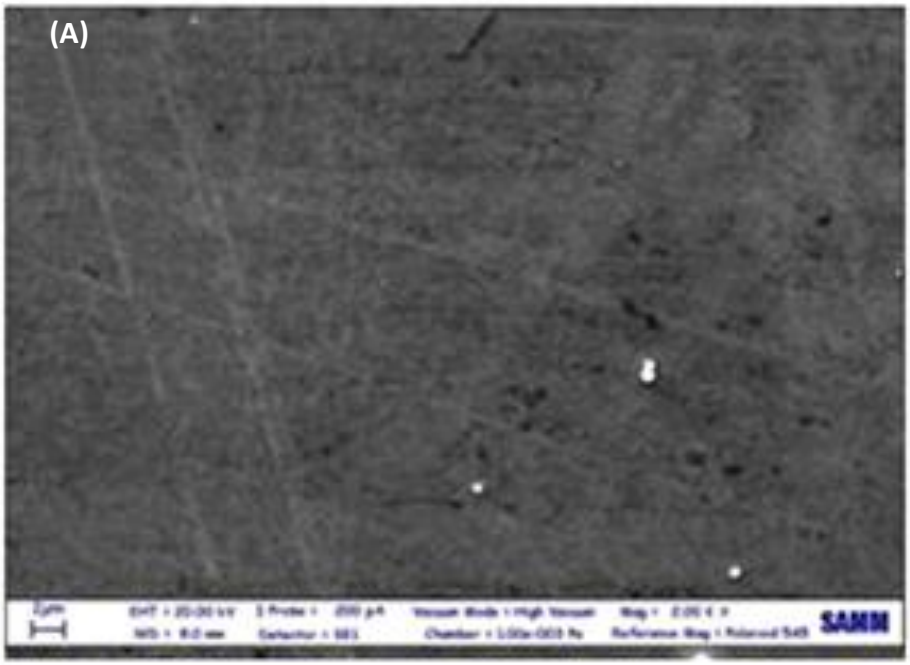

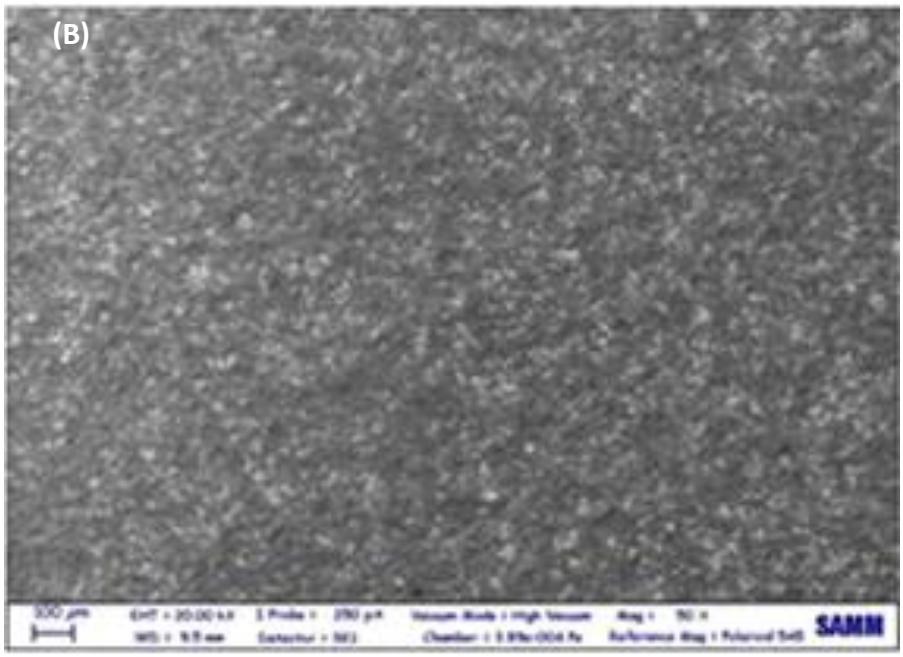
(B)
SAMM

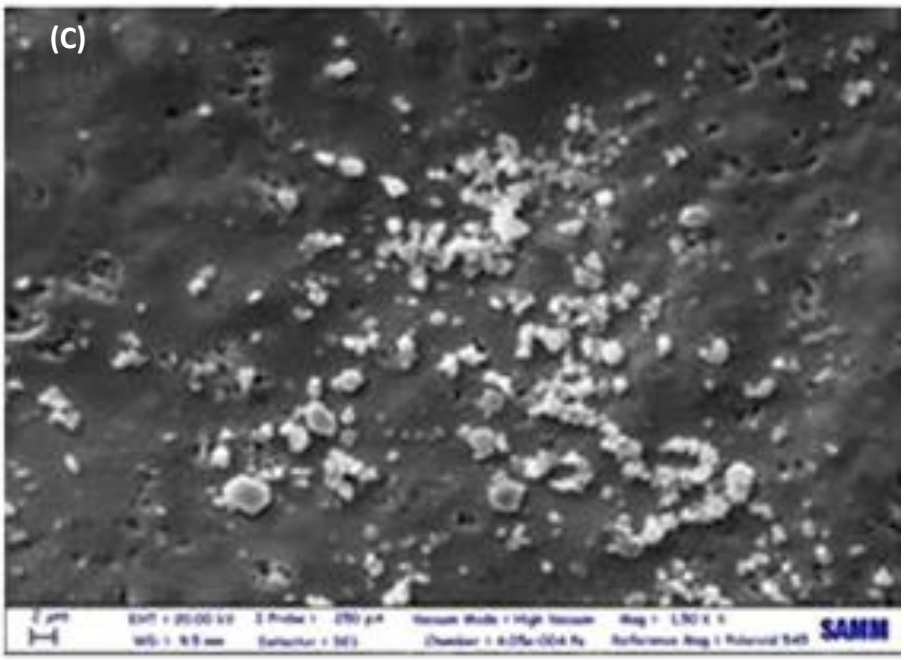
(C)
SAMM

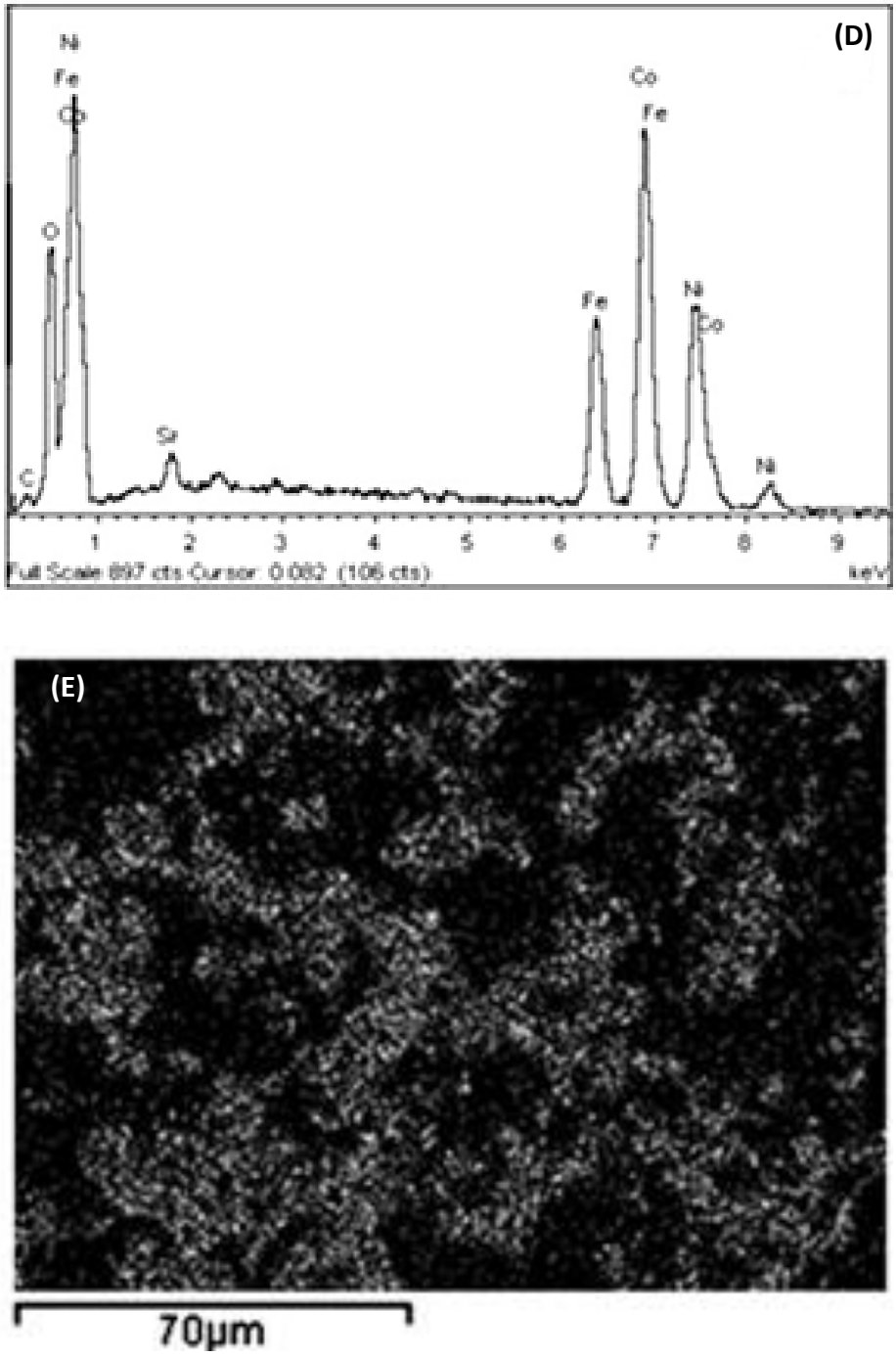

Figure 39: SEM images of coatings with particle's load of 0 and 5 g L^{-1}: (A) NiCo alloy, (B) NiCo/5 g L^{-1} Ba–Sr ferrite, (C) NiCo/5 g L^{-1} Ba–Sr ferrite (zoom), (D) NiCo/5 g L^{-1} Ba–Sr ferrite (EDS spectrum of zoom area), (E) NiCo/5 g L^{-1} Ba–Sr ferrite (mapping of iron presence in the surface).

In order to study the incorporation of barium ferrite particles in NiCo matrix during the electrodeposition process, deposit cross- section was analyzed by SEM. Cross-section images reveal a gradual increase in ferrite particle incorporation into the metal matrix on increasing particle concentration in the solution. However, from 20 g L^{-1} a decrease in the particles incorporation was observed. Ferrite incorporation of the NiCo matrix leads to a distortion in its micro- structure, which is more marked as the number of particles embedded increases. A high deformation level of the microstructure hinders deposition process, reducing the number of particles incorporated. A good distribution of particles throughout the deposits was observed, especially in the range 5–10 g L^{-1} (Figure 40).

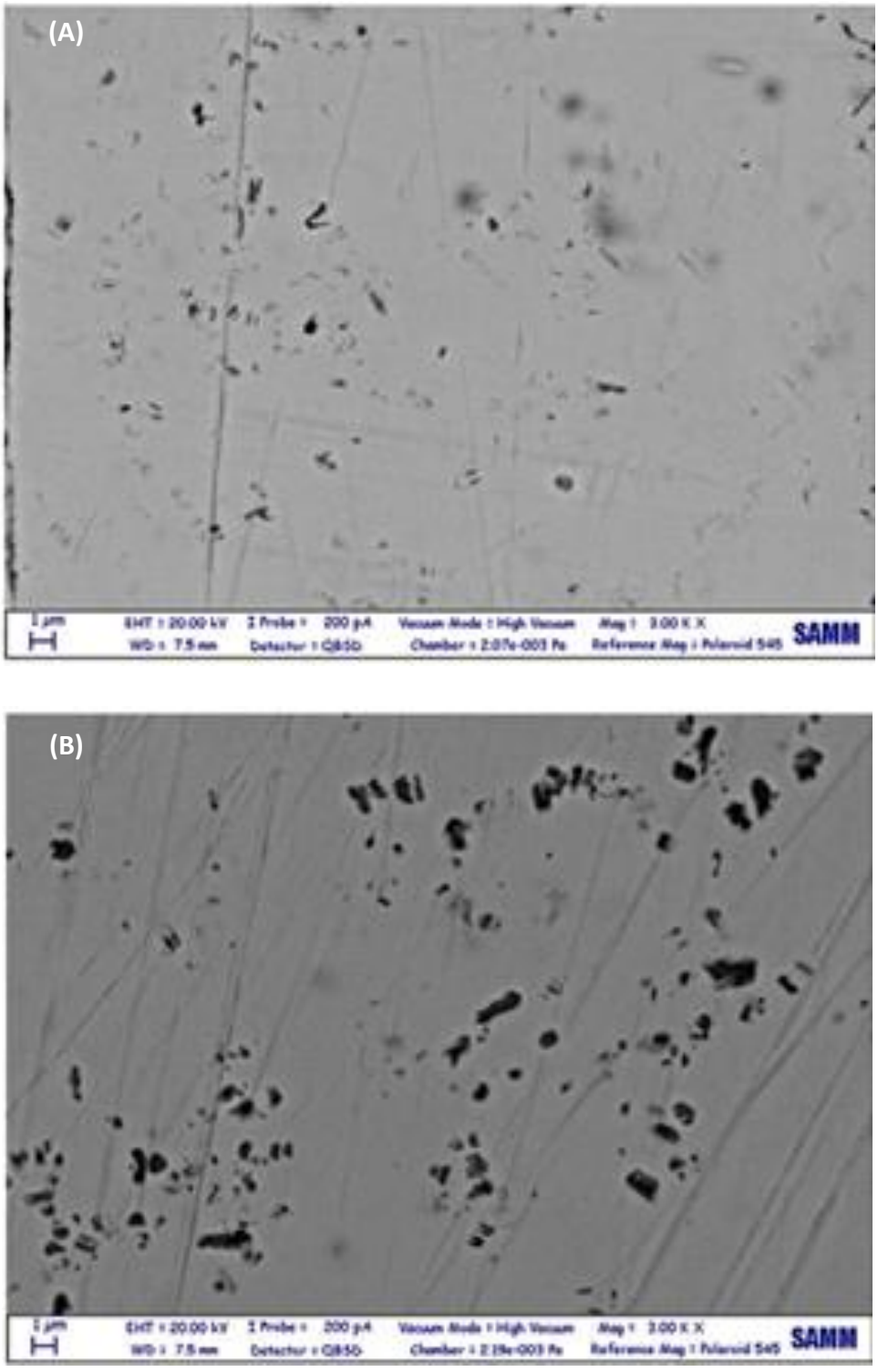

Figure 40: Detail of the cross-section of : (A) NiCo /5 g L^{-1} Ba–Sr ferrite and (B) NiCo/10 g L^{-1} Ba–Sr ferrite.

To see how the layer microstructure was changed depending on particle load, XRD analysis was used. For each deposit, and therefore for each particle load used, a diffractogram was recorded. Typical FCC phase was observed for NiCo in all samples (Figure 41).

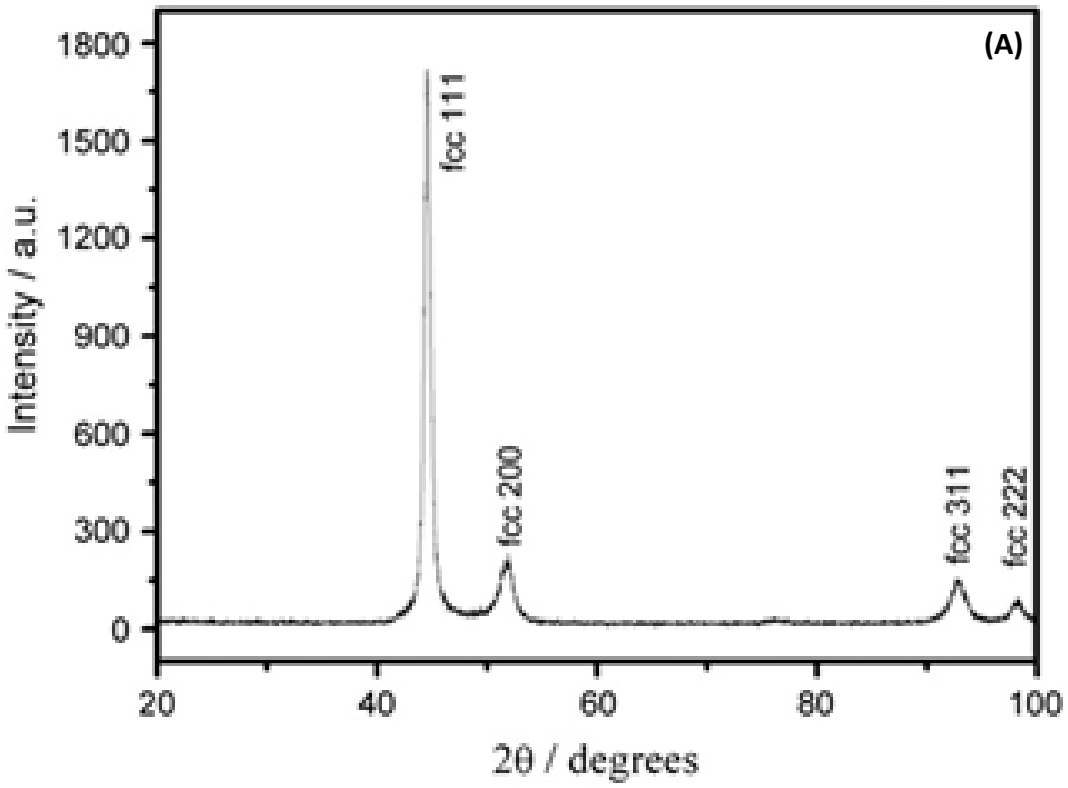

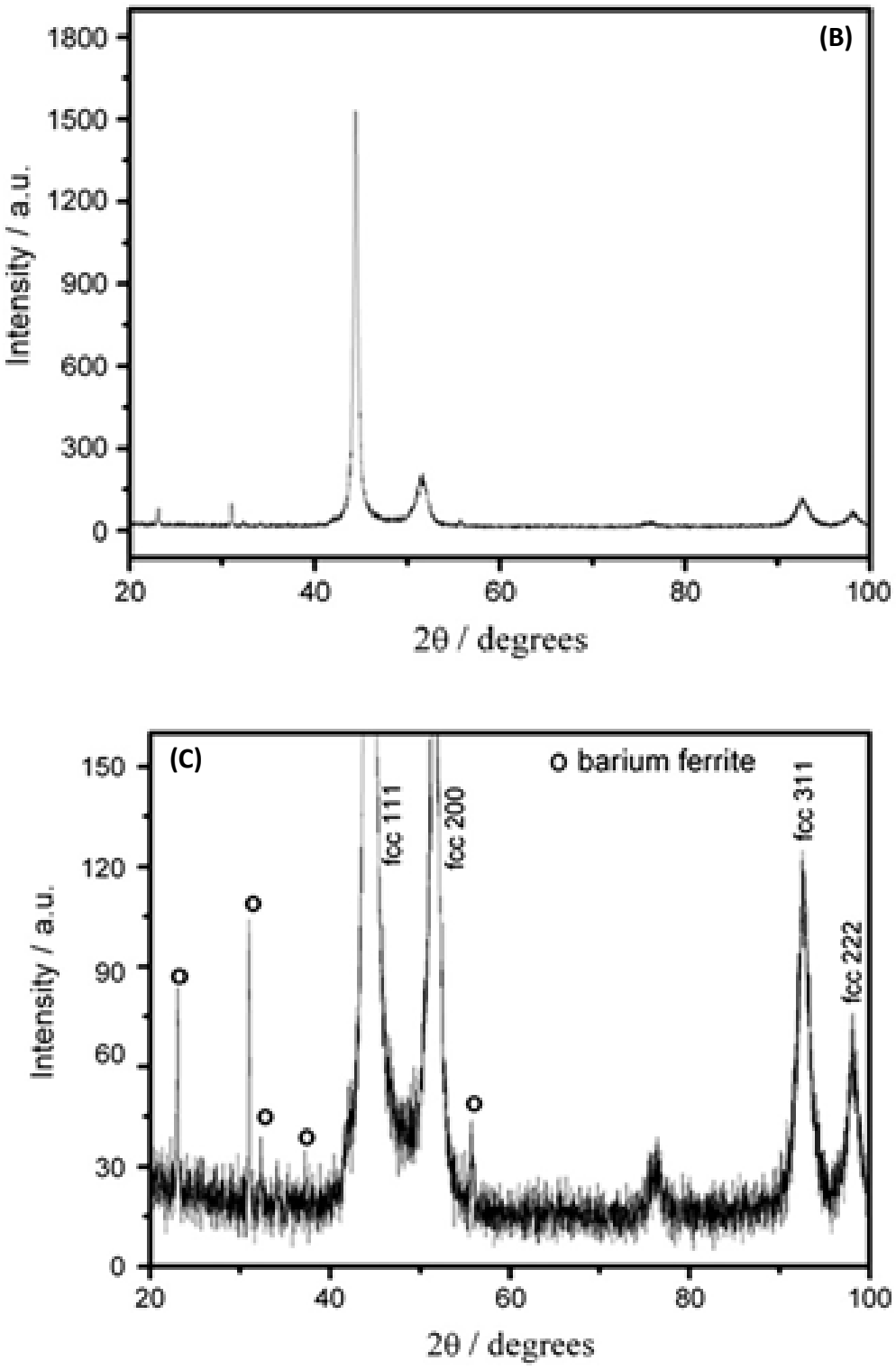

Figure 41: Diffraction peaks of (A) NiCo, (B) NiCo/5 g L^{-1} particles, (C) NiCo/5 g L^{-1} particles – zoom area.

Simultaneously, in deposits containing ferrites, a zoom of the diffractogram reveals the presence of several peaks attributable to ferrite. No significant changes in the relative intensities of the NiCo peaks were observed. It was possible to calculate the grain size average for each concentration of particles in the bath, obtaining its evolution in correlation with the number of particles in suspension in the electrolyte. This has been done following the equation of Debye–Scherrer, based on those parameters that characterize the peaks in the diffractograms, such as amplitude of the peak and peak position. The grain size slightly decreased on increasing particle load in the bath. Nanocrystalline layers have been also obtained although the incorporation of particles has a market influence on the structure of the coating; in fact the grain size decreases as the load of particles becomes higher. This trend is due to the influence that particle incorporation has on the nucleation process of alloy's grains: the particles act like obstacles in the formation of new grains, limiting their growth and reducing their size.

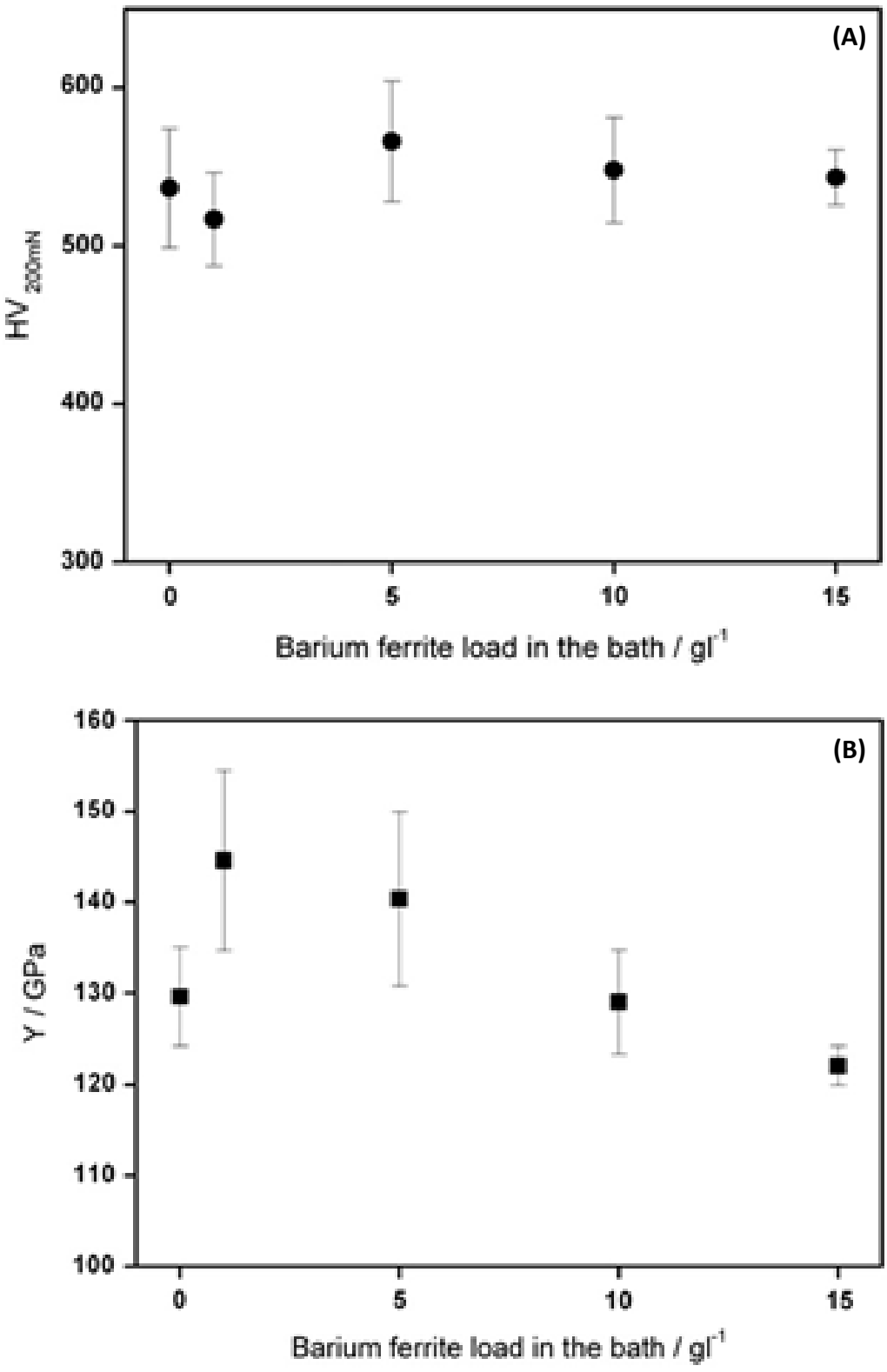

Figure 42: HV vs load of particles (A) and Young modulus vs load of particles (B).

The decrease in grain size, and in general microstructure modification, in the coating must have consequences on the mechanical properties; this has been investigated via microhardness and elastic Young's modulus measures (Figure 42).

Microhardness is influenced mainly by the number of incorporated particles, but as said before, grain size also contributes to the value of this parameter. The microhardness generally increases with the presence of particles; we can observe a peak at particle concentration of 5 g L^{-1}. This peak is confirming what we have noticed with current's efficiency, namely that this particle load could be the optimal one for the processing conditions adopted in this paper, in terms of number of particles incorporated and also of mechanical characteristics of the coating. However, we can observe that the values of microhardness do not differ much, revealing the dualism that exists between particles incorporated and grain size: in fact, for higher values of particles incorporated and relatively higher grain size (5 g L^{-1} Ba–Sr ferrite) we have almost the same value of microhardness obtained with a layer with a smaller number of particles incorporated and grain size (10 g L^{-1} Ba–Sr ferrite). Indeed, the elastic modulus evolution is characterized by a peak for the load of 1 g L^{-1} of particles and then decreases progressively.

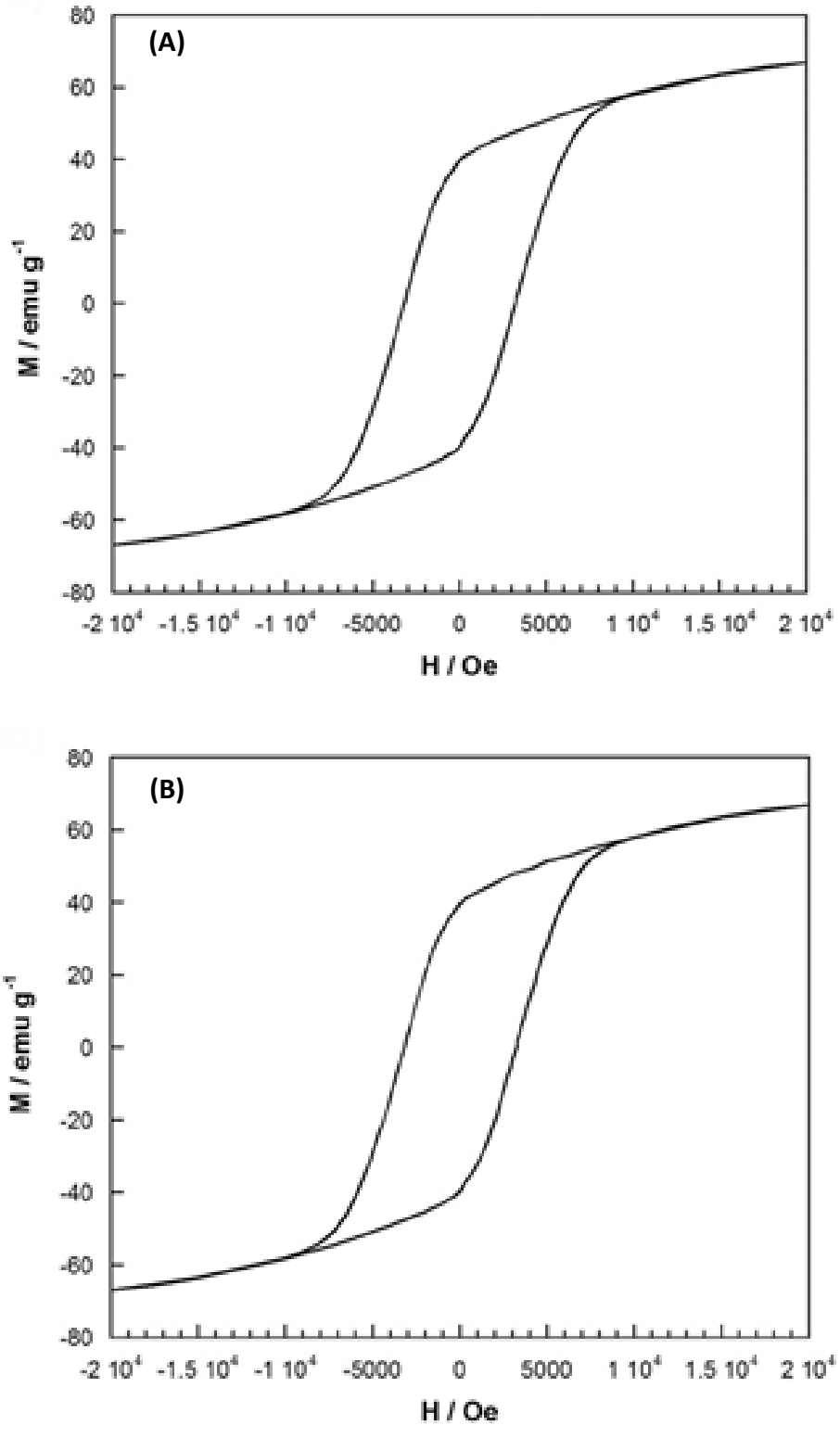

Figure 43: M–H curves Ba–Sr ferrites, (A) before, and (B) after immersing them in the electrolyte solution.

Due to the ferromagnetic behavior of the particles used, the magnetisation–magnetic field curves of the samples were recorded as another manner of detecting composite formation. Particles used were previously magnetically analyzed. The magnetisation–magnetic field curves were recorded before and after introducing the particles into the work solution during 48 h in order to determine their stability in the electrolytic bath (Figure 43). Ba–Sr ferrite particles were, as expected, hard-magnetic with a coercivity of 3200 Oe; the same magnetic response was obtained after immersing the particles into the solution, showing their stability.

Figure 44 shows the comparison between pure NiCo deposits and NiCo-$Fe_{12}O_{19}Ba_{0.2}Sr_{0.8}$ composites. Soft-magnetic behavior of NiCo didn't change in the presence of the incorporated particles. Particle inclusion did not provoke the formation of the more anisotropic hcp structure of NiCo and, thus, no increase in the coercivity of the layers was detected. A slight decrease of the coercivity was even observed probably as a consequence of the grain size variation. The presence of moderate percentages of hard-magnetic particles dispersed in the metal matrix was not enough to confer hard- magnetic behavior to the coating and the resulting composite, of FCC structure, maintained the soft-magnetic behavior. The magnetization of saturation was dependent on the Co content in the deposit. Magnetisation of saturation (Ms) slightly decreased as the Co percentage in the composites decreased.

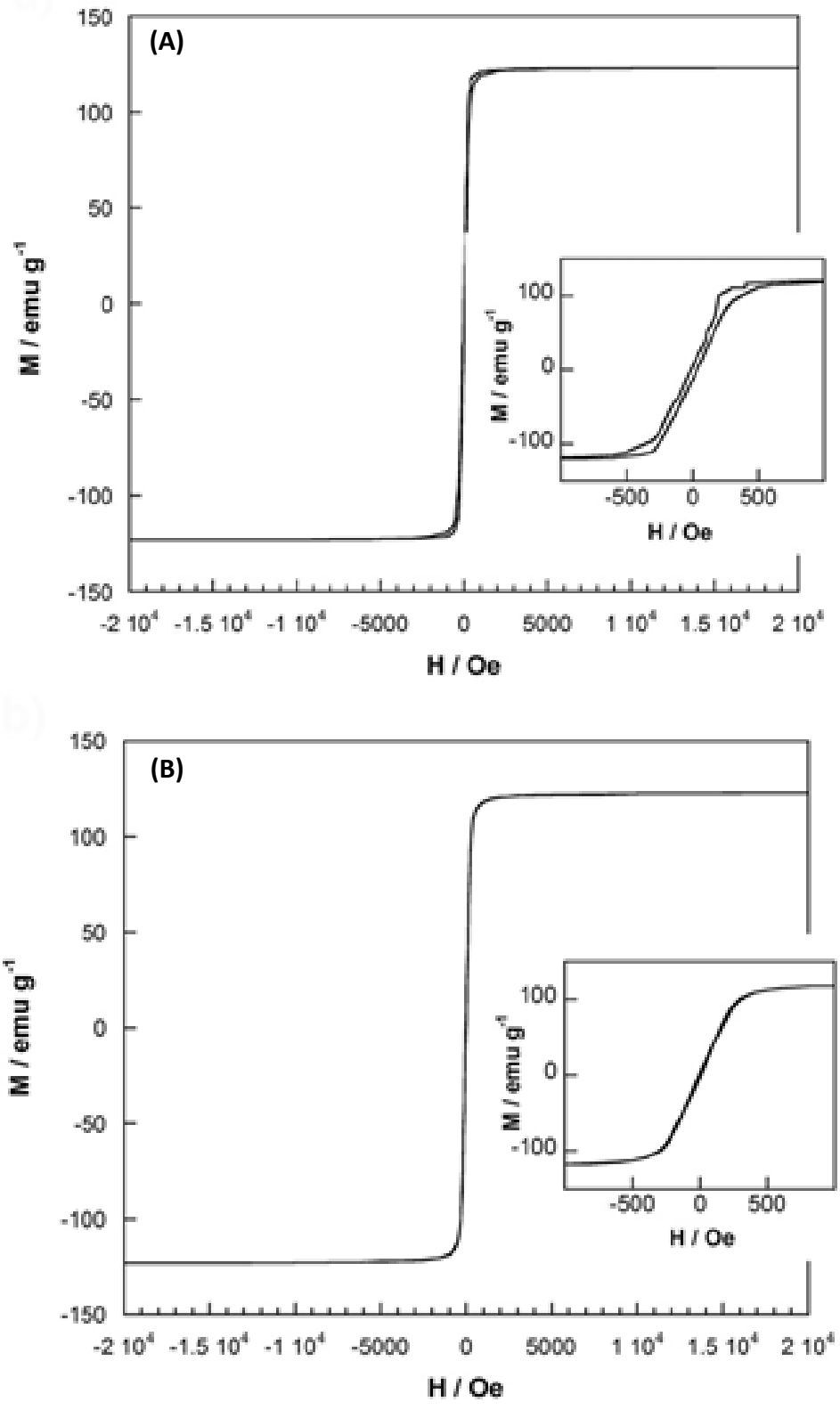

Figure 44: M–H curves for (A) NiCo and (B) NiCo/15 g/L Ba–Sr ferrite.

3.4 NiCo Nanowires with Embedded Ferrite Nanoparticles

The potential vs time curves during the deposition were recorded and compared with those obtained from the solution ferrite-less. More negative potentials were attained when the solution contained nanoparticles (Figure 45A). Probably, alloy nucleation into the porous channels was hindered when electroactive species and nanoparticles entered simultaneously in them. After 1 hour of deposition, nanowires of around 10 µm length were obtained: Figure 45B and C shows the average length of the nanowires and some of their detail is shown in inset pictures.

For observation of the nanowires by HRTEM and determination of both composition and crystalline structure, an etching of the membranes with 0.1 M NaOH was made. The nanowires were analyzed by EDS-TEM. Average composition was 82 wt.% Ni + 18 wt.% Co from the nanoparticles-free solution and 78 wt.% Ni + 15 wt.% Co + 7 wt.% barium ferrite from the solution with nanoparticles.

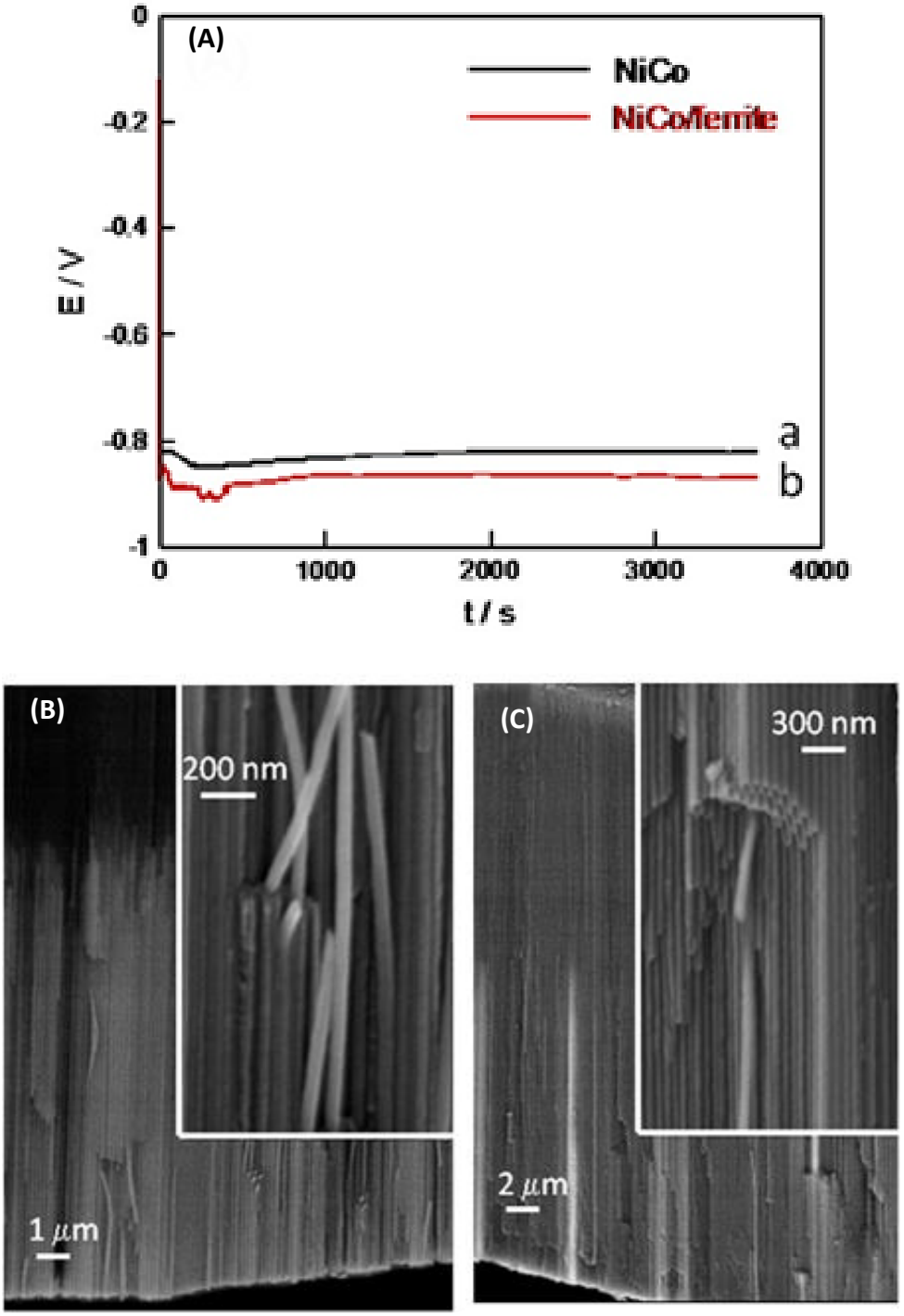

Figure 45: A) E–t transients of the galvanostatic deposition of (a) NiCo nanowires, (b) NiCo/ferrite nanowires and SEM images of the resulting nanowires (B) and nanowires composite (C) into the alumina membrane.

Nanowires obtained were crystalline (Figure 46). Pure NiCo nanowires correspond to Co HCP phase with 100 textures and a low proportion of FCC phase. The same phase and texture was observed in NiCo/ferrite nanowires, revealing that nanoparticles in the bath slightly impede deposit nucleation and growth but do not affect significantly crystalline growth development. The moderate sample signal and the low ferrite amount difficult the detection of the ferrite reflection peaks in the X-ray diffractograms. The comparison of the diffractogram of NiCo/ferrite nanowires with that of pure nanoparticles allows to detect, as the clearest peak of ferrite, the small peak at around 37°2θ. Then, in nanowires of both NiCo and NiCo/ferrite, HCP + FCC phases were detected whereas NiCo or NiCo/ferrite films obtained from the same bath showed only FCC phase [88, 89]. NiCo electrodeposition into the porous channels conditioned the crystalline structure.

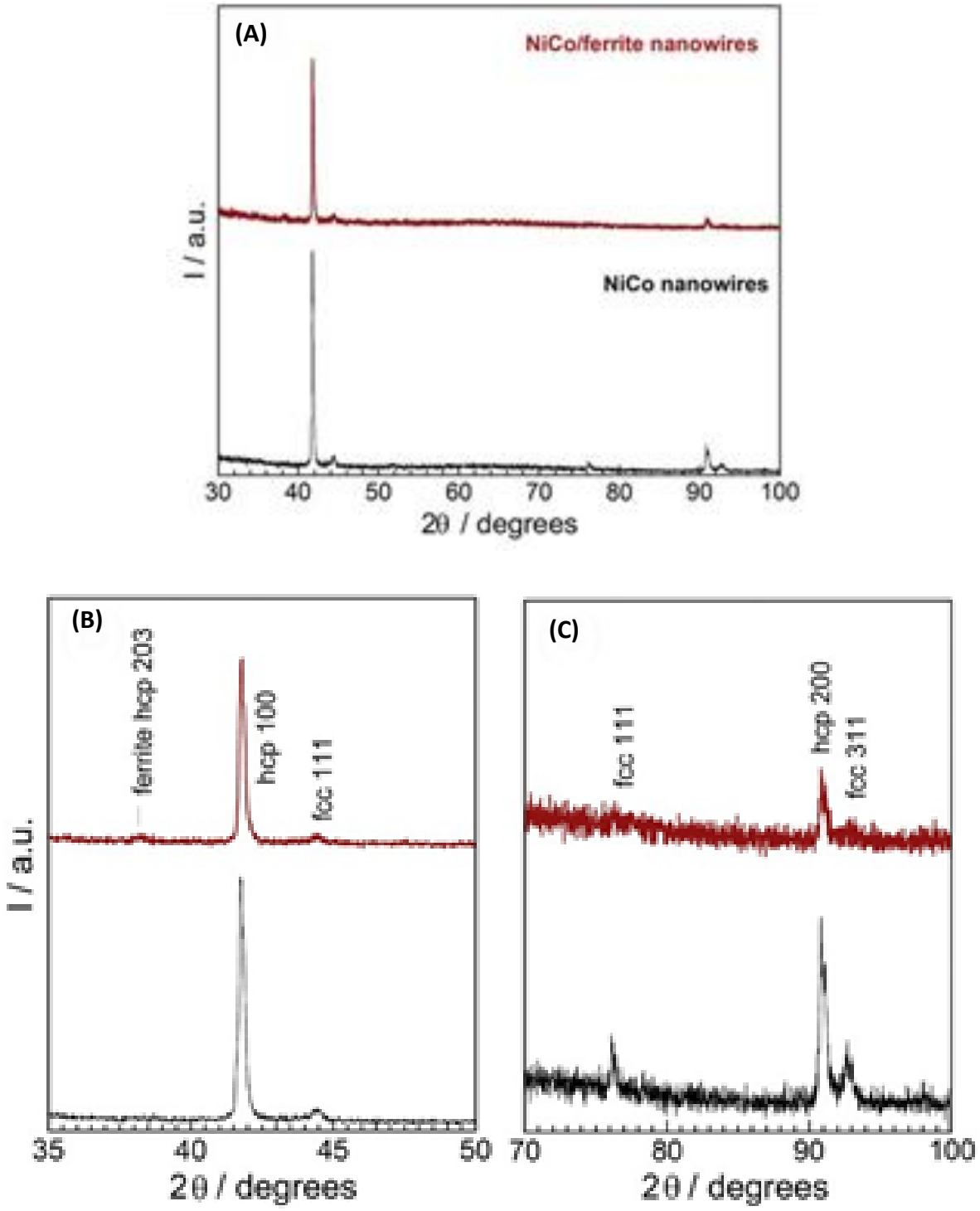

Figure 46: X-ray diffractograms of the nanowires and zoom details.

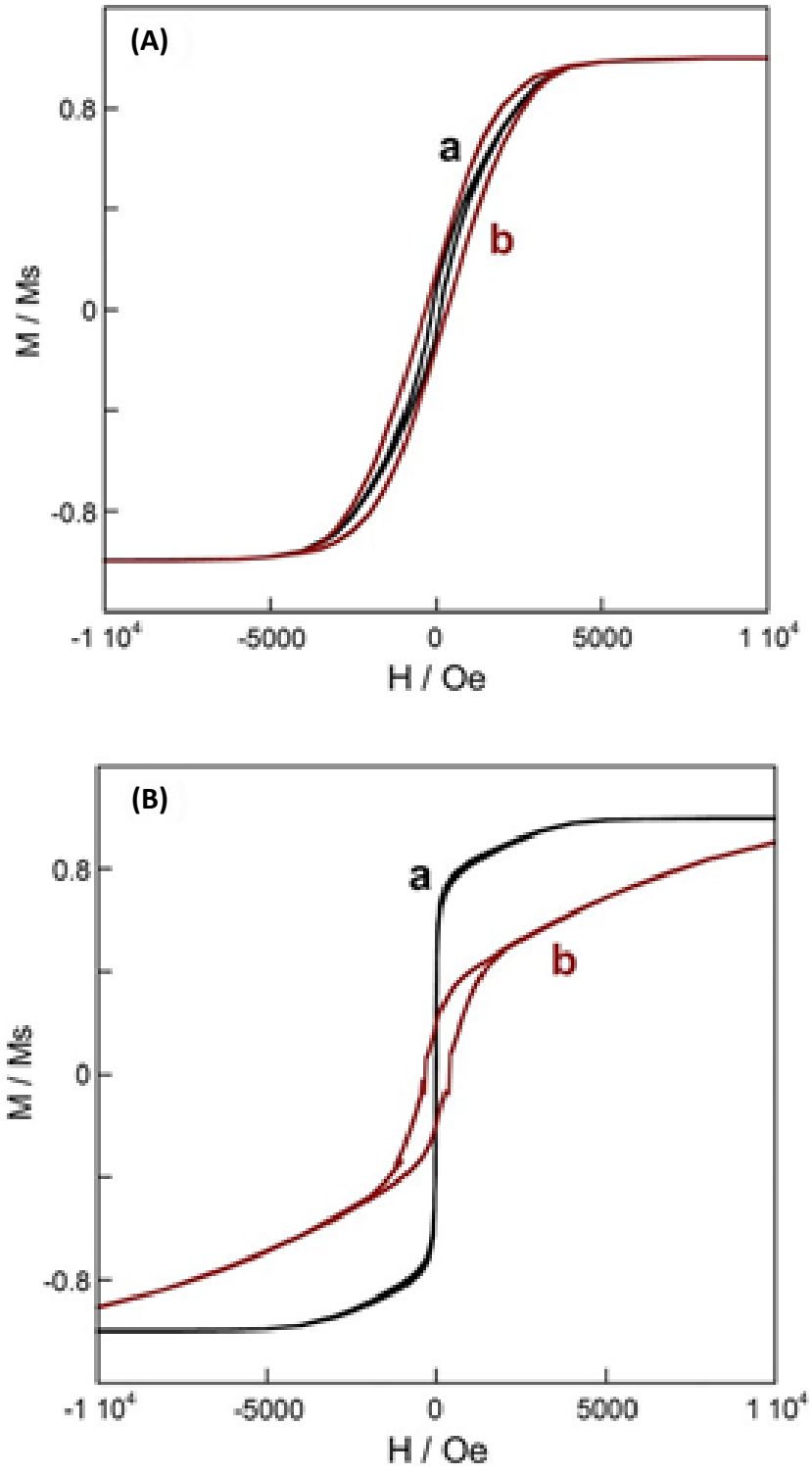

Figure 47: Magnetization–magnetic field applied with the membrane parallel (a) or perpendicular (b) to the magnetic field. A) NiCo nanowires, B) NiCo/ferrite composite nanowires.

Ferrite incorporation into the NiCo matrix was corroborated by HRTEM observation. Nanowires were released of the membrane without damage. Particle distribution, with sizes lower than 10 nm, was clearly observed. Low particle agglomeration inside the nanowire was detected, which demonstrates the formation of composite nanowires. The focalized analysis by EDS allows us to confirm that the nanoparticles corresponded to barium ferrite and the matrix to NiCo alloy.

Magnetic response of the composite nanowires was compared with that of nanowires without nanoparticles (Figure 47). For pure-NiCo nanowires similar magnetic curves were observed by applying parallel or perpendicular magnetic fields, which reveal very low magnetic anisotropy; similar behavior has been observed in other alloy nanowires as a function of their aspect ratio [90]. Composite nanowires (soft-magnetic NiCo matrix with hard-magnetic particles) give also single phase magnetic behavior (non-constricted shape) but high magnetic anisotropy is now observed: samples were easily magnetized when the magnetic field was applied parallel to the membrane (i.e. perpendicular to the nanowires), increasing magnetic remanence. The presence of the particles along the nanowire modifies the magnetostatic dipole interaction among the wires, which will induce a magnetic easy axis perpendicular to the nanowire axis.

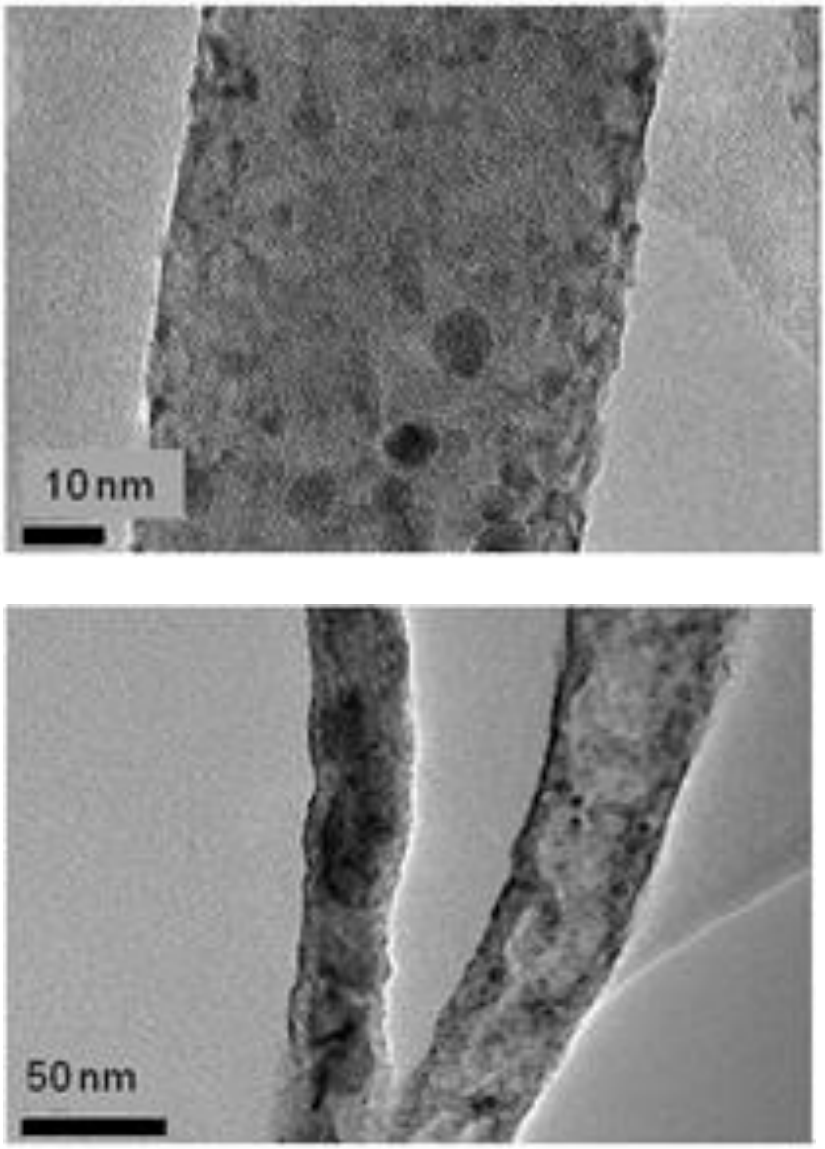

Figure 48: TEM pictures of the resulting composite nanowires.

The presence of the magnetic nanoparticles into the NiCo matrix deposit clearly influences the magnetic character of the nanowire arrays, inducing soft-magnetic behavior when the membrane is placed parallel to the magnetic field whereas a semi-hard one was obtained by placing the membrane perpendicular to the magnetic field.

Chapter 5: CONCLUSIONS

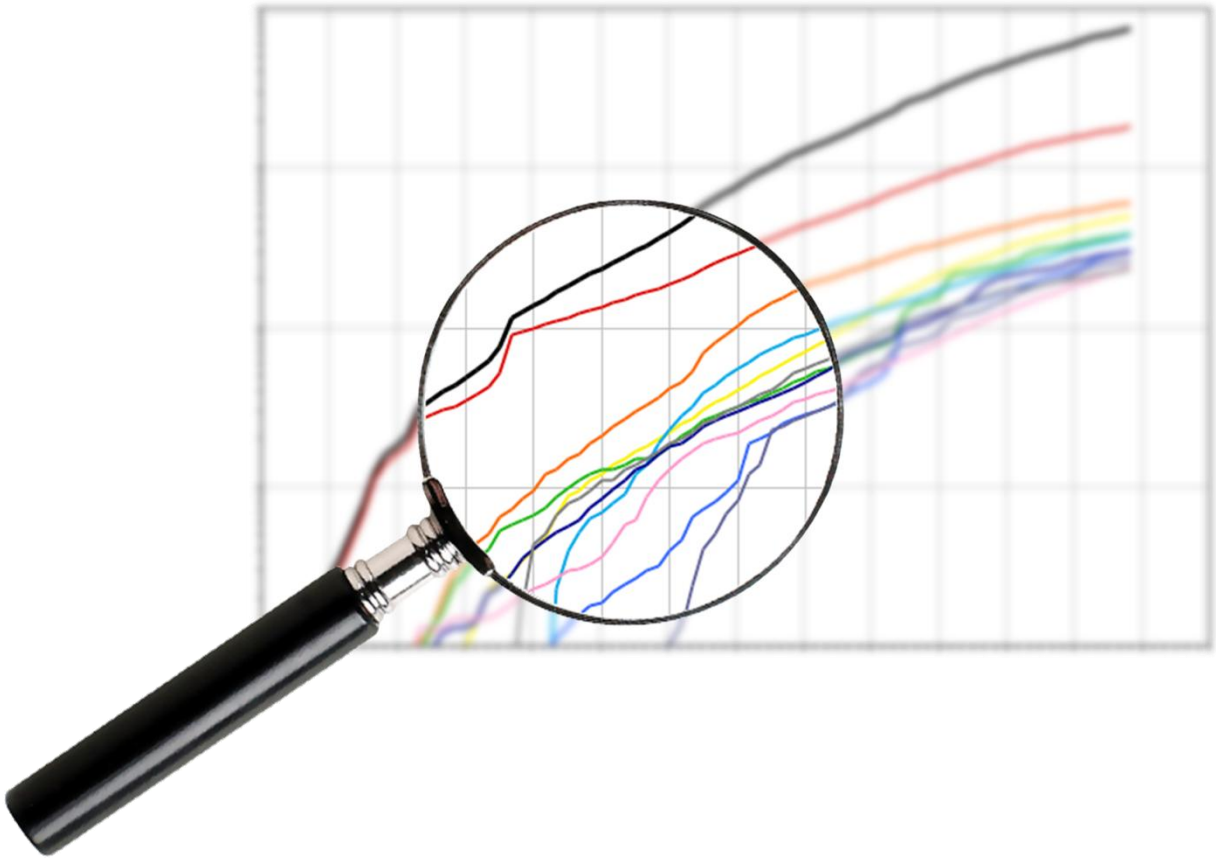

4. Conclusions

4.1 Study of Plain NiCo films formed by Electrochemical Deposition

From the sulphamate bath used, NiCo layers of several microns were compact and fine grained, showing a clear soft-magnetic behaviour with different saturation of magnetisation as a function of their cobalt percentage. No significant variation in their proper- ties was observed when they were prepared from different current densities or temperatures, which led to prepare soft-magnetic non fragile films in a wide range of experimental conditions.

NiCo coating improve the mechanical properties of pure cobalt and pure nickel electrodeposits up to 533 HV [91].

4.2 Incorporation of Ferrite Nanoparticles into NiCo matrix using a Basic Electrochemical Cell

Two types of layers were studied; one type was a pure NiCo nano-crystalline matrix without particle incorporation, the other was a composite of the nano-crystalline NiCo matrix and nano-sized barium ferrite particles. A fixed particle content of 0.2 wt. % is codeposited with varying bath loadings between 5 and 20 g/l. The influence of the incorporated particles on the magnetic properties of the composite becomes apparent in a relatively high anisotropy of the composite with very low coercivity, and very low remanent magnetization at room temperature. The global magnetization behaviour is dominated by the soft magnet matrix. For applications in future higher particle incorporation is crucial [55].

4.3 Incorporation of Ferrite Nanoparticles into NiCo matrix using Forced Flow Mechanism

This study deals about the usefulness of a “Forced Flow” electrolytic cell to perform composite layers codeposition. Specially, the possibility of controlling the ferrites percentage in the deposits as a function of the particles’ concentration in the solution has been

analyzed. It was decided to maintain constant temperature, pH and applied current density, varying only the quantity of particles in the electrolyte. Analysis on microstructure, mechanical and magnetic properties of the composite were done, obtaining encouraging results. The cell tested has been demonstrated to be adequate to prepare particles-metal matrix composites, leading to a good distribution into the deposits. This allows reducing the need to use surfactants to improve the particles dispersion. Also, when magnetic particles must be incorporated, the forced flow cell makes unnecessary to apply of a magnetic field during electrodeposition. Increasing particle load, the probability of their incorporation also increases, but a physical effect hindering in the process of absorption will be detected if there are too many particles in the bath. There must be a single particle concentration value in the bath that maximizes incorporation probability and keeps the physical encumbrance within acceptable limits: in our case it seems that 5–10 g L^{-1} is the optimal load for this kind of process [63].

4.4 Incorporation of Ferrite Nanoparticles into NiCo matrix using Centrifugal Cell

The experiments carried out using the centrifugal electrochemical cell were very basic and the idea was proven to be feasible. Initial measurements by the XRF showed inversion of the anomalous behaviour of NiCo electrolyte, i.e. The concentration of Ni in the deposits were found to be more than that of Co which was opposite in the other experiments. The concentration did not seem to be change much, tuning of the fluid dynamics within the cell will be required. The cell maybe used in more detailed experimentation to study the impact of G-forces in the incorporation of Nanoparticles in NiCo matrix.

4.5 NiCo Nanowires with Embedded Ferrite Nanoparticles

The results of the present work demonstrate the possibility of producing, by means of electrodeposition, composite nanowires in which nanoparticles of around 5 nm are

distributed into the NiCo metallic matrix of the nanowire of 50 nm of diameter. The electrolytic bath and the electrodeposition conditions set-up avoid the nanoparticle aggregation and contribute to their continuous incorporation into the template channels. This incorporation opens new perspectives in the field of magnetic nanowires preparation structures with modulated properties. Change in the magnetic properties of the nanowires has been detected when composite was formed [69].

Chapter 5: BIBLIOGRAPHY

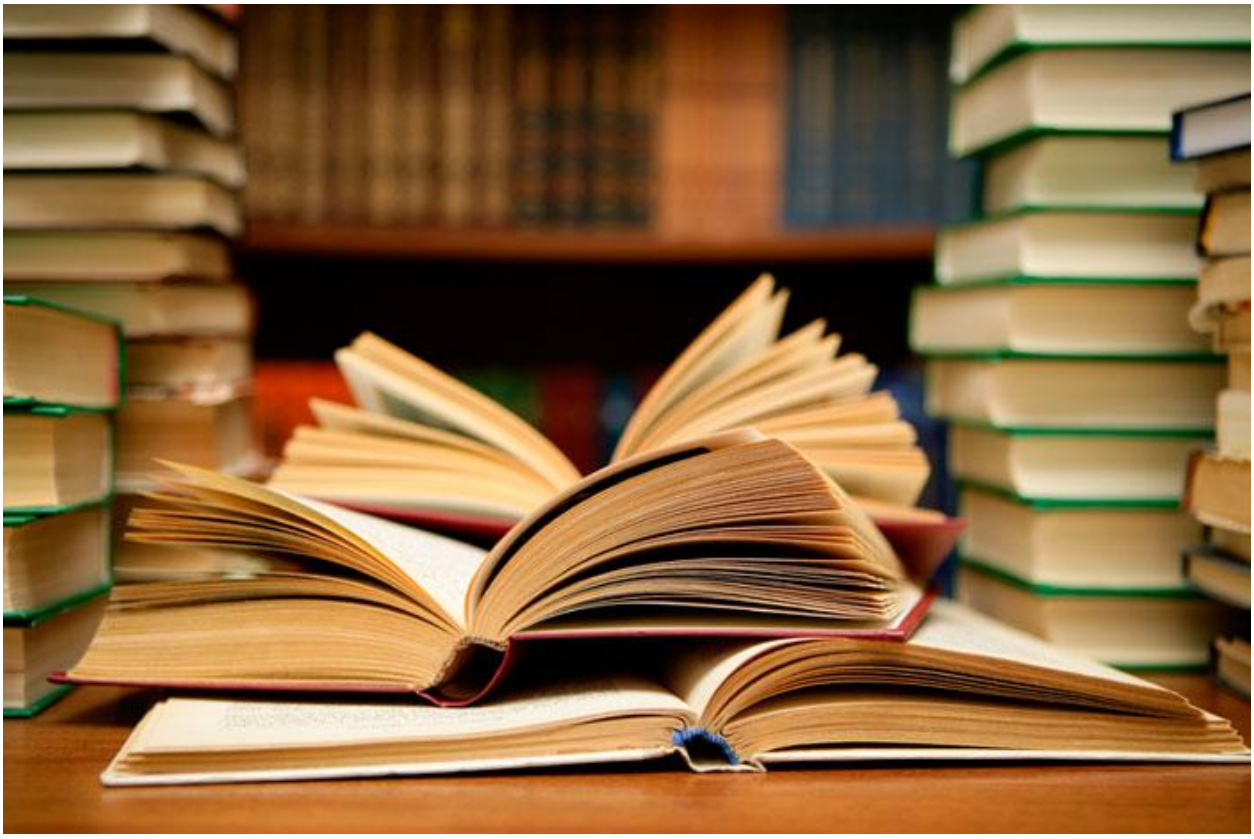

5. Bibliography

[1] V. Terzieva, J. Fransaer, J.P. Celis, J. Electrochem. Soc. 147 (2000)198.

[2] L. Shi, C. Sun, P. Gao, F. Zhou, W. Liu, Appl. Surf. Sci. 252 (2006) 3591.

[3] B. Szczygiel, M. Kolodziej, Electrochim. Acta 50 (2005) 4188.

[4] C.S. Lin, C.Y. Lee, C.F. Chang, C.H. Chang, Surf. Coat. Technol. 200 (2006) 3690.

[5] N. Damean, B.A. Parviz, J.Ng. Lee, T. Odom, G.M. Whitesides, J. Micromech. Microeng. 15 (2005)29.

[6] L.K. Lagorce, O. Brand, M.G. Allen, J. Microelectromech. Syst. 8 (1) (1999) 2.

[7] T. Osaka, T. Sawaguchi, F. Mizutani, T. Yokoshima, M. Takai, Y. Okinaka, J. Electrochem. Soc. 146 (1999) 3295.

[8] I. Tabakovic, V. Inturi, S. Riemer, J. Electrochem. Soc. 149 (2002) C18.

[9] F. Lallemand, D. Comte, L. Ricq, P. Renaux, J. Pagetti, C. Dieppedale, P. Gaud, Appl. Surf. Sci. 225 (2004) 59.

[10] M. Onoda, K. Shimizu, T. Tsuchiya, T. Wanabe, J. Magn. Magn. Mater. 126 (1993) 595.

[11] T. Osaka, Electrochim. Acta 42 (1997) 3015. H.J. Cho, C.H. Ahn, J. Microelectromech. Syst. 11 (1) (2002) 78.

[12] T.S. Chin, J. Magn. Mater. 209 (2000) 75.

[13] C.T.J. Low, R.G.A. Wils, F.C. Walsh, Surf. Coat. Technol. 201 (2006) 371.

[14] S. Guan, B.J. Nelson, K. Vollmers, J. Electrochem. Soc. 151 (2004) C545.

[15] S. Pane, E. Gomez, E. Valles, Electrochem. Commun. 9 (2007) 1755–1760

[16] E. Gomez, S. Pane, E. Valles, Electrochem. Commun. 7 (2005) 1225–1231.

[17] M. Duch, J. Esteve, E. Gomez, R. Perez-Castillejos, E. Valles, J. Electrochem. Soc. 149 (4) (2002) C201.

[18] M. Duch, J. Esteve, E. Gomez, R. Perez-Castillejos, E. Valles, J. Micromech. Microeng. 12 (2002) 400–405.

[19] W.A. Kaczmarek, E.Z. Radlinska, B.W. Ninham, Mat. Chem. Phys. 35 (1993) 31–35.

[20] W.A. Kaczmarek, B.W. Ninham, Mat. Chem. Phys. 40 (1995) 21–29.

[21] N.K. Shrestha, G. Kobayashi, T. Saji, Chem. Lett. 33 (2004) 984.

[22] N.K. Shrestha, M. Kawai, T. Saji, Surf. Coat. Technol. 200 (2005) 2414.

[23] S. Pane, E. Gomez, J. Garcia-Amoros, D. Velasco, E. Valles, Appl. Surf. Sci. 253 (2006) 2964.

[24] S. Pane, E. Gomez, J. Garcia-Amoros, D. Velasco, E. Valles, J. Electroanal. 615 (2008) 2, 117-123.

[25] A. Bastos, S. Zaefferer, D. Raabe, C. Schuh, Acta Materialia 54 (2006) 2451–2462.

[26] P.A. Gay, P. Bercot, J. Pagetti, Surf. Coat. Technol. 140 (2001) 147.

[27] A. Grosjean, M. Rezrazi, J. Takadoum, P. Bercot, Surf. Coat. Technol. 137 (2001) 92.

[28] A.F. Zimmerman, G. Palumbo, K.T. Aust, U. Erb, Mater. Sci. Eng. A328 (2002) 137.

[29] W.X. Chen, J.P. Tu, L.Y. Wang, H.Y. Gan, Z.D. Xu, X.B. Zhang, Carbon 41 (2003) 215.

[30] K.H. Hou, M.D. Ger, L.M. Wang, S.T. Ke, Wear 253 (2002) 994.

[31] Watson, S.A., "Electroforming Today", Asia Pacific Interfinish 90, Singapore 1990, page 5-1.

[32] Fehse, H.F., "Possible Artistic Applications of Electroforming", Eighth Ulmer Gesprach - Galvanoformung, Eugen G. Leuze Verlag, Saulgau 1986, page 8.

[33] Ahrens, H., "Problems and Solutions to Electroforming Replication", Eighth Ulmer Gesprach - Galvanoformung, Eugen G. Leuze Verlag, Saulgau 1986, page 19.

[34] Di Bari, G.A., "Electroforming", Electroplating Engineering Handbook - Fourth Edition, edited by L.J. Durney, Van Nostrand Reinhold Company Inc., New York 1984, page 474.

[35] Suchentrunk, R. and Tuscher, O., "Electroforming in Aerospace Engineering", Galvanotechnik, 70(12), 1178 -1184 (1979).

[36] Squitero, A.D., "Take Advantage of Modern Electroforming", Mach. Tool Blue Book, 69(5), 78-86 (1974)

[37] Hartley, P., "Electroforming", Eng. Mat. Design, 17(7), 13-14 (1973).

[38] Spencer, L.F., "Modern Electroforming - Part 2. Electroforming Solutions", Met. Finish., 71(4), 53-59 (1973); 71(3), 54-57 (1973).

[39] Sanborn, C.B.,"Nickel Electroforming Applications - Why They Exist", AD-738272, NTIS, Springfield, VA, 1972, pages 65-81.

[40] Weiler, G.G., "Electroforming - Definition and Literature Survey", Metalloberflaesche", 26(10), 381 (1972).

[41] Spiro, P., Electroforming, Robert Draper Ltd., Teddington, England, 1971, 335 pages.

[42] Di Bari, G.A., " Interlaboratory Evaluation of a Simple Ductility Tester and a Review of the Ductility of Nickel Sulfamate Deposits", AESF Proceedings of the Annual Conference in Toronto, June 1991

[43] Huang, C.H., Wu, H.M. and Hon,Y.H., "High-Strength Electroformed Nickel", Plat. Surf. Finish., Apr., 56 (1990).

[44] Clark, B., "Effects of Ammonia on the Ductility of Nickel Deposited from Sulfamate Solutions", American Electroplaters and Surface Finishers Society, Orlando, FLA, 1989.

[45] Glenn A. Malone, Electroplating nickel-CobaltAlloys by Pulse Plating with Automatic Anode Current Switching, Bell Aerospace Textron, 1979

[46] Muller, H. and Kreye, H., "Dependency of the Internal Stress on Microstructure", Eighth Ulmer Gesprach - Galvanoformung, Eugen G. Leuze Verlag, Saulgau 1986, 117.

[47] Safranek, W.H., The Properties of Electrodeposited Metals and Alloys - A Handbook, Second Edition, American Electroplaters and Surface Finishers Society, Orlando, Florida, 1986.

[48] Wearmouth, W.R. and Belt, K.C, "Electroforming with Heat-Resistant Sulfur-Hardened Nickel", Plating and Surface Finishing, 66(10),53-57 (1979).

[49] Dini, J.W., Johnson, H.R. and Brooks, J.A., "Zinc in Sulfamate Nickel Deposits – Influence on Weldability of Electroforms", Metal Finishing, 77(2), 99-101 (1979).

[50] Dean, A.V. and Wearmouth, W.R., "New Backing Techniques for Electroformed Molds and Dies", Electroplat. Met. Finish., 28(12), 18-23 (1975).

[51] Cooper, G., "Forming Processes for Metal Matrix Composites", Composites, 1(3), 153-159 (1970).

[52] Malone, G. A., "Electrodeposition of Dispersion Strengthened Alloys", Symposium on Electrodeposited Metals for Selected Applications, Battelle Memorial Laboratories, Columbus, Ohio, November 1973.

[53] C. Guo, Y. Zuo, X. Zhao, J. Zhao, J. Xiong, Surf. Coat. Technol. 202 (2008) 3385.

[54] A. Brenner, Electrodeposition of Alloys. Principles and Practice, Academic Press, New York, 1963.

[55] P. Cojocaru, S. Pahari, L. Magagnin, D. Dietrich, A. Liebig, T. Lampke; Z. Phys. Chem. 225 (2011) 351–361

[56] Gnass, E., "Electroforming with Dispered Particles", Eighth Ulmer Gesprach - Galvanoformung, Eugen G. Leuze Verlag, Saulgau 1986, page 75 (in German).

[57] Sykes, J. M. and Allner, D.J., "Mechanisms for the Formation of Electrodeposited Composite Coatings", Trans. Inst. of Metal Finishing, 52, 28 (1974).

[58] Harris, S.J. and Boden, P.J., "Electroforming with Composite Materials", Electroplat. Metal Finishing, 26(5), 9-13 (1973).

[59] Logsdon, J.R., "Electroforming Very Large Items", Plat. Surf. Finish., Mar., 22 (1990).

[60] G. Wu, N. Li, D.R. Zhou, K. Mitsuo, Surf. Coat. Technol. 176 (2003) 157.

[61] L. Shi, C.F. Sun, F. Zhou, W.M. Liu, Mater. Sci. Eng. A. 397 (2005) 190.

[62] L. Shi, C.F. Sun, W.M. Liu, Appl. Surf. Sci. 254 (2008) 6880.

[63] P. Cojocaru, M. Spreafico, E. Gomez, E. Vallés, L. Magagnin; Surface & Coatings Technology 205 (2010) 195–199

[64] Bazzard, R. and Boden, P.J., "Codeposition of Chromium Particles in a Nickel Matrix", Trans. Inst. of Metal Finishing, 50(2),63-69 (1972).

[65] Fedosyuk VM. NATO Science Series, 3: high technology. Nanostructured Films and Coatings 2000;78:85–102.

[66] Wang N, Arnold DP. IEEE Trans Magn 2008;5:3969–72.

[67] Kulkarni S, Roy S. J Magn Magn Mater 2010;322:1592–6.

[68] Wu K-H, Traisigkhachol O, Gatzen HH. ECS Trans 2007;3:191–202.

[69] P. Cojocaru, L. Magagnin, E. Gomez, E. Vallés; Materials Letters 65 (2011) 2765–2768

[70] B. Lochel, A. Maciossek, J. Electrochem. Soc. 143 (1996) 3343–3348.

[71] T. Wang, A.B. McCandless, R.M. Lienau, K.W. Kelly, D. Hensley, Y. Desta, Z.G. Ling, J. Microelectromech. Syst. 14 (2005) 400–409.

[72] S. Guan, B.J. Nelson, J. Microelectromech. Syst. 15 (2006) 330–337.

[73] R.D. Noce, N. Barelli, R.F.C. Marques, P.T.A. Sumodjo, A.V. Benedetti, Surf. Coat. Technol. 202 (2007) 107–113.

[74] de Julian-Fernandez C, Sangregorio C, Innocenti C, Mattei G, Mazzoldi P. Inorg Chim Acta 2008;361:4138–42.

[75] Spalding NA. Ferroelectrics and ferromagnets. Physics of Ferroelectrics. Heidelberg: Springer-Verlag GmbH; 2007.

[76] Cortés M, Gómez E, Vallés E. Electrochem Commun 2010;12:132–6.

[77] Jacintho GVM, Kosaka PM, Petri DFS, Suarez PAZ, Rubim JC. J Nanosci Nanotechnol 2009;9:3617–21.

[78] Y. Sverdlov, Y. Rosenberg, Y.I. Rozenberg, R. Zmood, R. Erlich, S. Natan, Y. Shacham-Diamand, Microelectron. Eng. 76 (2004) 258–265.

[79] S. Guan, B.J. Nelson, J. Electrochem. Soc. 152 (2005) C190–C195.

[80] J. Casals-Terré, M. Duch, J.A. Plaza, J. Esteve, R. Pérez-Castillejos, E. Vallés, E. Gómez, Sens. Actuators A 147 (2008) 600–606.

[81] J.N Hilfiker, D.W. Glenn, S. Heckens, J.A. Woollam, K.W.Wierman, J. Appl. Phys. 79 (1996) 6193.

[82] Z.Q. Zou, H. Wang, J. Zhou, D.F. Shen, Y.P. Lee, Eur. Phys. J. B 45 (2005) 97–102.

[83] Cojocaru P, Muscolino F, Magagnin L, Vázquez M, Badini-Confalonier G, Carac G. ECS Trans Electrochem Soc 2010;25:147–53.

[84] V.D. Jovic, N. Tosic, M. Stojanovic, J. Electroanal. Chem. 420 (1997) 43–51.

[85] E. Gómez, J. Ramírez, E. Vallés, J. Appl. Electrochem. 28 (1998) 71–79.

[86] C. Fan, D.L. Piron, Electrochim. Acta 41 (1996) 1713–1719.

[87] A. Bastos, S. Zaefferer, D. Raabe, and C. Schuh, Acta Mater. 54 (2006) 2451.

[88] Cojocaru P, Spreafico M, Gomez E, Vallés E, Magagnin L. Surf Coat Technol 2010;205:195–9.

[89] Cojocaru P, Muscolino F, Magagnin L, Vázquez M, Badini-Confalonier G, Carac G. ECS Trans Electrochem Soc 2010;25:147–53.

[90] Shamaila S, Sharif R, Riaz S, Ma M, Khaleeq-ur-Rahman M, Han XF. J Magn Magn Mater 2008;320:1803–9.

[91] P. Cojocaru, L. Magagnin, E. Gómez, E. Vallés; Journal of Alloys and Compounds 503 (2010) 454–459.